Interplay of Proton Transfer, Electron Transfer and Proton-Coupled Electron Transfer in Transition Metal Mediated Nitrogen Fixation

Thesis by

Benjamin David Matson

In Partial Fulfillment of the Requirements for

the degree of

Doctor of Philosophy

CALIFORNIA INSTITUTE OF TECHNOLOGY

Pasadena, California

2018

(Defended February 9th, 2018)

ACKNOWLEDGEMENTS

My time here at Caltech has been one of the most challenging yet rewarding periods of my life and there are so many people who have supported me on this journey. First off, I need to thank my advisor, Jonas, for taking me into his lab and allowing me to grow as a scientist. Jonas gave me the freedom to research new areas for our group and allowed me to really identify the types of chemistry I was truly passionate about. While the road has not always been smooth, Jonas was there to redirect me and get me to where I am today.

Next I'd like to thank my coworkers in the Peters lab. Several students in front of me, John Anderson, Jon Rittle, Sid Creutz, and Dan Suess, paved the way for the N_2 chemistry that has defined my thesis. During my time here, I have had the distinct pleasure of collaborating with many great chemists and friends. Most notably, Matthew Chalkley, Trevor Del Castillo and I have had the pleasure of working on several fruitful projects. They are truly exceptional chemists whose experimental expertise has guided me greatly along my Ph.D. In addition to N_2 chemistry, I have had the opportunity to work on denitrification chemistry with Tanvi Ratani. Tanvi provided numerous experimental breakthroughs really took a difficult project to the next level and I am happy to have played a (small) part in that. In addition to scientific breakthroughs, Matt, Tanvi, Gaël Ung and Miles Johnson have played an invaluable role in 'team morale'. Their confidence and support has helped me through many bad days in the lab and has kept to grounded and focused.

Outside the lab, I have had the chance to do amazing things with truly great people. Paul Walton, Jenna Bush, Noah Duffy, Josh Buss, Mark Nesbit and Kareem Hannoun have

joined me on many hiking and backpacking trips to see some of the most beautiful places in the country and have been amazing friends all along the way. Paul, Mark, Trevor and Beau Prichett also provided a great outlet in the form of our band, The 818s. Regularly described as “a participant” in some local festivals, my time with the band has been incredibly rewarding and tons of fun. To make up for the nerdy-ness of playing in a band, I have also had the chance to make great friends while playing Dungeons and Dragons at Caltech. Matt Davis, Richard Mossesso, Elizabeth Bernhardt, Nick Cowper, Noah and Trevor have made this quintessentially geeky game one of the most fun experiences of my time at Caltech.

Finally, I would like to thank my family for their incredible support over the last 5 years. My parents and my sister, Jennifer, have always been there for me during this time. Their humor and love has kept me going through many of the difficult periods I’ve worked through over the years. I also want to thank my grandma who, unfortunately, did not get to see me make it all the way through my Ph.D. She was always so proud of me and provided constant support over the years. To all my family and friends, I thank them for sticking by my through the years. Even when I was preoccupied, too busy to keep in touch or just grumpy, they have always been by my side. I am truly lucky to be surrounded by so many wonderful people.

ABSTRACT

Mitigation of the hydrogen evolution reaction (HER) is a key challenge in selective small molecule reduction catalysis, including the nitrogen (N_2) reduction reactions (N_2RR) using H^+/e^- currency. Here we explore, via DFT calculations, three iron model systems, P_3^EFe (E = B, Si, C), known to mediate both N_2RR and HER, but with different selectivity depending on the identity of the auxiliary ligand. It is shown that the respective efficiencies of these systems for N_2RR trend with the predicted N–H bonds strengths of two putative hydrazido intermediates of the proposed catalytic cycle, $P_3^EFe(NNH_2)^+$ and $P_3^EFe(NNH_2)$. Bimolecular proton-coupled electron transfer (PCET) from intermediates with weak N–H bonds is posited as a major source of H_2 instead of more traditional scenarios that proceed via metal hydride intermediates and proton transfer/electron transfer (PT/ET) pathways.

Studies on our most efficient molecular iron catalyst, $[P_3^BFe]^+$, reveal that the interaction of acid and reductant, Cp^*_2Co, is critical to achieve high efficiency for NH_3, leading to the demonstration of electrocatalytic N_2RR. Stoichiometric reactivity shows that Cp^*_2Co is required to observe productive N–H bond formation with anilinium triflate acids under catalytic conditions. A study of substituted anilinium triflate acids demonstrates a strong correlation between pK_a and the efficiency for NH_3, which DFT studies attribute to the kinetics and thermodynamics of Cp^*_2Co protonation. These results contribute to the growing body of evidence suggesting that metallocenes should be considered as more than single electron transfer reagents in the proton-coupled reduction of small molecule substrates and that ring-functionalized metallocenes, believed to be intermediates on the background HER pathway, can play a critical role in productive bond-forming steps.

PUBLISHED CONTENT AND CONTRIBUTIONS

1. Matson, B. D.; Peters, J. C. Fe-mediated HER vs N_2RR: Factors that Determine Selectivity in $P_3^EFe(N_2)$ (E = B, Si, C) Catalyst Model Systems. *ACS Catalysis*, **2018**, *8*, 1448-1455. https://pubs.acs.org/doi/abs/10.1021/acscatal.7b03068

I performed all calculations and wrote the manuscript for this work.

2. Chalkley, M. J.; Del Castillo, T. J.; Matson, B. D.; Roddy, J. P.; Peters, J. C. Catalytic N_2-to-NH_3 Conversion by Fe at Lower Driving Force: A Proposed Role for Metallocene-Mediated PCET. *ACS Central Science*, **2017**, 3, 217-223. http://pubs.acs.org/doi/full/10.1021/acscentsci.7b00014

I performed all calculations, assisted in the analysis of catalytic and spectroscopic data, and wrote portions of this manuscript

TABLE OF CONTENTS

DETAILED TABLE OF CONTENTS

LIST OF FIGURES

LIST OF TABLES

LIST OF ABBREVIATIONS

atm Atmosphere

Avg Average

BAr^F_4 $B(3,5\text{-}C_6H_3(CF_3)_2)_4$

BDE Bond Dissociation Enthalpy

BDFE Bond Dissociation Free-Energy

C Constant

ca circa

calc Calculated

CN Cyanide

CNH_x Generic CN-derived ligand with x H atoms

Cp Cyclopentadienyl

Cp* Pentamethylcyclopentadienyl

CV cyclic voltammogram

DFT Density Functional Theory

DME 1,2-dimethoxyethane

e^- Electron

EPR Electron paramagnetic resonance

eq Equation

equiv Equivalents

E^o Reduction potential

$Fc^{+/0}$ Ferrocene/Ferrocenium couple

FeMoco Iron-Molybdenum cofactor

GC gas chromatography

G Gauss

g Gram

g_n Electron g-factor

GC Gas chromatography

GHz Gigahertz

H Enthalpy

HIPT hexa-isopropyl-terphenyl

HOMO Highest-Occupied Molecular Orbital

Hz Hertz

iPr isopropyl

IR Infrared

K Kelvin

K_{eq} Equilibrium constant

L Generic neutral dative ligand

LUMO Lowest-Unoccupied Molecular Orbital

kcal Kilocalorie

M Concentration in molarity

max Maximum

Me Methyl

mg Milligram

MHz Megahertz

mL Milliliter

mM Millimolar

mm Millimeter

mV Millivolt

mmol Millimole

MO Molecular orbital

mol Mole

n generic number

nm nanometer

NMR Nuclear magnetic resonance

N_xH_y Generic nitrogenous ligand with x N atoms and y H atoms

NNH_x Generic nitrogenous ligand with 2 N atoms and x H atoms

o ortho

OTf Triflate (OSO_2CF_3)

Ph Phenyl

pK_a Acid dissociation constant

R Generic organic group

RT Room temperature

S Entropy

P_3^B (o-^{i}Pr$_2$P(C$_6$H$_4$))$_3$B-

P_3^C (o-^{i}Pr$_2$P(C$_6$H$_4$))$_3$C-

P_3^{Si} $(o\text{-}^{i}Pr_2P(C_6H_4))_3Si$-

TBA Tetra-n-butyl ammonium

tBu tert-Butyl

TEMPO 2,2,6,6-tetramethylpiperidine-N-oxide

THF Tetrahydrofuran

TMS Trimethylsilyl

UV Ultraviolot

V Volt

XRD X-ray diffraction

N_α Proximal nitrogen atom of a bound N_2 ligand

N_β Terminal nitrogen atom of a bound N_2 ligand

γ High frequency electromagnetic radiation

Q Mössbauer quadrupole splitting

δ chemical shift or Mössbauer isomer shift

° Degree

°C Degrees Celsius

ε Extinction coefficient in units of $M^{-1}cm^{-1}$

η_x Hapticity of order x

λ Wavelength

λ_{max} Wavelength of local maximum intensity

μ Bridging

μA Microamps

ν_{xy} Vibrational frequency between atoms x and y

Σ Summation

σ Sigma symmetry orbital or interaction

σ^* Sigma symmetry antibonding interaction

π Pi symmetry orbital or interaction

π^* Pi symmetry antibonding interaction

$\tau_{1/2}$ Half-life

Å Angstrom

12-C-4 12-crown-4

^{1}H Hydrogen-1

^{2}H Hydrogen-2

^{11}B Boron-11

^{13}C Carbon-13

^{15}N Nitrogen-15

^{31}P Phosphorus-31

2-MeTHF 2-Methyl-tetrahydrofuran

def2-xxx Basis sets for DFT

TPSS, etc. DFT functional

Chapter 1. Introduction

1.1. Opening Remarks

The global nitrogen cycle is a crucial biogeochemical cycle and underpins much of life on Earth.[1] In particular, the conversion of dinitrogen (N_2) to ammonia (NH_3) provides a means by which atmospheric N_2, a relatively inert gas that makes up 78% of Earth's atmosphere, can be converted to a bioavailable form (NH_3, NO_2^- and NO_3^-).[1] The fixation of N_2 can occur via non-biological natural processes, as in the splitting of N_2 by lightning, or via biological and industrial processes.[1-3] The latter two processes have garnered significant interest in chemistry and biology.[4]

The industrial process by which N_2 is fixed, referred to as the Haber-Bosch process, is performed on a massive scale and the drastic increase in the human population in the 20th century is often credited to its use in fertilizer production.[1] While the Haber-Bosch process continues to be a major source of bioavailable nitrogen globally, accounting for up to 80% of nitrogen in the human body, the high temperatures and pressures required has led to interest in developing a more energy efficient process.[1]

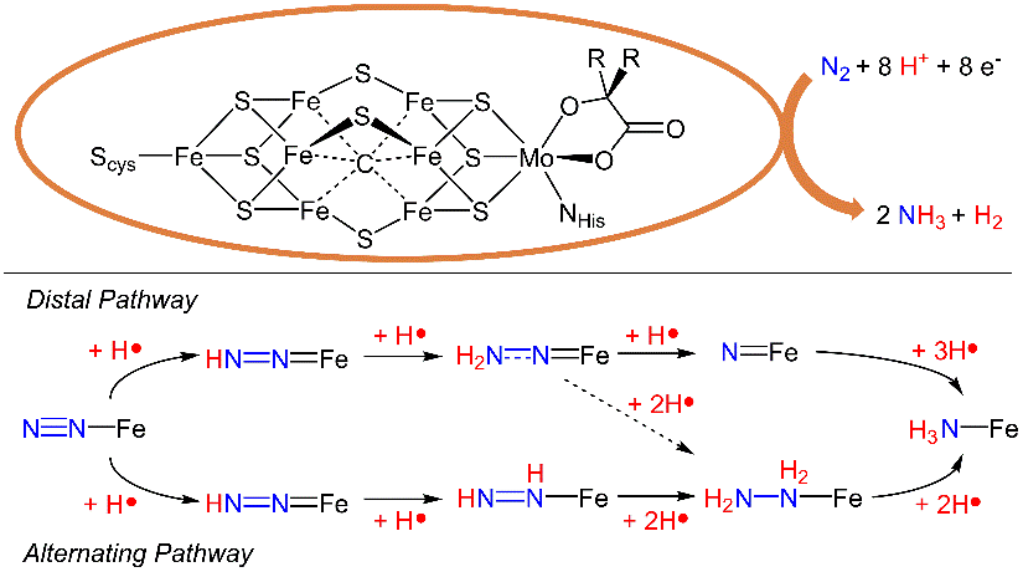

Figure 1.1. (Top) Biological nitrogen fixation is catalyzed by the iron-molybdenum cofactor (FeMoco) in nitrogenase enzymes. (Bottom) Possible mechanisms by which a single Fe site can catalyze the reaction.

Biological nitrogen fixation has provided ideal inspiration in the development synthetic N_2 fixation processes.[4] Studies on the nitrogenase enzyme have revealed three major subtypes: iron-molybdenum nitrogenase, vanadium-iron nitrogenase, and all iron nitrogenase.[5] The most well studied of these, the molybdenum-iron nitrogenase, contains the iron-molybdenum cofactor (FeMoco; Figure 1.1). In recent years, structure-function studies on FeMoco have led to increased interest in the mechanism by which N_2 can be reduced at a single Fe center.[7] At a single metal site, two limiting mechanisms have been proposed, referred to as the distal pathway and the alternating pathway (Figure 1.1, bottom). The distal mechanism is characterized by the early release of the first equivalent of NH_3, with concomitant formation of a terminal nitride intermediate, Fe(N). In contrast,

the alternating mechanism is associated with the late release of the first equivalent of NH_3 and is characterized by the formation of diazene, Fe(NHNH) and hydrazine, Fe(NH_2NH_2) intermediates.[7] In addition to these limiting mechanisms, hybrid mechanisms are similarly plausible. A notable example of a hybrid mechanism is the so-called 'distal-to-alternating' mechanism, in which Fe(NH_2NH_2) and/or Fe($NHNH_2$) are formed without initial formation of an Fe(NHNH) species.

In the study of synthetic systems for NH_3 formation, designated in this work as the nitrogen reduction reaction (N_2RR), the hydrogen evolution reaction (HER) competes for acid and reductant equivalents. Suppression of this unproductive pathway is crucial to increasing the efficiency of a system for N_2RR, generally reported as the $\%NH_3$ per e^- equivalent. As such, elucidation of the mechanistic interplay between N_2RR and HER is perhaps the most important factor in the increasing the efficacy of N_2RR catalyst systems.

Central to mechanistic studies into multi-proton, multi-electron catalyst systems, including N_2RR, is the interchange between proton transfer (PT), electron transfer (ET), proton-coupled electron transfer (PCET) and hydride transfer (HT). Accordingly, mechanistic steps for N_2RR can be characterized by PT and ET as separate kinetic steps or by the concerted transfer of a proton and one or two electrons (PCET or HT, respectively). Given that N_2RR necessarily involves the net addition of 6 H-atom ($H^\bullet$) equivalents, the synchronous and/or asynchronous delivery of H^+ and e^- to the N_2 substrate produces drastic changes in the intermediates produced in the process and, thus, the selectivity of the system.

1.2. N_2RR Using Soluble Transition Metal Catalysts

In this thesis, research efforts aim at elucidating the role of PT, ET and PCET in N_2RR are presented. Particular attention is paid to the impact these mechanistic steps have on the overall selectivity of the systems. Over the last decade, our group, and others, have uncovered several methods for transition metal mediated N_2RR via alteration of the catalyst, as well as the stoichiometric reagents (acid and reductant).[10] The research presented in this thesis is based on the most diverse class of catalysts, namely the P_3^EFe (E = B, C or Si) based systems (Figure 1.2).

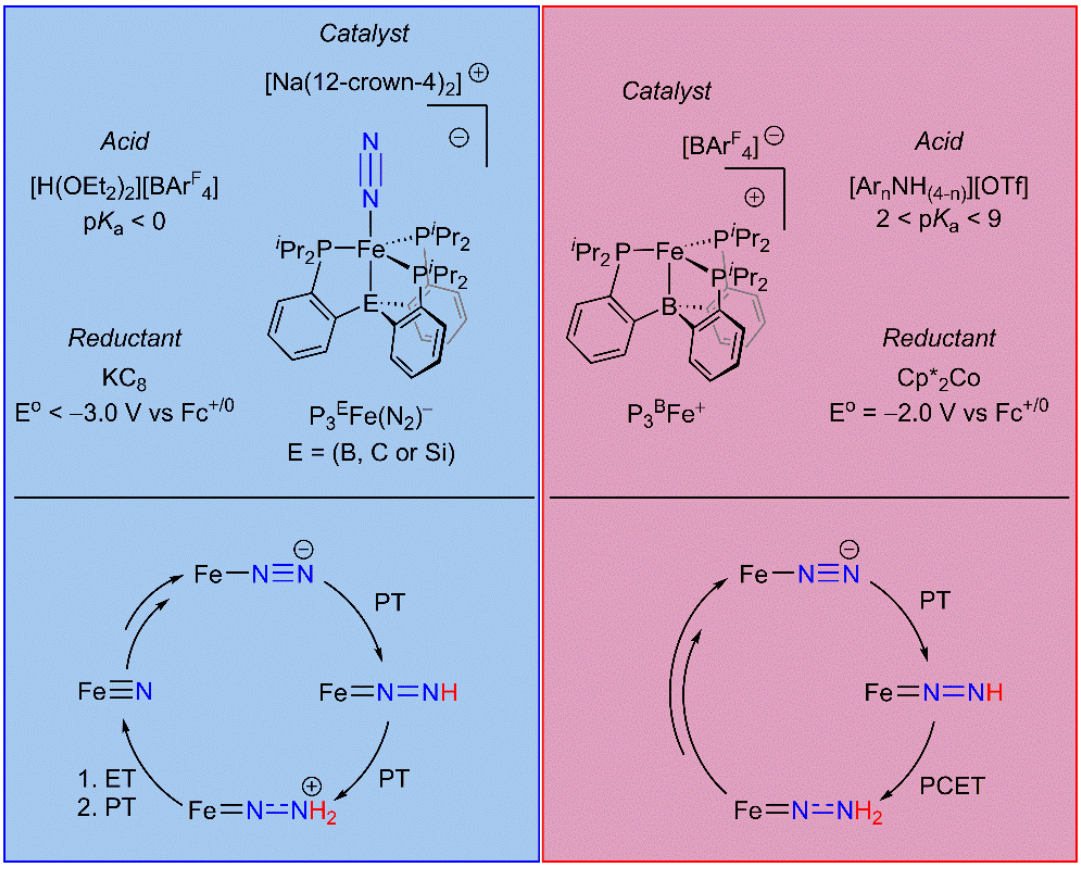

Figure 1.2. (Top) Overview of P_3^EFe catalysts, acids and reductants discussed in this thesis. (Bottom) Proposed mechanisms for each set of reagents (*vida infra*).

In initial work on N_2RR by $P_3^EFe(N_2)^-$ based catalysis, all three catalysts studied (E = B, C or Si) were shown to be formally catalytic upon the addition of strong reductant, KC_8 ($E^o < -3.0$ V vs $Fc^{+/0}$; Figure 1.2), and acid, $[H(OEt_2)_2][BAr^F_4]$ ($HBAr^F_4$, BAr^F_4 = tetrakis-(3,5-bis(trifluoromethyl)phenyl)borate; pK_a < 0.0; Figure 1.2).[4d] The P_3^BFe system was found to be the most efficient catalyst, with efficiencies for NH_3 up to 45 ± 3%. While still catalytic, the $P^{3C}Fe$ and $P_3^{Si}Fe$ systems were found to be less efficient for N_2RR, with efficiencies up to 36 ± 6% and 5 ± 3%, respectively. More recent studies have revealed that a related catalyst, $[P_3^BFe][BAr^F_4]$, can achieve much higher efficiencies for N_2RR (up to 77%) using a decamethylcobaltocene reductant (Cp^*_2Co; $E^o = -2.0$ V vs $Fc^{+/0}$) and a 2,5-dichloroanilinium triflate acid ($[^{2,5\text{-Cl}}PhNH3][OTf]$; p$K_a$ = 4.1).[4e]

Of particular interest to the studies presented herein is the role that the acid and reductant choice play in the plausibility of PT, ET and PCET based mechanisms. Notably, the $KC_8/HBAr^F_4$ cocktail should be associated with increased favorability of asynchronous PT and ET steps, given the strength of these reagents and the lack of stable intermediates formed upon reaction between them. In contrast, we've shown that the use of $Cp^*_2Co/[^RPhNH_3][OTf]$ is associated with an increased role of PCET mechanisms due to the formation of a highly active PCET reagent, a protonated Cp^*_2Co species ($[Cp^*Co(\eta^4\text{-}C_5Me_5H)]^+$), under catalyst conditions.

1.3. Selectivity for N_2RR vs HER

In chapter 2, the interplay of N_2RR and HER in catalysis using KC_8 and $HBAr^F_4$ is explored in depth.[11] The use of KC_8 and $HBAr^F_4$ provides the most complete comparison between P_3^EFe catalysts discussed, as all three systems (E = B, C or Si) are formally catalytic, but with drastically different efficiencies for N_2RR and HER. Beyond the differing N_2RR efficiencies discussed previously, the efficiencies for HER in P_3^BFe (44%) and $P_3^{Si}Fe$ (88%) have been shown to trend in the opposite direction, consistent with HER being a major source of N_2RR efficiency loss.

Investigating this difference in N_2RR and HER efficiencies via density functional theory (DFT) point to the $P_3^EFe(NNH_2)^{+/0}$ intermediates, and their stability, as key players. Despite the relative lack of PCET reactivity from the $KC_8/HBAr^F_4$ interaction directly, we invoke bimolecular PCET between reactive $P_3^EFe(N_xH_y)$ species as the major source of HER on the these scaffolds (Figure 1.3). In particular, while the $Fe(NNH_2)$ is predicted to be the only species capable of bimolecular HER on the P_3^B scaffold, the cationic species, $Fe(NNH_2)^+$, on $P_3^{C/Si}$ are predicted to be long-lived and highly reactive for bimolecular H_2 release (Figure 1.3).

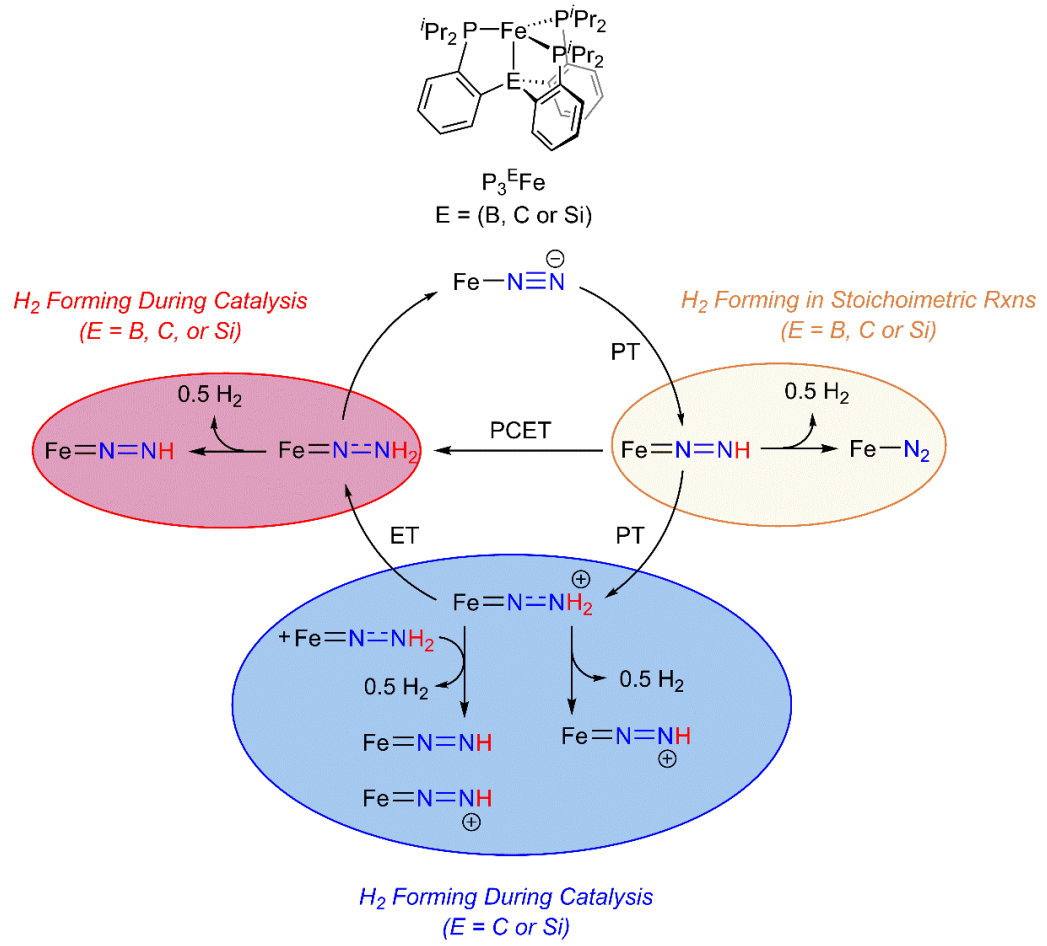

Figure 1.3. Overview of predicted HER mechanisms on P_3^EFe systems, as discussed in chapter 2.

In addition to the $Fe(NNH_2)^{+/0}$ species, predicted to be major sources of HER under catalytic conditions (using KC_8/$HBAr^F_4$), the diazenido species, Fe(NNH), are predicted to be extremely reactive intermediates and are invoked as sources of H_2 in the stoichiometric oxidation of $P_3^EFe(N_2)$ species.[4a,f,g] In addition, the bimolecular coupling of Fe(NNH) species is predicted to become relevant in catalytic systems in which protonation reactions are slowed, i.e. with the use of anilinium triflate acids. The solubility of the anilinium acids

in Et_2O is quite low and, accordingly, is associated with slower PT under turnover conditions. As a result, PCET reactivity from the Cp^*_2Co/[^{R}PhNH$_3$][OTf] combination is therefore invoked as the source of increased N_2RR efficiencies using these reagents.

1.4. Proton-Coupled Electron Transfer in N_2RR

Chapters 3 and 4 are focused on our discovery that a protonated decamethylcobaltocene species, [Cp*Co(η^4-C_5Me_5H)]$^+$, likely serves as PCET reagent under conditions in which Cp^*_2Co serves the reductant and [^{R}PhNH$_3$][OTf] serves as the acid source.[4e] More specifically, chapter 3 outlines our initial discovery that N_2RR using P_3^BFe can be accomplished with increased efficiency using reagents which substantially lower the overpotential of the system (ca. 100 kcal/mol lower). To rationalize this counterintuitive observation, we invoke the formation of a protonated metallocene species, [Cp*Co(η^4-C_5Me_5H)]$^+$, and suggest that it serves as a PCET reagent under turnover conditions (Figure 1.4).

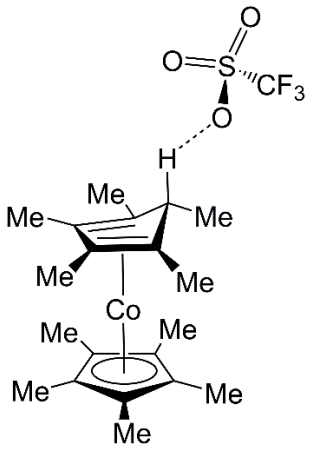

[Cp*Co(η⁴-C₅Me₅H)][OTf]

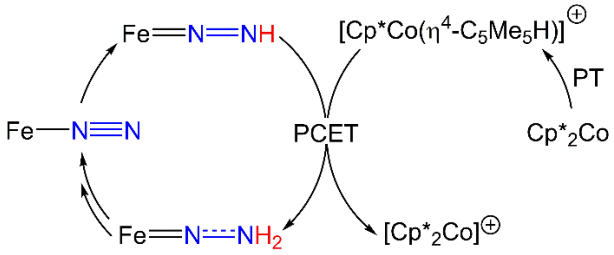

Figure 1.4. (top) Proposed structure of the $[Cp^*Co(\eta^4\text{-}C_5Me_5H)]^+$ intermediate discussed in chapters 3 and 4. (bottom) Proposed mechanism in which $[Cp^*Co(\eta^4\text{-}C_5Me_5H)]^+$ acts as a PCET reagent.

In chapter 4, we expand upon this discovery via a thorough study on the effect of pK_a on the efficiency for N_2RR vs HER. By alteration of the electronics of the aryl ring in $[^{R}PhNH_3][OTf]$ acids, catalytic turnover is achieved over 8 pK_a units using Cp^*_2Co as the reductant. Further, the efficiency for N_2RR is shown to increase with acid strength and HER is shown to concomitantly decrease. Using DFT, we suggest that the rate of Cp^*_2Co protonation as the likely source of this pK_a effect. As the final piece of evidence for the potential role of $[Cp^*Co(\eta^4\text{-}C_5Me_5H)]^+$ in N_2RR, catalytic yields of NH_3 are achieved

electrochemically using a P_3^BFe catalyst, diphenylammonium acid $[Ph_2NH_2]^+$ and a Cp^*_2Co co-catalyst. Under electrolytic conditions we suggest that Cp^*_2Co may be acting as a PCET mediator, as well as an ET shuttle.

1.5. Method for Predicting E-H Bonds Strengths Using DFT

The final chapter of this thesis discusses efforts to increase the accuracy of DFT predicted bond dissociation free-energies ($BDFE_{E-H}$) of transition metal bound E–H bonds. The importance of $BDFE_{E-H}$ predictions are apparent in all chapters in this work and in chapter 5, the accuracy of these calculations are discussed as a function of DFT functional and solvent of interest. Most notably it is reported that all functionals tested show similar accuracy for gas-phase $BDFE_{E-H}$ predictions, assuming proper calibration with known literature values. It is further shown that reproduction of solvated $BDFE_{E-H}$ is significantly less accurate than gas-phase values, but that values in several common organic solvents, DMSO, MeCN and C_6H_6 can be reproduced with acceptable accuracy.

1.6. Conclusions

In sum, the following chapters will outline research efforts aimed at elucidating the mechanism by which P_3^EFe (E = B, C or Si) catalyzes HER and N_2RR. Particular attention is paid to how the choice of reductant and acid source can dictate the rates of PT, ET and PCET. Notably, bimolecular coupling of reactive P_3^EFe intermediates via PCET is presented as a likely mechanism for competing HER. Further, evidence for the formation of a reactive PCET reagent, $Cp^*Co(\eta^4\text{-}C_5Me_5H)$, is presented as a background HER

intermediate that can be intercepted by P_3^BFe species to undergo productive N–H bond formation.

The following chapters rely heavily on the use of DFT for efficient prediction of $BDFE_{E\text{-}H}$ values, pK_a values, E^o values and the kinetics associated with each of these reaction. The calculation of known values highlights the accuracy and utility of these calculations' predictive power. Thus, on a larger scale the research presented highlights the value of DFT calculations in elucidating the mechanism by which multi-proton, multi-electron reactions precede as well as key factors that can be used to inform the design of future, more efficient systems.

1.7. References

[1] Smil, V. *Enriching the Earth.* Cambridge: MIT Press, 2001.

[2] Drapcho, D. L.; Sisterson, D.; Kumar, R. *Atmospheric Environment (1967)* **1983**, 729–734.

[3] (a) Howard, J. B.; Rees, D. C. *Proc. Nat. Acad. Sci.* **2006**, *103*, 17088-17093. (b) Howard, J. B.; Rees, D. C. *Chem. Rev.* **1996**, *96*, 2965−2982. (c) Hoffman, B. M.; Lukoyanov, D.; Yang, Z.-Y.; Dean, D. R.; Seefeldt, L. C. *Chem. Rev.* **2014**, *114*, 4041−4062.

[4] For pertinent Fe systems: (a) Anderson, J. S.; Rittle, J.; Peters, J. C. *Nature* **2013**, *501*, 84−87. (b) Creutz, S. E.; Peters, J. C. *J. Am. Chem. Soc.* **2014**, *136*, 1105−1115. (c) Ung, G.; Peters, J. C. *Angew. Chem., Int. Ed.* **2015**, *54*, 532−535. (d) Del Castillo, T. J.; Thompson, N. B.; Peters, J. C. *J. Am. Chem. Soc.* **2016**, *138*, 5341–5350. (e) Chalkley, M. J.; Del Castillo, T. J.; Matson, B. D.; Roddy, J. P.; Peters, J. C. *ACS Central Science* **2017**,

3, 217-223. (f) Anderson, J. S.; Cutsail, G. E.; Rittle, J.; Connor, B. A.; Gunderson, W. A.; Zhang, L.; Hoffman, B. M.; Peters, J. C. *J. Am. Chem. Soc.* **2015**, *137*, 7803–7809. (g) Rittle, J.; Peters, J. C. *J. Am. Chem. Soc.* **2016**, *138*, 4243–4248. (h) Rittle, J.; Peters, J. C. *J. Am. Chem. Soc.* **2017**, *139*, 3161–3170. For Mo systems: (i) Kuriyama, S.; Arashiba, K.; Nakajima, K.; Matsuo, Y.; Tanaka, H.; Ishii, K.; Yoshizawa, K.; Nishibayashi, Y. *Nat. Commun.* **2016**, *7*, 12181. (j) Yandulov, D. V.; Schrock, R. R. *Science* **2003**, *301*, 76−78. (k) Arashiba, K.; Miyake, Y.; Nishibayashi, Y. *Nat. Chem.* **2011**, *3*, 120−125. (l) Kuriyama, S.; Arashiba, K.; Nakajima, K.; Tanaka, H.; Kamaru, N.; Yoshizawa, K.; Nishibayashi, Y. *J. Am. Chem. Soc.* **2014**, *136*, 9719−9731. (m) Arashiba, K.; Kinoshita, E.; Kuriyama, S.; Eizawa, A.; Nakajima, K.; Tanaka, H.; Yoshizawa, K.; Nishibayashi, Y. *J. Am. Chem. Soc.* **2015**, *137*, 5666−5669. For Co systems: (n) Del Castillo, T. J.; Thompson, N. B.; Suess, D. L. M.; Ung, G.; Peters, J. C. *Inorg. Chem.* **2015**, *54*, 9256–9262. (o) Kuriyama, S.; Arashiba, K.; Tanaka, H.; Y. Matsuo, Y.; Nakajima, K.; Yoshizawa, K.; Nishibayashi, Y. *Angew. Chem. Int. Ed.* **2016**, *55*, 14291–14295.

[5] (a) Hu, Y.; Ribbe, M. W. *Methods Mol. Biol.* **2011**, *766*, 3–7. (b) Burgess, B. K.; Lowe, D. J. *Chem. Rev.* **1996**, *96*, 2983–3011. (c) Seefeldt, L. C.; Hoffman, B. M.; Dean, D. R. *Annu. Rev. Biochem.* **2009**, *78*, 701–722. (d) Hoffman, B. M.; Dean, D. R.; Seefeldt, L. C. *Acc. Chem. Res.* **2009**, *42*, 609–619. (e) Seefeldt, L. C.; Hoffman, B. M.; Dean, D. R. *Curr. Opin. Chem. Biol.* **2012**, *16*, 19–25.

[7] (a) Chatt, J.; Dilworth, J. R.; Richards, R. L. *Chem. Rev.* **1978**, *78*, 589-625. (b) Schrock, R. R. *Acc. Chem. Res.* **2005**, *38*, 955-962. (c) Nishibayashi, Y. *Inorg. Chem.* **2015**, *54*, 9234−9247. (d) van der Ham, C. J. M.; Koper, M. T. M.; Hetterscheid, D. G. H. *Chem.*

Soc. Rev. **2014**, *43*, 5183−5191. (e) Shaver, M. P.; Fryzuk, M. D. *Adv. Synth. Catal.* **2003**, *345*, 1061−1076. (f) MacLeod, K. C.; Holland, P. L. *Nat. Chem.* **2013**, *5*, 559−565.

Chapter 2. Fe-mediated HER vs N_2RR: Exploring Factors that Contribute to Selectivity in $P_3^EFe(N_2)$ (E = B, Si, C) Catalyst Model Systems

2.1. Introduction

The reduction of nitrogen (N_2) to ammonia (NH_3) by nitrogenase enzymes (the nitrogen reduction reaction: N_2RR) has garnered substantial interest in the synthetic inorganic community for several decades.[1] In particular, the structural characterization of the FeMo-cofactor of biological nitrogen fixation,[2] and mechanistic uncertainties associated with this process,[3] have motivated studies of synthetic (primarily Mo and Fe) model systems that mediate N_2RR in the presence of proton and electron equivalents in organic solvent.[4-6] The mechanisms of these systems are at various stages of understanding. Experimental[4-6] and theoretical (predominantly Mo)[7] studies have been undertaken to provide insight.

Single-site iron model complexes, such as $P_3^BFe(N_2)^-$ and $P_3^BFe^+$ (**Figure 1**), catalyze N_2RR under a variety of conditions and driving forces, with reported selectivities (to date) for NH_3 generation as high as 72% based on reductant consumed.[4e] In addition, conditions have been reported under which $P_3^CFe(N_2)^-$ and $P_3^{Si}Fe(N_2)^-$ also catalyze N_2RR to varying degrees, with the $P_3^{Si}Fe$-system being far more efficient at the Hydrogen evolution reaction (HER) than N_2RR compared to P_3^BFe and P_3^CFe.[4d,8] We are naturally interested in understanding the mechanism/s by which catalysis in these respective systems occurs, and in exploring alternative systems that might function similarly. Of interest to the present study is the interplay between efficiency for the N_2RR and HER on the P_3^BFe scaffold and its isostructural congeners $P_3^{Si}Fe$ and P_3^CFe. In particular, can we elucidate some of the salient factors that dictate overall product selectivity for NH_3 versus H_2 in these respective systems?

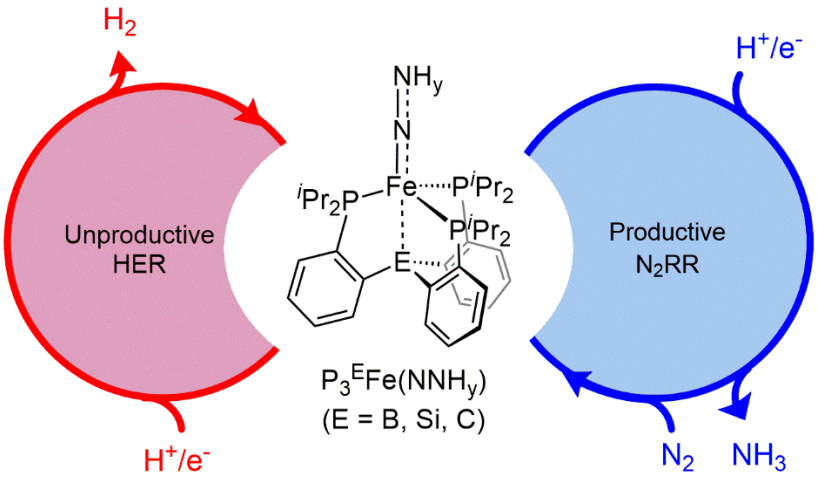

Figure 2.1. Schematic depiction of N_2RR/HER iron catalysts studied herein to explore key factors dictating product selectivity.

Herein we use DFT calculations to explore this question. We examine the comparative feasibility of HER via proton-coupled electron transfer (PCET)[9] from several putative Fe(N_xH_y) early intermediates, using electronic structure calculations coupled with predicted N–H bond strengths, thermodynamic driving forces, and electron-transfer (ET) kinetics as mechanistic probes. Acknowledging the likelihood that numerous and potentially competing factors may be at play, the formation, electronic structure, and reactivity of a key common intermediate, $Fe(NNH_2)^+$, is highlighted to be an important factor in the divergent selectivity profile of P_3^BFe (and P_3^CFe) relative to the $P_3^{Si}Fe$ system.

2.1. Computational Methods

All calculations were performed using dispersion corrected density functional theory (DFT-D_3) using Grimmes dispersion correction. 10 All calculations were done using the full P_3^EFe scaffold with the TPSS functional[11] and a def2-TZVP basis set on transition metals and a def2-SVP basis set on all other atoms.[12]

All stationary point geometries were optimized using NWChem 6.313 or Orca 3.0.3.[14] To ensure consistency in grid size, all reported single point and thermodynamic energies were performed using Orca 3.0.3. Frequency calculations were used to confirm the presence of true minima and to obtain gas phase free-energy values at 195 K (G_{gas}). Solvation corrections were performed using the COSMO-SMD continuum model.[15] The solvation free energy was approximated using gas phase and solvated single point energies ($\Delta G_{solv} \approx E_{soln} - E_{gas}$). Finally, the free-energy of the solvated species at 195 K was

calculated using the gas-phase free-energy and the solvation free-energy ($G_{soln,195K} = G_{gas,195K} + \Delta G_{solv}$).[16]

The accuracy of the described computational methodology was measured by comparison to several experimental benchmarks of interest. In addition to ensuring good agreement between computed and crystallographically determined structural data, experimentally determined bond dissociation enthalpies ($BDFE_{N-H}$) of the compounds $P_3^{Si}Fe(CNH)^+$, $P_3^{Si}Fe(CNH)$, $P_3^{Si}Fe(CNMeH)^+$, $P_3^{Si}Fe(CNMeH)$ and $P_3^{Si}Fe(NNMeH)^+$ could be faithfully reproduced within ±2 kcal/mol (See SI for full description).[4h] As a further point of calibration, the calculated singlet-triplet energy gap and the redox potentials of $P_3^{B}Fe(NNMe_2)$ and $P_3^{Si}Fe(NNMe_2)^+$ are in good agreement with the experimentally determined values (within ±1.5 kcal/mol, and ±3 kcal/mol (±130 mV vs $Fc^{+/0}$), respectively ; see Appendix 1).[4gh,17]

Reduction kinetics were calculated using the standard Marcus equation relating activation barrier with driving force and total reorganization energy ($\lambda_{tot} = \lambda_{is} + \lambda_{os}$).[18] The inner-sphere reorganization energy for electron transfer ($\lambda_{is,ET}$) was estimated assuming non-adiabatic behavior and by calculating the difference between the single point energies of the relevant species in its ground state and the corresponding single point energy of this ground state in the oxidized or reduced geometry (Eq. 1).

$$\lambda_{is,ET} = [E(Fe^{ox}{}_{ox}) - E(Fe^{ox}{}_{red})] + [E(Fe^{red}{}_{red}) - E(Fe^{red}{}_{ox})] \qquad (2.1)$$

The outer-sphere reorganization energy was calculated by assuming a barrier of 1.0 kcal/mol for the reduction of $P_3^{B}Fe(NNH_2)^+$ followed by calculation of λ_{tot} using this

barrier and λ_{is}, as calculated by Eq 1. A continuum solvation model was used to support this λ_{os} value (See SI for full description).[18] Reduction barriers for $P_3^{C/Si}Fe(NNH_2)^+$ were subsequently calculated relative to $P_3^{B}Fe(NNH_2)^+$.

2.2. Results and Discussion

To set the stage for the present study, previously reported catalytic N_2-to-NH_3 conversion studies by $P_3^{E}Fe$ (E = B, C, and Appendix A) under an atmosphere of N_2 at −78 °C in Et_2O, using KC_8 and $[H(OEt_2)_2][BAr^F_4]$ ($HBAr^F_4$, BAr^F_4 = tetrakis-(3,5-bis(trifluoromethyl)phenyl)borate) as the reductant and acid source,[4a,d] established $P_3^{B}Fe$ as the most efficient catalyst for N_2RR; the highest reported efficiency for this system (under these conditions) was 45 ± 3% (48 equiv acid; 58 equiv reductant). For comparison, the $P_3^{Si}Fe$ system provided a conversion efficiency of only 5 ± 3%. The $P_3^{C}Fe$ catalyst system was reasonably active at 36 ± 6% (note: ~25% lower substrate loading was used for this $P_3^{C}Fe$ value[4d]). Measurement of HER activity established $P_3^{Si}Fe(N_2)^-$ (88% per added acid equiv) as a significantly more efficient HER catalyst than $P_3^{B}Fe(N_2)^-$ (40% per added acid equiv) under analogous conditions.[4d] N_2RR catalysis by $P_3^{E}Fe$ (E = B, Appendix A) has also been studied in the presence of milder reagents (e.g., Cp^*_2Co and $[H_2NPH_2][OTf]$ or $[H_3NPh][OTf]$); under these conditions only the $P_3^{B}Fe$ system is catalytically active.

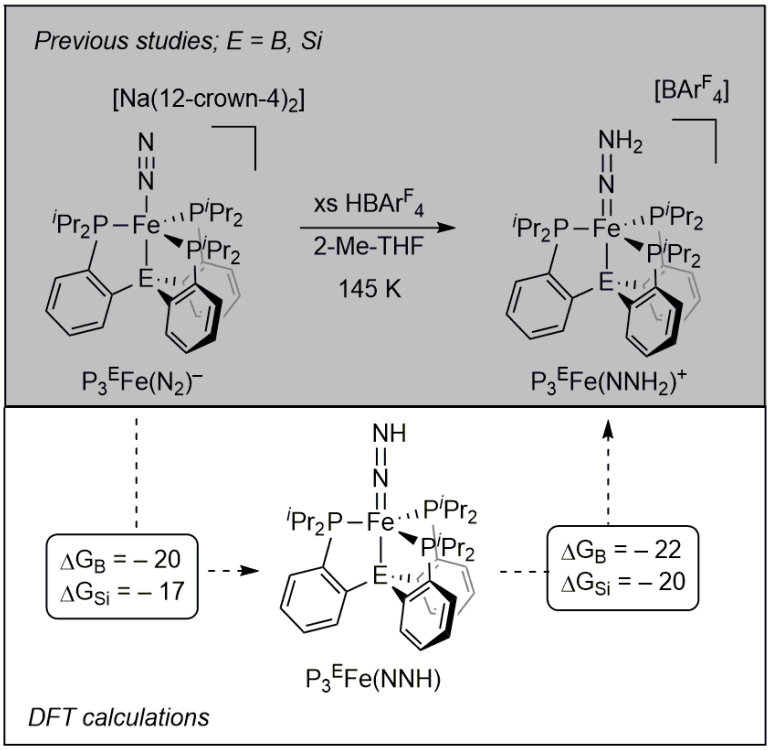

Figure 2.2. (top) Previous experimental work showing the formation of $P_3^EFe(NNH_2)^+$ (E = B or Appendix A) via protonation with excess acid.[4f,g] (bottom) Calculated free energy changes (in kcal/mol) for the formation of $P_3^EFe(NNH_2)^+$ via $P_3^EFe(NNH)$ (E = B or Appendix 1).

Previous studies of the P_3^BFe and $P_3^{Si}Fe$ systems have also explored the generation and characterization of early stage intermediates of the N_2RR catalysis.[4e,f,g] Most salient, low temperature protonation of $P_3^EFe(N_2)^-$ (E = B, Appendix A) with excess $HBAr^F_4$ affords the doubly protonated $P_3^EFe(NNH_2)^+$ species (Figure 2).[4f,g] As expected, corresponding DFT calculations (this work) are consistent with thermodynamically favored formation of $P_3^EFe(NNH)$ via proton transfer (Figure 2); another favorable proton transfer forms $P_3^EFe(NNH_2)^+$.

2.2.1. DFT Support for Slow Fe Protonation and Fast Fe-N_xH_y Formation

Although metal $H_y$dride (M–H) species are most typically invoked as intermediates of transition-metal catalyzed HER,[19] we do not think Fe–H species are the primary players in H_2 formation by the present systems. Several experimental observations are consistent with this idea. Foremost among them is that low temperature addition of stoichiometric acid (e.g., $HBAr^F_4$) to any of the anions, $P_3^EFe(N_2)^-$, causes overall oxidation to their corresponding neutral products, $P_3^EFe(N_2)$, along with release of 0.5 equiv H_2.[4a,d] This is notewortH_y because for E = Si or C the diamagnetic $H_y$dride products, $P_3^EFe(N_2)(H)$, are very stable species and are formed during catalysis as end products.[4b,d] We posit that reactive $P_3^EFe(N_xH_y)$ intermediates instead undergo net bimolecular HAT reactions to liberate H_2 via N_xH_y-ligand-mediated steps (*vida infra*). While iron $H_y$drides (Fe–H) can tie up the population of active catalyst, in our view they are unlikely to be intermediates of the dominant HER pathway.

To speak to this hypothesis computationally, we focus on one acid source, $HBAr^F_4$, as it has been the subject of the most extensive comparative study.[4d] The solid-state empirical formula of $HBAr^F_4$ reveals the presence of two ethers per $HBAr^F_4$ ($[(Et_2O)_2H][BAr^F_4]$).[20] To determine the preferred solution-state structure of this acid, optimizations were performed in which a Et_2OH^+ species was provided with 0, 1 or 2 explicit Et_2O molecules with which to $H_y$drogen bond. We found that $[(Et_2O)_2H]^+$ was lowest in free-energy, with $[(Et_2O)_3H]^+$ and $[Et_2OH]^+$ higher in energy by +7.0 and +8.2 kcal/mol, respectively.

The structure of $HBAr^F_4$ is particularly crucial for Fe protonation, as a pre-equilibrium formation of the $[Et_2OH]^+$ appears to be required, as evidenced by relaxed surface scans. The need for dissociation of Et_2O prior to Fe protonation provides a lower bound on the barrier of +8.2 kcal/mol. The requirement of $[Et_2OH]^+$ as the active acid, as opposed to $[(Et_2O)_2H]^+$, is presumably steric in origin and may speak, in part, to the importance of bulky isopropyl substituents in these catalysts. Our lab recently reported that a structurally related $P_3^{Si}Os(N_2)^-$ complex is an active catalyst N_2RR.[21] In contrast to the $P_3^EFe(N_2)^-$ catalysts, stoichiometric $HBAr^F_4$ addition can protonate at the metal, generating Os–H species that are not catalytically active for N_2RR. Steric access to the larger Os center is presumably less restricted than it is for Fe.

The structure of $HBAr^F_4$ is particularly crucial for Fe protonation, as a pre-equilibrium formation of the [Et2OH]+ appears to be required, as evidenced by relaxed surface scans. The need for dissociation of Et2O prior to Fe protonation provides a lower bound on the barrier of +8.2 kcal/mol. The requirement of [Et2OH]+ as the active acid, as opposed to [(Et2O)2H]+, is presumably steric in origin and may speak, in part, to the importance of bulky isopropyl-phosphino substituents in these catalysts. Our lab recently reported that a structurally related $P_3^{Si}Os(N_2)$- complex is an active catalyst for N_2RR. 21 In contrast to the $P_3^EFe(N_2)^-$ catalysts, stoichiometric $HBAr^F_4$ addition can protonate at the metal, generating Os-H species that are not catalytically active for N_2RR. Steric access to the larger Os center is presumably less restricted than it is for Fe.

The steric profile of the $Fe(N_2)$ unit suggests that functionalization of the β–N should not be subject to the same pre-equilibrium. This is consistent with relaxed surface scans, which show that the N_2 unit can be protonated in a concerted, low energy step in which an Et_2O molecule is favorably displaced by the nucleophilic β N-atom. Subsequent proton transfers yield Fe(NNH) with a low kinetic barrier (0.5–1.0 kcal/mol).

Fe–H formation is thermodynamically favored for all three scaffolds. We therefore presume that the dominant source of HER for these systems is not via Fe–H formation, but that Hydride species are formed over the course of catalysis as thermodynamic products. We presume that both HER and N_2RR, under the conditions explored in this work, are operating under kinetic control. In subsequent results and discussion, thermodynamics are assumed to be relevant within the context of kinetic parameters.

In addition to restricting our analysis to a single acid, $HBAr^F_4$, we focus on KC_8 as a reductant for several reasons. Most salient is that KC_8 is the only reductant that has been shown to produce catalytic yields of NH_3 for all scaffolds considered. This observation is attributed to the requirement of $Fe(N_2)^-$ formation during catalysis. While $P_3{}^BFe(N_2)^-$ can be formed with weaker reductants, namely Cp^*_2Co, the more reducing $P_3{}^{Si/C}Fe(N_2)^-$ is believed to be inaccessible under these conditions. Additionally, it has been noted that, when using KC_8 and $HBAr^F_4$, HER proceeds with similar initial rates on $P_3{}^{Si}Fe$ and $P_3{}^BFe$ scaffolds,[4d] possibly due to $Fe(N_2)$ reduction being a common rate limiting step.

Despite the need to restrict the scope of this study to a specific catalysis cocktail, many of the conclusions should extend to other conditions reported for N_2RR catalysis

using P_3^EFe (and related) complexes. In particular, the $BDFE_{N\text{-}H}$ values reported herein are acid and reductant independent and hence provide insight into the anticipated stability and reactivity profiles of key early intermediates of N_2RR.

2.2.2. Calculation of $BDFE_{N\text{-}H}$ Values for Fe–N_xH_y Intermediates

Early stage intermediates of the type Fe(NNH) and Fe(NNH_2) are expected to be highly reactive;[4e,h] thermochemical calculations reveal the presence of extremely weak N–H bonds in these systems, as shown by their calculated bond dissociation enthalpies ($BDFE_{N–H}$; Figure 2.3). In particular, as yet unobservable P_3^EFe(NNH) intermediates are predicted to have extremely weak N–H bonds (< 40 kcal/mol), and should therefore be subject to rapid bimolecular loss of H_2 and generation of $P_3^EFe(N_2)$. By contrast, the $BDFE_{N\text{-}H}$ values of candidate $P_3^EFe(N_xH_y)$ intermediates that are further downstream (e.g., Fe(N_2H_4), Fe(NH), Fe(NH_2)) are predicted to be significantly larger (Figure 2.3). This notion is consistent with the solution stability of characterized examples of such downstream intermediates, contrasting the high degree of solution instability of earlier intermediates.

Of particular interest herein is that the $BDFE_{N–H}$ values for the $P_3^{Si}Fe(NNH_2)^{n+}$ (n = 0, 1) system are lower than those for $P_3^{B/C}$, for a given overall charge. As discussed later, these different $BDFE_{N–H}$ values are rooted in the different valence electron counts, and hence electronic structures, of the respective P_3^EFe-systems.

For additional context, it is useful to consider reported $BDFE_{N–H}$ data for a related $P_3^{Si}Fe(CN)$-system. The relevant $P_3^{Si}Fe(CNH)$ species, isoelectronic with $P_3^{B}Fe(NNH)$, is calculated to have a weak $BDFE_{N–H}$ of 43.5 kcal/mol, in close agreement to that of 41.4 kcal/mol determined experimentally.4h Accordingly, $P_3^{Si}Fe(CNH)$ loses 0.5 equiv H_2 rapidly in solution to afford $P_3^{Si}Fe(CN)$. In contrast, its oxidized cation, $P_3^{Si}Fe(CNH)^+$, has a much higher $BDFE_{N–H}$ (61.8 kcal/mol (calc); 61.9 kcal/mol (exp)); this species is stable to H_2 loss in solution and can be isolated and structurally characterized.

Considering these collected data and observations, and additional data discussed below, we presume that the earliest N_2RR intermediates in $P_3^{E}Fe$-systems are very important for determining N_2RR versus HER selectivity; they engage in bimolecular H_2-evolving reactions that compete with productive N_2RR. We next consider aspects of the H–H bond-forming steps in these early $P_3^{E}Fe(N_xH_y)$ intermediates in more detail.

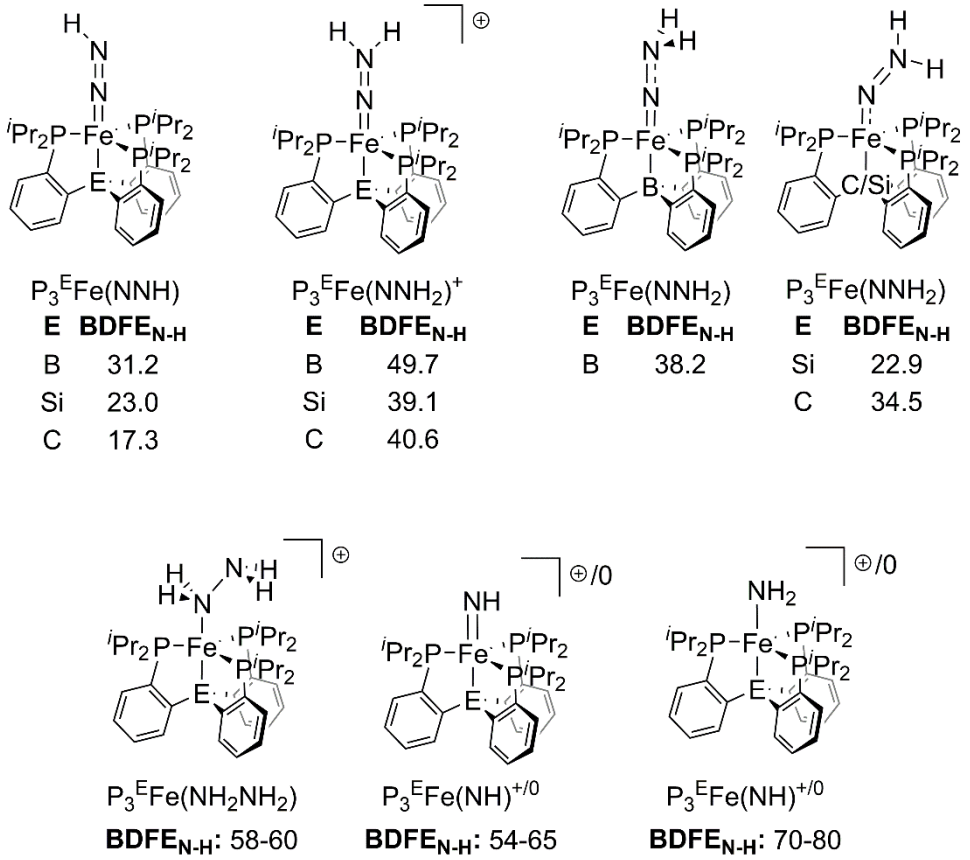

Figure 2.3. $BDFE_{N–H}$ values (in kcal/mol) for selected $P_3^EFe(N_xH_y)$ species.[22]

$P_3^EFe(NNH)$ species are plausible candidates to consider with respect to selectivity since bimolecular H_2-evolving reactions can presumably result from their extremely weak N−H bonds (Figure 2.3; 31-17 kcal/mol). $P_3^{Si}Fe(NNH)$, with a $BDFE_{N–H}$ estimated to be 8.2 kcal/mol lower than for $P_3^BFe(NNH)$, might be reasonably expected to liberate H_2 more readily, thereby attenuating its N_2RR efficiency. However, the $BDFE_{N–H}$ for $P_3^CFe(NNH)$ is calculated to be even lower (17.3 kcal/mol) than for $P_3^{Si}Fe(NNH)$ (23 kcal/mol), despite the fact that $P_3^CFe(N_2)^-$ is appreciably more efficient for N_2RR. Hence, a trend is not evident on the basis of the Fe(NNH) intermediates, at least as related to their relative

$BDFE_{N–H}$ values. Fe(NNH) intermediates are readily protonated to form $Fe(NNH_2)^+$ species in solution at low temperature (Figure 2.2). This likewise suggests that Fe(NNH) intermediates are unlikely to be primarily responsible for HER under catalytic conditions when a large excess of acid is present.[4f,g]

$P_3^EFe(NNH_2)$ $BDFE_{N–H}$ values provide a more tractable trend: the respective calculated values are 38.2 kcal/mol for P_3^BFe, 34.4 kcal/mol for P_3^CFe, and 22.9 kcal/mol for $P_3^{Si}Fe$; the $P_3^EFe–NNH_2$ species that exhibits the most efficient N_2RR activity exhibits the strongest N-H bond, and the least efficient exhibits the weakest (Figure 2.3).

2.2.3. Calculated Reduction Kinetics of $P_3^EFe(NNH_2)^+$

To gain further insight into the respective role $P_3^EFe(NNH_2)^{+/0}$ (E = B, Si, C) species might play in dictating product selectivity, $P_3^EFe(NNH_2)^+$ reduction kinetics were derived using the standard Marcus equation relating the driving force and total reorganization energy with the ET activation barrier.[18] Comparison of the optimized $Fe(NNH_2)$ and $Fe(NNH_2)^+$ redox pairs reveals significant differences in their respective reduction potentials and inner-sphere reorganization energies ($\lambda_{is,ET}$).

The $P_3^BFe(NNH_2)^+$ species is predicted to have a considerably more positive reduction potential (−1.2 V vs $Fc^{+/0}$) than $P_3^{Si}Fe(NNH_2)^+$ (−1.9 V; Table 2.1), resulting from their different valence electronic counts and electronic structures (see below). Given their dramatic difference in reduction potentials, the barrier for reduction (G*) is expected to sharply increase in moving from B to Si. Relative reduction barrier calculations,

assuming G* = 1.0 kcal/mol for the reduction of $P_3^BFe(NNH_2)^+$, predict activation barriers that are 4–5 times higher in energy for the reduction of $P_3^{C/Si}Fe(NNH_2)^+$ versus $P_3^BFe(NNH_2)^+$ (Table 2.1). While the reduction of all three species should be more than readily accomplished by the strong reductant KC_8, $P_3^{C/Si}Fe(NNH_2)^+$ species are predicted to be significantly longer lived than the $P_3^BFe(NNH_2)^+$ congener.

The $P_3^BFe(NNH_2)^+$ intermediate is predicted to have a lower propensity for H_2-liberating PCET reactivity, and is also predicted to be reduced much more rapidly. Since the reaction of two $P_3^BFe(NNH_2)$ molecules is a more probable source of H_2 on this scaffold, the efficiency for N_2RR on P_3^BFe should be strongly coupled to the rate at which $P_3^BFe(NNH_2)$ can be productively consumed (i.e., protonated to form a $P_3^BFe(NHNH_2)^+$ or $P_3^BFe(NNH_3)^+$). Mechanistic experiments to address these scenarios are ongoing. For example, a recent study has provided experimental evidence that $P_3^BFe(NNH_2)$ is protonated by acid at low temperature to liberate $P_3^BFe(N)^+$ and NH_3, presumably via $P_3^BFe(NNH_3)^+$.

We conclude that facile reduction of $P_3^BFe(NNH_2)^+$ to $P_3^BFe(NNH_2)$, relative to that for $P_3^{Si}Fe(NNH_2)^+$ and $P_3^CFe(NNH_2)^+$, is one important factor in determining its comparative efficiency for N_2RR. As further elaborated below, long-lived $P_3^EFe(NNH_2)^+$ intermediates can, via bimolecular PCET pathways, instead lead to unproductive HER. This HER activity, however, is dependent on both a long-lived $P_3^EFe(NNH_2)^+$ intermediate, and the presence of a highly reactive PCET reagent, such as a $P_3^EFe(NNH_2)$ species. We have previously postulated that $P_3^EFe(NNH_2)$ formation is required for the release of the

first equivalent of NH_3 and thus suggest that this species may be a crucial intermediate in both HER and N_2RR.[4fg,17]

Table 2.1. Calculated thermodynamic and kinetic parameters for $P_3^EFe(NNH_2)^+$ a $P_3^EFe(NNH_2)$[a]

$P_3^EFe(NNH_2)^+ + e^- \rightarrow P_3^EFe(NNH_2)$				
	E^o (vs $Fc^{+/0}$)	$\lambda_{is,ET}$	G^*_{rel}	k_{rel}[b]
E =B	−1.2 V	23	1.0	1
E = Si	−1.9 V	30	4.4	$2x10^{-4}$
E = C	−2.0 V	30	5.2	$2x10^{-5}$

[a]Energies are in kcal/mol, unless noted otherwise. [b]G^*_{rel} values were calculated assuming a $P_3^BFe(NNH_2)^+$ reduction barrier of 1.0 kcal/mol. $k_{rel} \equiv \exp[(G^*_B - G^*_E)/kbT]$ where T = 195 K.

2.2.4. Calculated PCET Reactions

The differences in N–H bond strengths and relative rates of $P_3^EFe(NNH_2)^+$ reduction, with corresponding implications for product selectivity, are further highlighted by calculating the thermodynamic and kinetic parameters for several PCET reactions of interest (Figure 2.4ABC). In particular, comparative driving forces were calculated for unproductive bimolecular PCET reactions that generate H_2 between $P_3^EFe(NNH_2)^{n+}$ (n = 0,1; E = B, Si, C) and $P_3^EFe(NNH_2)$. Consistent with the calculated $BDFE_{N–H}$ values (Figure 2.3), the $P_3^{Si}Fe$, and to a lesser extent the P_3^CFe, system shows a higher propensity

to undergo PCET to liberate H_2 and the corresponding reduced Fe–NNH_y species. This is especially apparent in the reaction between two $P_3^EFe(NNH_2)^+$ species, and in the cross-reaction between an $P_3^EFe(NNH_2)^+$ cation and a neutral $P_3^EFe(NNH_2)$ species.

In the former case, two $P_3^EFe(NNH_2)^+$ (E = Si, C) species react in a very favorable step to form 0.5 equiv H_2 and $P_3^EFe(NNH)^+$ (ΔG_{calc} = −17.5 kcal/mol and −16.5, respectively; Figure 2.4A). The reaction barrier is expected to be dominated in this case by the work required to bring two cationic species together in solution (~5 kcal/mol; see APPENDIX A), highlighting the reactive *Nature* of $P_3^{C/Si}Fe(NNH_2)^+$. In contrast, $P_3^BFe(NNH_2)^+$ shows a correspondingly uphill PCET reaction (ΔG_{calc} = +3.1 kcal/mol) in its self-combination to liberate H_2 and $P_3^BFe(NNH)^+$;[23] $P_3^BFe(NNH_2)^+$ is also much more readily reduced to $P_3^BFe(NNH_2)$ (Table 2.1).

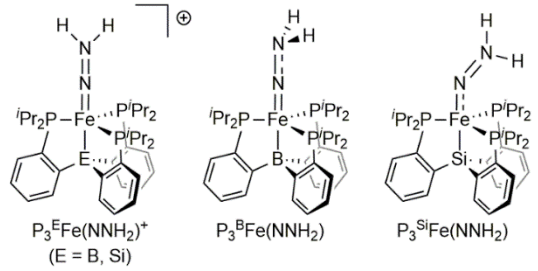

		ΔGcalc	
		E = B	E = Si
A	$P_3^EFe(NNH_2)^+ \xrightarrow{-0.5\ H_2} P_3^EFe(NNH)^+$	+3.1	-17.5
B	$P_3^EFe(NNH_2) \xrightarrow{-0.5\ H_2} P_3^EFe(NNH)$	-22.7	-54.9
C	$P_3^EFe(NNH_2)^+ + P_3^EFe(NNH_2) \xrightarrow{-H_2} P_3^EFe(NNH)^+ + P_3^EFe(NNH)$	-9.8	-36.0

Figure 2.4. Calculated free energy changes (ΔG_{calc}; in kcal/mol; 195 K) for several putative PCET reactions that evolve H_2.

The bimolecular reaction between cationic $P_3^EFe(NNH_2)^+$ with $P_3^EFe(NNH_2)$ to produce H_2 and the corresponding $P_3^EFe(NNH)^+$ and $P_3^EFe(NNH)$ byproducts is predicted to be favorable for all three systems (Figure 2.4C). However, the $P_3^{C/Si}Fe$ systems proceed with far more driving force than the P_3^BFe system.

Favorable driving forces are also predicted for all three systems in self reactions of $P_3^EFe(NNH_2)$ to produce H_2 and $P_3^EFe(NNH)$, but again the $P_3^{C/Si}Fe$ systems proceed with far more driving force (Figure 2.4B). While the bimolecular reaction of $P_3^EFe(NNH_2)$ with itself is therefore a presumed source of H_2 for each system, in sum the $P_3^{C/Si}Fe$ systems are more likely, under each of the considered bimolecular reactions, to liberate H_2, in accord with their efficiency for HER versus N_2RR relative to the P_3^BFe system.

Given that the reduction of $P_3^{C/Si}Fe(NNH_2)^+$ is predicted to be comparatively slow, one might expect such a species to build-up as an intermediate. This possibility warrants future experimental studies aimed at in situ detection. At the present stage, we can suggest that a high (relative) concentration of $P_3^{C/Si}Fe(NNH_2)^+$, and a high predicted propensity for HER via reaction of this species with either itself or $P_3^{C/Si}Fe(NNH_2)$, leads to unproductive PCET steps that evolve H_2 as competitive with downstream N_2 reduction steps that lead to N_2RR. This is one important factor in determining selectivity.

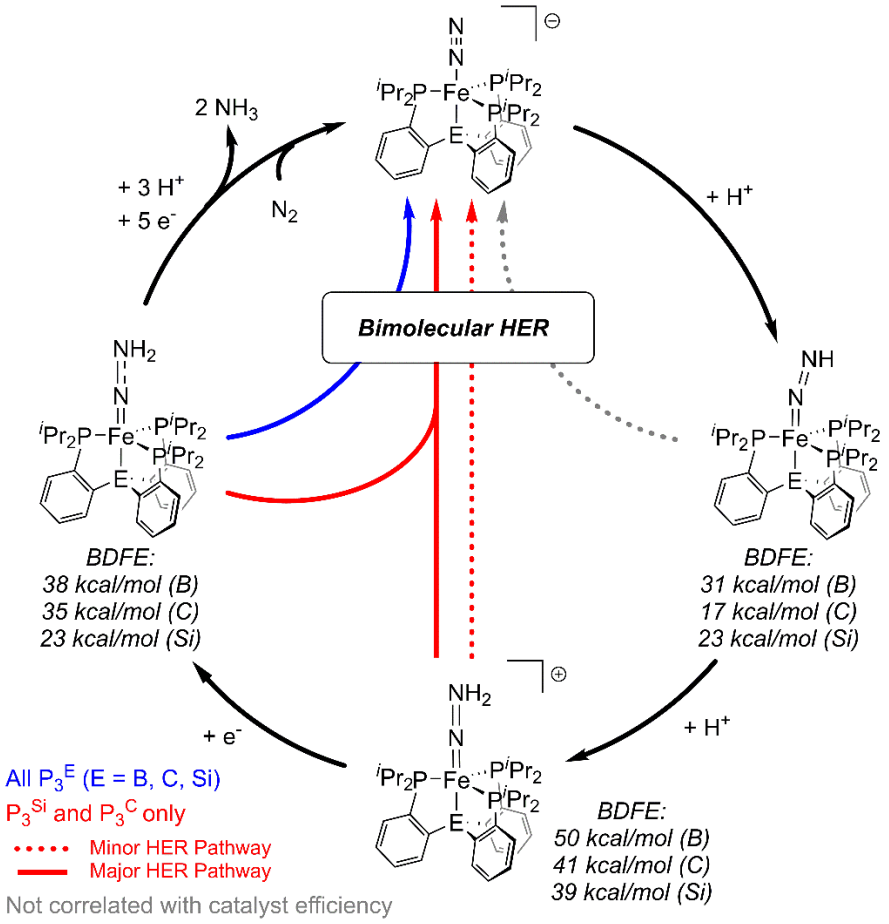

Figure 2.5. Overview of predicted bimolecular HER and N_2RR pathways for $P_3^EFe(NNH_y)$ species and pertinent $BDFE_{N–H}$ values.

Since the $P_3^BFe(NNH_2)^+$ intermediate is predicted to have a lower propensity for H_2-liberating PCET reactivity, and is also predicted to be reduced much more rapidly, the reaction of two $P_3^BFe(NNH_2)$ molecules is a more probable source of H_2 for this scaffold; the efficiency for N_2RR on P_3^BFe should therefore be related to the rate at which $P_3^BFe(NNH_2)$ can be productively consumed (i.e., protonated to form a $P_3^BFe(NHNH_2)^+$ or $P_3^BFe(NNH_3)^+$). Mechanistic experiments to address these scenarios are ongoing. For

example, a recent study has shown that $P_3^BFe(NNH_2)$ can be protonated by strong acid at low temperature to liberate $P_3^BFe(N)^+$ and NH_3, presumably via $P_3^BFe(NNH_3)^+$.[17]

While the P_3^CFe scaffold provides a less definitive comparison, the calculated $BDFE_{N–H}$ values and H_2-evolving PCET thermodynamics suggest that the dominant source of HER on the $P_3^{C/Si}Fe$ scaffolds may be the reaction between $Fe(NNH_2)$ and $Fe(NNH_2)^+$. The highly reducing nature of $P_3^CFe(NNH_2)^+$, as for the P_3^{Si} scaffold, suggests it should be comparatively long-lived, and thus more likely to undergo PCET with $P_3^CFe(NNH_2)$. The similarity between P_3^CFe and $P_3^{Si}Fe$ in their thermodynamics for the reaction between two $Fe(NNH_2)^+$ species (Figure 2.4A) does not correlate with their disparate $\%NH_3$ efficiencies. Substantial differences in their predicted thermodynamics for the reaction between $Fe(NNH_2)$ and $Fe(NNH_2)^+$ (Figure 2.4C) are more in line with the observed trend. This type of bimolecular reactivity may be an important source of HER on the $P_3^{C/Si}Fe$ scaffolds (Figure 2.5).

2.2.5. Wiberg Bond Indices of $P_3^EFe(N_xH_y)$ Species

We next examine how each P_3^E auxiliary, and the corresponding $P_3^EFe(NNH_y)$ valence at iron, confers variability in bonding to, and the electronic structure of, the NNH_y ligand, as a means of further considering corresponding reactivity differences of $P_3^EFe(NNH_y)$ species.

Wiberg bond indices provide a means to examine how the localized bonding between various atoms, expressed as a bond index,[24] changes as a function of the NNH_y

reduction state (i.e., NNH to NNH_2). We have suggested elsewhere that the relative flexibility of the P_3^B ligand, owing to a weak and dative Fe-B interaction, may allow for stabilization of Fe−NNH_y intermediates where Fe–N π-bonding is accompanied by pyramidalization at the Fe center, and a corresponding lengthening of the Fe–B distance.[4a,17,25] The P_3^{Si} ligand is expected to give rise to a more shared, covalent Fe–Si interaction, irrespective of the NNH_y reduction state, and the P_3^C system may be expected to fall in the middle of these extremes.[4b]

Changes in the respective bond indices of these frameworks have been determined between pairs of P_3^EFe(NNH) and P_3^EFe(NNH_2) species (E = B, C, Appendix A), related by formal addition of an H-atom to the former. Interestingly, the N–H bond indices are essentially invariant across all complexes studied, indicating that differences in $BDFE_{N–H}$ are mostly dependent on the relative bonding through the E–Fe–N–N manifold.[26] The most salient data, reproduced in Figure 2.6, are the total Wiberg bond indices for Fe−N_α, Fe−N_β, Fe−E, N−N and N−H. The total Fe−N–N bond order, ∑(Fe−N−N), is also provided, as is the net difference in the $\Delta BDFE_{N-H}$ value, for each pair on moving from Fe(NNH) to Fe(NNH_2).

As expected, the Fe–E bond order weakens slightly from Fe(NNH) to Fe(NNH_2) for E = B, and stays constant for both Si and C. The respective change at Fe-N_α is also informative. For the B system, a significant increase is observed (1.6 to 1.9), reflecting a build-up in pi-bonding in P_3^BFe(NNH_2), akin to low-spin (pseudotetrahedral) iron imides

of the type $P_3^BFe(NR)$. For comparison, a previously characterized $P_3^BFe(NR)$ species (R = 4-OMe-Ph) is predicted to have an Fe–N bond order of 1.8 (see Appendix A).

By contrast, the Fe–Nα index for Si is sharply attenuated (from 1.6 to 1.2), reflecting a corresponding decrease in pi bonding. While this difference must partly reflect a less flexible Fe-Si interaction, it also reflects the electronic structure resulting from an extra electron in the frontier orbitals of the ^2E $\{Fe\text{-}Si\}^7$ system relative to ^1A $\{Fe\text{-}B\}^6$. Interestingly, $P_3^BFe(NNH_2)$ is pyramidalized at N_β whereas N_β is planar for $P_3^{Si}Fe(NNH_2)$. This observation can again be rationalized by the assignment of a low-spin iron "imide-like" electronic structure to $\{Fe\text{-}B\}^6$ $P_3^BFe(NNH_2)$, but not for $\{Fe\text{-}Si\}^7$ $P_3^{Si}Fe(NNH_2)$, where substantial spin leaks onto the NNH_2 subunit (19% on $P_3^{Si}Fe(NNH_2)$). The C system provides an interesting further comparison, with spin leakage onto the NNH_2 unit falling between these two extremes (12% on $P_3^CFe(NNH_2)$). An increase in the Fe-Nα index occurs from $P_3^CFe(NNH)$ to $P_3^CFe(NNH_2)$ (1.2 to 1.4), but N_β is predicted to remain planar.

There also appears to be a strong trend between the degree of change in the total Fe−N−N bond order (∑(Fe−N−N)) and the $\Delta BDFE_{N\text{-}H}$; The B and C systems show little change in ∑(Fe−N−N), with a corresponding significant increase in $BDFE_{N\text{-}H}$ from Fe(NNH) to $Fe(NNH_2)$ (7.0 and 17.9 kcal/mol, respectively). However, the P_3^CFe system starts at a much weaker $BDFE_{N\text{-}H}$ of 17.3 kcal/mol for $P_3^CFe(NNH)$ (compared to 31.2 kcal/mol for P_3^BFe). This observation is consistent with their total ∑(Fe−N−N) values (3.8 for B and 2.9 for C). Thus, the comparative stability of $P_3^CFe(NNH_2)$, with its much higher $BDFE_{N\text{-}H}$ relative that in $P_3^CFe(NNH)$, appears to reflect a higher degree of instability in

$P_3^{C}Fe(NNH)$ (relative to the same comparison for E = B). This idea is further supported by Wiberg bond indices of the $P_3^{E}Fe(N_2)$ species, which show a total bond order of 4.0 across the Fe–N–N unit for all three scaffolds (Figure 2.6).

In sharp contrast, the $P_3^{Si}Fe$ system has a relatively high ∑(Fe−N−N) value in $P_3^{Si}Fe(NNH)$, but this value decreases dramatically in $P_3^{Si}Fe(NNH_2)$. There is correspondingly very little change in the $\Delta BDFE_{N\text{-}H}$, reflecting a comparatively very weak N-H bond in $P_3^{Si}Fe(NNH_2)$. The instability of $P_3^{Si}Fe(NNH_2)$, with an electronic structure that places substantial unpaired spin on NNH_2 owing to the $\{Fe\text{-}Si\}^7$ configuration, presumably contributes to the cathodically shifted reduction potential predicted for $P_3^{Si}Fe(NNH_2)^+$ relative to $P_3^{B}Fe(NNH_2)^+$, and also its propensity for facile PCET to liberate H_2.

In sharp contrast, the $P_3^{Si}Fe$ system has a relatively high ∑(Fe−N−N) value in $P_3^{Si}Fe(NNH)$, but this value decreases dramatically in $P_3^{Si}Fe(NNH_2)$. There is correspondingly very little change in the $\Delta BDFE_{N\text{-}H}$, reflecting a comparatively very weak N-H bond in $P_3^{Si}Fe(NNH_2)$. The instability of $P_3^{Si}Fe(NNH_2)$, with an electronic structure that places substantial unpaired spin on NNH_2 owing to the {Fe-Si}7 configuration, presumably contributes to the cathodically shifted reduction potential predicted for $P_3^{Si}Fe(NNH_2)^+$ relative to $P_3^{B}Fe(NNH_2)^+$, and also its propensity for facile PCET to liberate H_2.

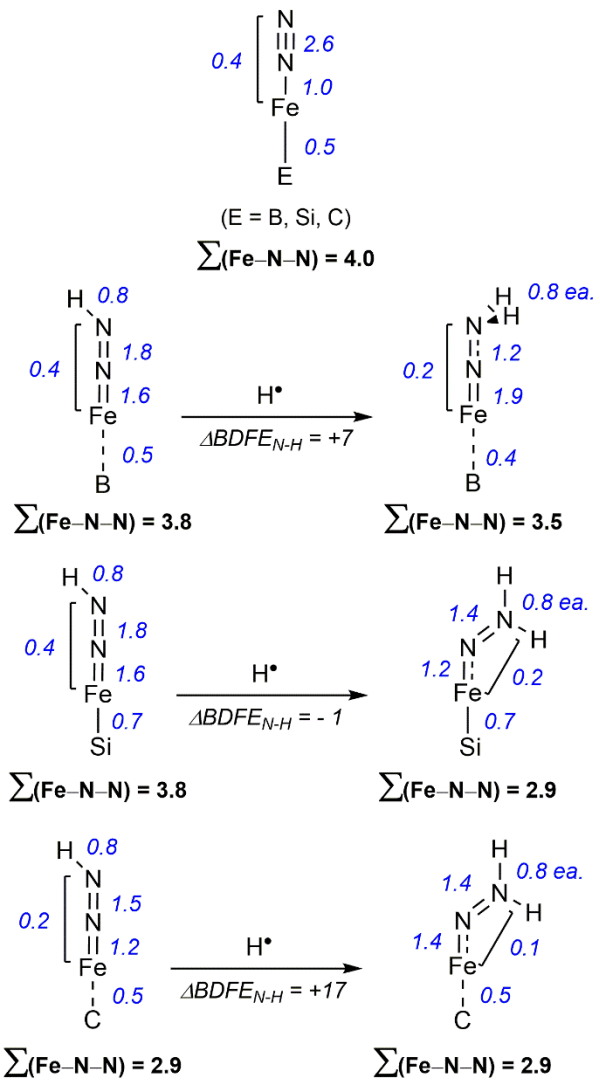

Figure 2.6. Selected total Wiberg bond indices for $P_3^EFe(N_2)$, $P_3^EFe(NNH)$ and $P_3^EFe(NNH_2)$ species, along with the total Fe−N–N bond order, ∑ (Fe−N−N). $\Delta BDFE_{N\text{-}H}$ values are reported in kcal/mol.

2.3. Conclusions

Exploring the chemical basis for N_2RR versus HER selectivity for a molecular catalyst is important to future catalyst design. The DFT study described herein suggests

that PCET reactions involving $P_3^EFe(NNH_2)^{n+}$ species likely play an important role in the efficiency of N_2-to-NH_3 conversion catalysis by P_3^EFe model systems. These calculations enable predictions qualitatively consistent with previous stoichiometric and catalytic experiments. The comparative stability of $P_3^EFe(NNH_2)^{n+}$ intermediates, as predicted by calibrated $BDFE_{N–H}$ values and redox potentials, emerges as one of the important factors in determining selectivity for N_2RR versus HER in these systems. Corresponding Wiberg bond indices intimate P_3^B as an especially well-equipped ligand for supporting N_2RR at Fe, due to its high degree of flexibility and the valence electron count it confers to Fe in the reduced intermediate $P_3^BFe(NNH_2)$. Our study suggests that increasing the rate at which an $P_3^EFe(NNH_2)$ intermediate is productively consumed so as to avoid bimolecular HER, possibly via rapid PCET reagents, may be a promising route to increasing efficiency for NH_3 production.

Looking beyond these iron model systems, our study underscores the potential utility of DFT-predicted $BDFE_{N-H}$ determinations towards the rational design of catalysts for N_2RR. Intermediates with weak N–H bonds (e.g., M(NNH) and $M(NNH_2)$) are highlighted as important sources of H_2 production via bimolecular PCET. Such a scenario is distinct from HER activity via more traditional metal-$H_y$dride intermediates.

2.4. References

[1] (a) Chatt, J.; Dilworth, J. R.; Richards, R. L. *Chem. Rev.* **1978**, *78*, 589-625. (b) Schrock, R. R. *Acc. Chem. Res.* **2005**, *38*, 955-962. (c) Nishibayashi, Y. *Inorg. Chem.* **2015**, *54*,

9234−9247. (d) van der Ham, C. J. M.; Koper, M. T. M.; Hetterscheid, D. G. H. *Chem. Soc. Rev.* **2014**, *43*, 5183−5191. (e) Shaver, M. P.; Fryzuk, M. D. *Adv. Synth. Catal.* **2003**, *345*, 1061−1076. (f) MacLeod, K. C.; Holland, P. L. *Nat. Chem.* **2013**, *5*, 559−565.

[2] (a) Howard, J. B.; Rees, D. C. *Proc. Nat. Acad. Sci.* **2006**, *103*, 17088-17093. (b) Howard, J. B.; Rees, D. C. *Chem. Rev.* **1996**, *96*, 2965−2982.

[3] Hoffman, B. M.; Lukoyanov, D.; Yang, Z.-Y.; Dean, D. R.; Seefeldt, L. C. *Chem. Rev.* **2014**, *114*, 4041−4062.

[4] For pertinent Fe systems: (a) Anderson, J. S.; Rittle, J.; Peters, J. C. *Nature* **2013**, *501*, 84−87. (b) Creutz, S. E.; Peters, J. C. *J. Am. Chem. Soc.* **2014**, *136*, 1105−1115. (c) Ung, G.; Peters, J. C. *Angew. Chem., Int. Ed.* **2015**, *54*, 532−535. (d) Del Castillo, T. J.; Thompson, N. B.; Peters, J. C. *J. Am. Chem. Soc.* **2016**, *138*, 5341–5350. (e) Chalkley, M. J.; Del Castillo, T. J.; Matson, B. D.; Roddy, J. P.; Peters, J. C. *ACS Central Science* **2017**, *3*, 217-223. (f) Anderson, J. S.; Cutsail, G. E.; Rittle, J.; Connor, B. A.; Gunderson, W. A.; Zhang, L.; Hoffman, B. M.; Peters, J. C. *J. Am. Chem. Soc.* **2015**, *137*, 7803–7809. (g) Rittle, J.; Peters, J. C. *J. Am. Chem. Soc.* **2016**, *138*, 4243–4248. (h) Rittle, J.; Peters, J. C. *J. Am. Chem. Soc.* **2017**, *139*, 3161–3170.

[5] For Mo systems: (a) Kuriyama, S.; Arashiba, K.; Nakajima, K.; Matsuo, Y.; Tanaka, H.; Ishii, K.; Yoshizawa, K.; Nishibayashi, Y. *Nat. Commun.* **2016**, *7*, 12181. (b) Yandulov, D. V.; Schrock, R. R. *Science* **2003**, *301*, 76−78. (c) Arashiba, K.; Miyake, Y.; Nishibayashi, Y. *Nat. Chem.* **2011**, *3*, 120−125. (d) Kuriyama, S.; Arashiba, K.; Nakajima, K.; Tanaka, H.; Kamaru, N.; Yoshizawa, K.; Nishibayashi, Y. *J. Am. Chem. Soc.* **2014**,

136, 9719−9731. (e) Arashiba, K.; Kinoshita, E.; Kuriyama, S.; Eizawa, A.; Nakajima, K.; Tanaka, H.; Yoshizawa, K.; Nishibayashi, Y. *J. Am. Chem. Soc.* **2015**, *137*, 5666−5669.

[6] For Co systems: (a) Del Castillo, T. J.; Thompson, N. B.; Suess, D. L. M.; Ung, G.; Peters, J. C. *Inorg. Chem.* **2015**, *54*, 9256–9262. (b) Kuriyama, S.; Arashiba, K.; Tanaka, H.; Y. Matsuo, Y.; Nakajima, K.; Yoshizawa, K.; Nishibayashi, Y. *Angew. Chem. Int. Ed.* **2016**, *55*, 14291–14295.

[7] (a) Reiher, M.; Le Guennic, B.; Kirchner, B. *Inorg. Chem.* **2005**, *44*, 9640–9642. (c) Studt, F.; Tuczek, F. *Angew. Chem. Int. Ed.* **2005**, *44*, 5639–5642. (d) Studt, F.; Tuczek, F. *J. Comput. Chem.* **2006**, *27*, 1278–1291. (e) Ujjal Gogoi, U.; Kanti Guha, A.; Phukan, A. K. *Chem. Eur. J.* **2013**, *19*, 11077–11089.

[8] Side-by-side comparisons of catalytic N_2RR by P_3^EFe (E = B, C, and Appendix A) using potassium graphite (KC_8) and $[(Et_2O)_2H][BAr^F{}_4]$ ($HBAr^F{}_4$, BArF4 = tetrakis-(3,5-bis(trifluorometH$_y$l)phenyl)borate) have revealed P_3^BFe to be the most efficient catalyst, with reported efficiencies up to 37%. N_2RR catalysis by P_3^CFe or P_3^{Si}Fe is less efficient under these conditions, with reported efficiencies of 33% and 4%, respectively. Studies focused on HER catalysis have shown $P_3^{Si}Fe(N_2)$- (88% per H+) to be significantly more efficient than $P_3^BFe(N_2)$- (40% per H+) under analogous conditions. See 4d.

[9] In this study, we do not distinguish between the terms H-atom transfer (HAT) vs PCET. For consistency, we refer to PCET throughout. For discussion of terminology see: (a) Warren, J. J.; Tronic, T. A.; Mayer, J. M. *Chem. Rev.* **2010**, *110*, 6961–7001. (b) Hammes-Schiffer, S. *J. Am. Chem. Soc.* **2015**, *137*, 8860−8871.

[10] Grimme, S.; Antony, J.; Ehrlich, S.; Krieg, H. *J. Chem. Phys.* **2010**, *132*, 154104.

[11] Tao, J. M.; Perdew, J. P.; Staroverov, V. N.; Scuseria, G. E. *Phys. Rev. Lett.* **2003**, *91*, 146401.

[12] Weigend, F.; Ahlrichs, R. *Phys. Chem. Chem. Phys.* **2005**, *7*, 3297–3305.

[13] Valiev, M.; Bylaska, E. J.; Govind, N.; Kowalski, K.; Straatsma, T. P.; Van Dam, H. J. J.; Wang, D.; Nieplocha, J.; Apra, E.; Windus, T. L.; de Jong, W. A. *Comput. Phys. Commun.* **2010**, *181*, 1477–1489.

[14] Neese, F. *Wiley Interdiscip. Rev. Comput. Mol. Sci.* **2012**, *2*, 73-78.

[15] (a) Klamt, A.; Schüürmann, G. *J. Chem. Soc. Perkin Trans. 2.* **1993**, *2*, 799–805. (b) Marten, B.; Kim, K.; Cortis, C.; Friesner, R. A.; Murphy, R. B.; Ringnalda, M. N.; Sitkoff, D.; Honig, B. *J. Phys. Chem.* **1996**, *100*, 11775–11788.

[16] (a) Ribeiro, R. F.; Marenich, A. V.; Cramer, C. J.; Truhlar, D. G. *J. Phys. Chem. B* **2011**, *115*, 14556–14562. (b) Wang, T.; Brudvig, G.; Batista, V. S. *J. Chem. Theory Comput.* **2010**, *6*, 755–760. (c) Marten, B.; Kim, K.; Cortis, C.; Friesner, R. A.; Murph$_y$, R. B.; Ringnalda, M. N.; Sitkoff, D.; Honig, B. *J. Phys. Chem.* **1996**, *100*, 11775–11788.

[17] Thompson, N.B.; Green, M. T.; Peters, J.C. *J. Am. Chem. Soc.*, **2017**, *139*, 16105-16108.

[18] Marcus, R. A. *J. Chem. Phys.* **1956**, *24*, 966–978.

[19] (a) Dempsey, J. L.; Brunschwig, B. S.; Winkler, J. R.; Gray, H. B. *Acc. Chem. Res.* **2009**, *42*, 1995–2004. (b) Lewandowska-Andralojc, A.; Baine, T.; Zhao, X.; Muckerman, J. T.; Fujita, E.; Polyansky, D. E. *Inorg. Chem.* **2015**, *54*, 4310–4321. (c) Yang, J. Y.; Smith, S. E.; Liu, T.; Dougherty, W. G.; Hoffert, W. A.; Kassel, W. S.; DuBois, M. R.; DuBois, D. L.; Bullock, R. M. *J. Am. Chem. Soc.* **2013**, *135*, 9700–9712.

[20] Brookhart, M.; Grant, B.; Volpe Jr., A. F. *Organometallics* **1992**, *11*, 3920–3922.

[21] Fajardo, J.; Peters, J. C. *J. Am. Chem. Soc.* **2017**, *139*, 16105–16108.

[22] We have previously reported bond dissociation enthalpies ($BDE_{N\text{-}H}$) for $P_3^BFe(NNH)$ and $P_3^BFe(NNH_2)$ (see ref 4e). Here we reported $BDFE_{N\text{-}H}$ values as they have more theoretical justification in the absence of experimental knowledge of the entropy change associated with H· loss.

[23] While this discussion may seem at odds with the enhanced stability of $P_3^{Si}Fe(NNH_2)^+$ relative to $P_3^BFe(NNH_2)^+$, other factors are presumably responsible in solution, such as the more facile reduction of $P_3^BFe(NNH_2)^+$ relative to $P_3^{Si}Fe(NNH_2)^+$.

[24] Wiberg, K. B. *Tetrahedron*, **1968**, *24*, 1083-1096.

[25] Moret, M-.E.; Peters, J. C. *J. Am. Chem. Soc.*, **2011**, *133*, 18118-18121.

[26] Similarly, the C_2H_5 radical is predicted to have a very low $BDFE_{C\text{-}H}$ (34 kcal/mol) when compared to C_2H_4 (100 kcal/mol), but the Wiberg bond indices for their respective C–H bonds do not change appreciably (See Appendix A)

Chapter 3. Catalytic N_2-to-NH_3 Conversion by Fe at Lower Driving Force: A Proposed Role for Metallocene-Mediated PCET

Reproduced in part with permission from:

Chalkley, M. J.; Del Castillo, T. J.; Matson, B. D.; Roddy, J. P.; Peters, J. C.

ACS Central Science, **2017**, 3, 217-223.

3.1. Introduction

The reduction of N_2 to NH_3 is critical for life and is performed on a massive scale both industrially and biologically.[1] The high stability of the N≡N triple bond necessitates catalysts and high-energy reagents/conditions to achieve the desired transformation.[2] Synthetic studies of catalytic N_2-to-NH_3 conversion by model complexes are of interest to constrain hypotheses concerning the mechanism/s of biological (or industrial) N_2-fixation and to map fundamental catalyst design principles for multi-electron reductive transformations.[3]

Interest in Fe model systems that catalyze N_2-to-NH_3 conversion has grown in part due to the postulate that one or more Fe centers in the FeMo-cofactor of FeMo-nitrogenase may serve as the site of N_2 binding and activation during key bond-breaking and -making steps.[4] Previous examples of synthetic molecular Fe catalysts that mediate N_2-to-NH_3 conversion operate with high driving force, relying on a very strong acid (pK_a ca. 0) and reductant ($E° < -3.0$ V vs $Fc^{+/0}$).[5] In contrast, several Mo catalysts have been shown to facilitate N_2-to-NH_3 conversion with significantly lower driving force.[6] There is thus interest in exploring

the viability of Fe-mediated catalytic N_2-to-NH_3 conversion under less forcing conditions from a practical perspective, and to continue assessing these systems as functional models of biological nitrogenases.

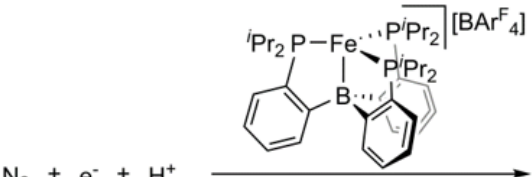

e^- (E^0 vs $Fc^{+/0}$)	H^+ (pK_a in THF)	$\Delta\Delta H_f$ (kcal/mol)
Cp^*_2Co (-1.96 V)	$[PhNH_3][OTf]$ (7.8)	62
Cp^*_2Co (-1.96 V)	$[Ph_2NH_2][OTf]$ (4.1)	77
KC_8 (≤ -3.0 V)	$HBAr^F_4$ (ca. 0)	≥ 156

Figure 3.1. Summary of conditions used for catalytic N_2-to-NH_3 conversion by $P_3{}^BFe^+$ highlighting the estimated enthalpic driving force ($\Delta\Delta H_f$).[7]

In this chapter, it is demonstrated that catalytic conversion of N_2 to NH_3 by $P_3{}^BFe^+$ ($P_3{}^B$ = tris(*o*-diisopropylphosphinophenyl)borane) can be achieved with a significantly lower driving force by coupling Cp^*_2Co with $[Ph_2NH_2]^+$ or $[PhNH_3]^+$ (Figure 3.1). Such conditions additionally afford unusually high selectivity and catalytic turnover for NH_3.[8] Moreover, it is noted that the use of milder reagents as reductant and acid engenders a higher effective bond dissociation enthalpy (BDFE; eq 3.1).[7a,9] This may in turn afford access to proton-coupled electron transfer (PCET) pathways (e.g., $FeN_2 + H\cdot \rightarrow FeN_2H$) distinct from electron transfer (ET)/proton transfer (PT) pathways, thus enhancing overall catalytic efficiency.

$$BDFE_{effective} = 1.37(pK_a) + 23.06(E^0) + C_G \quad (3.1)$$

Theoretical considerations, including DFT calculations, are discussed that suggest the viability of a decamethylcobaltocene-mediated PCET pathway in this system; by extension we suggest metallocene-mediated (e.g., Cp^*_2Cr) PCET pathways may be operative in previously studied Mo and Fe N_2-fixing systems that use metallocene reductants.[6,8]

3.2. Results

3.2.1 Catalysis Using $[P_3^BFe][BAr^F_4]$, Cp^*_2Co and $[R_nNH_{(4-n)}][OTf]$

Various observations of P_3^BFe complexes in the presence of acids and reductants suggested that this system might be capable of N_2-to-NH_3 conversion with lower driving force than that originally reported. Accordingly, we had observed that the treatment of $P_3^BFeN_2^-$ with KC_8 and weaker acids ($pK_a > 0$) led to greater than stoichiometric NH_3 formation (e.g., under unoptimized conditions [2,6-dimethylanilinium][OTf] afforded 2.1 equiv NH_3 per Fe).[10] Similarly, the treatment of $P_3^BFeN_2^-$ with $[H(OEt_2)_2][BAr^F_4]$ ($HBAr^F_4$, BAr^F_4 = tetrakis(3,5-bis(trifluoromethyl)phenyl)borate) and weaker reductants led to modest yields of NH_3. For example, under unoptimized conditions we had observed that decamethylcobaltocene (Cp^*_2Co) and $HBAr^F_4$ afforded 0.6 equiv NH_3 per Fe.[10,11] Most recently, an apparent catalytic response was observed during a cyclic voltammetry experiment at the $P_3^BFeN_2^{0/-}$ couple (−2.1 V vs $Fc^{+/0}$) upon addition of excess $HBAr^F_4$ under an N_2 atmosphere. Electrolytic NH_3 generation by $P_3^BFe^+$ was observed at −2.4 V vs $Fc^{+/0}$ in Et_2O,[11] and Na/Hg (−2.4 V vs $Fc^{+/0}$ in THF)[7b] could instead be used for N_2-to-NH_3 conversion catalysis (albeit less selectively and with low turnover). Finally, mixing $P_3^BFe^+$ with Cp^*_2Co in Et_2O at −78 °C under N_2 generates some $P_3^BFeN_2^-$ as observed by X-band

EPR and Mössbauer spectroscopy (See Appendix 2), suggesting that Cp^*_2Co is in principle a sufficiently strong reductant to trigger catalysis by $P_3^BFe^+$.

Treatment of $P_3^BFe^+$ with Cp^*_2Co and $[Ph_2NH_2][OTf]$, $[Ph_2NH_2][BAr^F_4]$, or $[PhNH_3][OTf]$ in Et_2O at −78 °C under an N_2 atmosphere affords catalytic yields of NH_3 (Table 3.1). Notably, the highest selectivity for NH_3 obtained among this series (72% at standard substrate loading; Entry 1) is significantly improved compared to all previously described (molecular) Fe catalysts for N_2-to-NH_3 conversion.[8,12] Tripling the initial substrate loading (Entry 2) nearly triples the NH_3 production with only modest loss in efficiency for NH_3 (63%). Preliminary attempts to further increase the initial substrate loading have led to substantially decreased efficiency (Entry 3). However, substrate reloading experiments (Entries 4 and 5) maintain greater than 50% efficiency for NH_3 overall; a turnover number for NH_3 generation via two reloadings has been achieved as high as 89 (84 ± 8; Entry 5). This is the highest turnover number yet reported for a (molecular) N_2-to-NH_3 conversion catalyst under any conditions.[13]

The use of the more soluble acid $[Ph_2NH_2][BAr^F_4]$ (Entry 6) provides significantly lower, but still catalytic, yields of NH_3. This more soluble acid presumably increases background reactivity with Cp^*_2Co (See Appendix 2). Perhaps more significantly, $[PhNH_3][OTf]$ is a considerably weaker acid than $[Ph_2NH_2][OTf]$ (Figure 3.1), but still provides substantial catalytic yields of NH_3 (Entries 7 and 8) and at efficiencies that compare well with those obtained previously using $HBAr^F_4$ and KC_8 despite a difference in driving force of nearly 100 kcal/mol.[11]

Table 3.1. N_2-to-NH_3 Conversion with P_3^EM Complexes (M = Fe, Co)

	Catalyst	Cp^*_2Co (equiv)	Acid (equiv)	Equiv. NH_3/Fe	% Yield (NH_3/e^-)
1	$P_3^BFe^+$	54	108[b]	12.8 ± 0.5	72 ± 3
2	$P_3^BFe^+$	162	322[b]	34 ± 1	63 ± 2
3	$P_3^BFe^+$	322	638[b]	26.7 ± 0.9	25 ± 1
4[a]	$P_3^BFe^+$	[162]x2	[322]x2[b]	56 ± 9	52 ± 9
5[a]	$P_3^BFe^+$	[162]x3	[322]x3[b]	84 ± 8	52 ± 5
6	$P_3^BFe^+$	54	108[c]	8 ± 1	42 ± 6
7	$P_3^BFe^+$	54	108[d]	7 ± 1	38 ± 7
8	$P_3^BFe^+$	162	322[d]	16 ± 3	29 ± 4
9	$P_3^{Si}FeN_2$	54	108[b]	1.2 ± 0.1	6 ± 1
10	$P_3^BCoN_2^-$	54	108[b]	1.1 ± 0.4	6 ± 2
11	$P_3^{Si}CoN_2$	54	108[b]	0 ± 0	0 ± 0

The catalyst, acid, Cp^*_2Co, and Et_2O were sealed in a vessel at −196 °C under an N_2 atmosphere followed by warming to −78 °C and stirring. Yields are reported as an average of at least 2 runs; for individual experiments See Appendix 2. [a]For these experiments the reaction was allowed to proceed for 3 hours at −78 °C before cooling to −196 °C and furnished with additional substrate and solvent [b][Ph_2NH_2][OTf]. [c][Ph_2NH_2][BAr^F_4]. [d][$PhNH_3$][OTf].

We also screened several related phosphine-ligated Fe–N_2 and Co–N_2 complexes[14] under the new standard reaction conditions with [Ph_2NH_2][OTf] and Cp^*_2Co (Entries 9–11) but

found that none of these other systems were competent catalysts. While we anticipate other catalyst systems for N_2-to-NH_3 conversion may yet be found that function under the conditions described herein,[8] certain features of the P_3^BFe system correlate with unusually productive catalysis.[14b]

Also significant is that when $P_3^BFe^+$ is loaded with 322 equiv $[Ph_2NH_2][OTf]$ and 162 equiv Cp^*_2Co in Et_2O at −78 °C, modest levels of N_2H_4 are detected (< 1 equiv per Fe; see Appendix 2). We had previously reported that catalytic N_2 reduction with KC_8 and $HBAr^F_4$ yielded no detectable hydrazine, but observed that if hydrazine was added at the outset of a catalytic run, it was consumed.[5a] When 5 equiv of N_2H_4 were added at the beginning of a catalytic run (again with 322 equiv $[Ph_2NH_2][OTf]$ and 162 equiv Cp^*_2Co), only 0.22 equiv of N_2H_4 (4.4% recovery) remained after workup. This result indicates that liberated hydrazine can also be reduced or disproportionated under the present conditions. That N_2H_4 is detected to any extent in the absence of initially added N_2H_4 under these conditions indicates that a late N–N cleavage mechanism to produce NH_3 (e.g., alternating or hybrid cross-over) is accessible.[3b,15] Whether such a pathway is kinetically dominant is as yet unclear.[11,16]

3.2.2. Fe Speciation under Turnover Conditions

The P_3^BFe speciation under turnover conditions was probed via freeze-quench Mössbauer spectroscopy.[11] The Mössbauer spectrum of a catalytic reaction mixture after five minutes of reaction time (Figure 3.2) reveals the presence of multiple species featuring well-resolved sets of quadrupole doublets. The spectrum is satisfactorily simulated with $P_3^BFeN_2$ (δ = 0.55 mm/sec, ΔE_Q = 3.24 mm/sec, 32%; Figure 3.2 green), $P_3^BFeN_2^-$ (δ =

0.40 mm/sec, ΔE_Q = 0.98 mm/sec, 26%; Figure 2 blue),[11,17] an unknown $P_3{}^BFe$ species (δ = 0.42 mm/sec, ΔE_Q = 1.84 mm/sec, 18%; Figure 3.2 yellow), and a final species that is modeled with δ = 0.96 mm/sec and ΔE_Q = 3.10 mm/sec (24%; Figure 3.2 orange). The broad nature of this last signal and its overlap with other features in the spectrum prevents its precise assignment, but its high isomer shift and large quadrupole splitting are suggestive of a tetrahedral, *S* = 2 Fe(II) complex.[18] The Mössbauer spectrum of a catalytic reaction mixture after 30 minutes was also analyzed (See Appendix 2). The spectrum still shows $P_3{}^BFeN_2$ (53%), the same unknown $P_3{}^BFe$ species (18%), and again a tetrahedral, high-spin Fe(II) component (22%). However, $P_3{}^BFe^+$ is now present (δ = 0.75 mm/sec, ΔE_Q = 2.55 mm/sec, 8%) and $P_3{}^BFeN_2^-$ is no longer observed. The reloading experiments described above provide strong evidence that "$P_3{}^BFe$" species represent an "active catalyst" population; interpretation of the relative speciation via spectroscopy should hence bear on the mechanism of the overall catalysis.

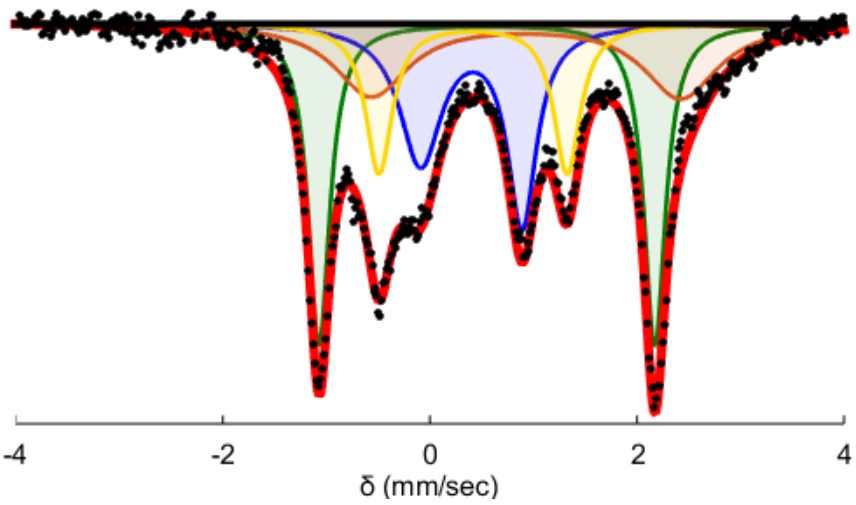

Figure 3.2. Mössbauer spectrum at 80 K with 50 mT applied parallel field of a freeze-quenched catalytic reaction (54 equiv Cp^*_2Co, 108 equiv $[Ph_2NH_2][OTf]$, 1 equiv $P_3^B[^{57}Fe]^+$) after five minutes of reaction time.

The appearance of a presumed high-spin ($S = 2$), tetrahedral Fe(II) species during catalysis (ca. 25%) might arise via dechelation of a phosphine arm. This species could represent an off-path state, or a downstream deactivation product. Interestingly, under the present catalytic conditions we do not observe the borohydrido-hydrido species $P_3^B(\mu\text{-H})Fe(H)(L)$ ($L = N_2$ or H_2); this species was postulated to be an off-path resting state during N_2-to-NH_3 conversion catalysis using $HBAr^F_4$ and KC_8 and was the major component observed at early times (ca. 60% at 5 min).[11] It therefore appears that a larger fraction of the "P_3^BFe" species are in a catalytically on-path state at early reaction times under these new catalytic conditions.

Additionally, the presence of a significant degree of $P_3^BFeN_2^-$ (Figure 2) at an early time point is distinct from conditions with $HBAr^F_4$ and KC_8.[11] This observation is consistent with the notion that protonation of $P_3^BFeN_2^-$ is slowed under the present conditions, likely as a result of the insolubility of the triflate salt $[Ph_2NH_2][OTf]$ and its attenuated acidity relative to $HBAr^F_4$.[7c-d,19] Clearly, differences in the rates of key elementary steps under the new conditions described here may lead to new mechanistic scenarios for N_2-to-NH_3 conversion.

3.2.3. DFT Predicted pK_a's and BDFEs

The improved catalytic efficiency at significantly lower driving force warrants additional consideration. When using $HBAr^F_4$ and KC_8 we have previously suggested that protonation

of $P_3^BFeN_2^-$, which itself can be generated by reduction of $P_3^BFeN_2$, to produce P_3^BFe-N=NH is a critical first step; P_3^BFe-N=NH can then be trapped by acid to produce spectroscopically observable $P_3^BFe{=}N\text{-}NH_2^+$.[16] These steps, shown in eq 3.2a-b, represent an ET-PT pathway. A PT-ET pathway, where $P_3^BFeN_2$ is sufficiently basic to be protonated to generate P_3^BFe-N=NH^+ as a first step, followed by ET, is also worth considering (eq 3.3a-b). A direct PCET pathway (eq 3.4) where H-atom delivery to $P_3^BFeN_2$ occurs, thus obviating the need to access either $P_3^BFeN_2^-$ or P_3^BFe-N=NH^+, needs also to be considered.

$P_3^BFeN_2 + e^- \rightarrow P_3^BFeN_2^-$ (3.2a)

$P_3^BFeN_2^- + H^+ \rightarrow P_3^B$Fe-N=NH (3.2b)

$P_3^BFeN_2 + H^+ \rightarrow P_3^B$Fe-N=$NH^+$ (3.3a)

P_3^BFe-N=$NH^+ + e^- \rightarrow P_3^B$Fe-N=NH (3.3b)

$P_3^BFeN_2 + H\cdot \rightarrow P_3^B$Fe-N=NH (3.4)

Initial PT to $P_3^BFeN_2$ to generate P_3^BFe-N=NH^+ (eq 3.3a) is unlikely under the present conditions due to the high predicted acidity of P_3^BFe-N=NH^+ (pK_a = −3.7; estimated via DFT; See Appendix 2); efficient generation of such a species seems implausible for acids whose pK_a's are calculated at 1.4 ($Ph_2NH_2^+$) and 6.8 ($PhNH_3^+$) in Et_2O (Table 3.2). We note that $[Ph_2NH_2][OTf]$ does not react productively with $P_3^BFeN_2$ at -78 °C in Et_2O, as analyzed by Mössbauer spectroscopy.

Focusing instead on the PCET pathway (eq 3.4), the DFT-calculated $BDE_{N\text{-}H}$ for P_3^BFe-N=NH (35 kcal/mol; Table 2; See Appendix 2 for details)[20] is larger than the effective BDE[9] of either $Cp^*_2Co/Ph_2NH_2^+$ or $Cp^*_2Co/PhNH_3^+$ (25 and 31 kcal/mol, respectively). This suggests that PCET (eq 3.4) is plausible on thermodynamic grounds. Given that we have employed Cp^*_2Co in this study, and that this and also Cp_2Co and Cp^*_2Cr have been

effective in other N_2-fixing molecular catalyst systems,[6,8] we have explored via DFT several putative metallocene-derived PCET reagents. Based on the analysis we describe below, we propose that protonated metallocenes may serve as discrete and highly active H· sources for PCET.

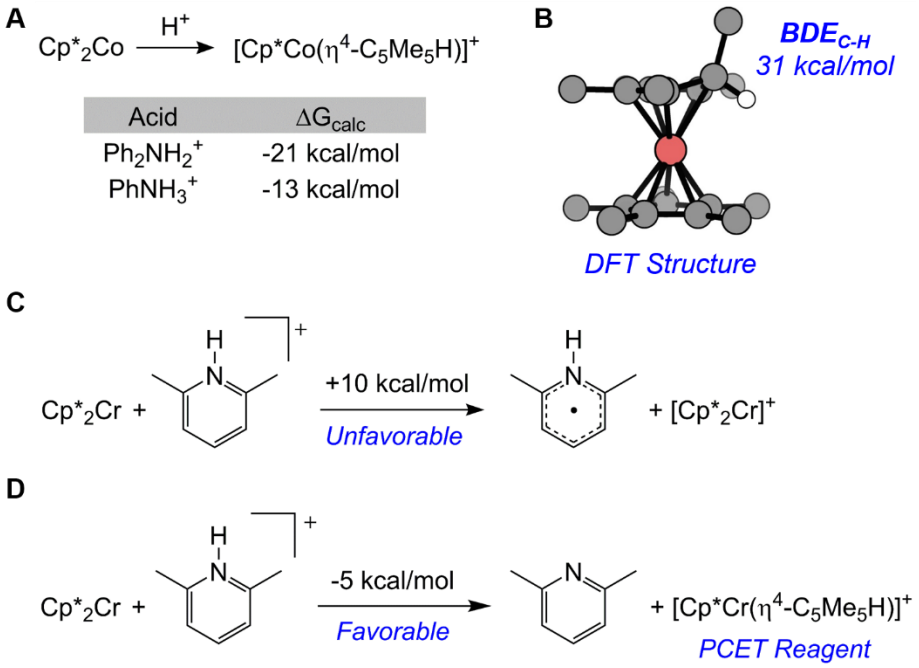

Figure 3.3. (A) Calculated free-energy changes for the protonation of Cp^*_2Co. (B) DFT optimized structure of *endo*-$Cp^*Co(\eta^4\text{-}C_5Me_5H)^+$ (methyl protons omitted for clarity). (C) The unfavorable reduction of 2,6-lutidinium by Cp^*_2Cr with the calculated free energy change. (D) The favorable protonation of Cp^*_2Cr by lutidinium with the calculated free energy change.

Accordingly, we find that the formation of *endo*- and *exo*-$Cp^*Co(\eta^4\text{-}C_5Me_5H)^+$ are predicted to be thermodynamically favorable via protonation of Cp^*_2Co by either $Ph_2NH_2^+$ or $PhNH_3^+$ (−21 and −13 kcal/mol, respectively; Figure 3.3A).[21] We have calculated the $BDE_{C\text{-}H}$'s for both *endo*- and *exo*-$Cp^*Co(\eta^4\text{-}C_5Me_5H)^+$ as 31 kcal/mol (Figure 3.3B; Table

2), indicating that they should be among the strongest PCET reagents accessible in this catalyst cocktail. Indeed, they would be among the strongest PCET reagents known.[9]

Table 3.2. Calculated pK_a Values and BDEs of Selected Species[a]

Species	pK_a	BDE[b]
$Ph_2NH_2^+$	1.4[c]	-
$PhNH_3^+$	6.8	-
Lutidinium	14.5	-
endo-Cp*Co(η^4-C_5Me_5H)$^+$	16.8	31
exo-Cp*Co(η^4-C_5Me_5H)$^+$	16.8	31
endo-Cp*Cr(η^4-C_5Me_5H)$^+$	17.3	37
exo-Cp*Cr(η^4-C_5Me_5H)$^+$	12.1	30
P_3^BFe-N=NH	38.7	35
P_3^BFe=N-NH_2^+	14.4	51
P_3^BFe=N-NH_2	-	47
[HIPTN_3N]Mo-N=NH	-	51

[a]Calculations were performed using the M06-L[22] functional with a def2-TZVP basis set on Fe and a def2-SVP basis set on all other atoms[23] (See Appendix 2). [b]In kcal/mol. [c]pK_a values were calculated in Et_2O and reported relative to $(Et_2O)_2H^+$.

We have also calculated the N–H bond strengths (Table 2) of several early stage candidate intermediates, including the aforementioned P_3^BFe-N=NH (35 kcal/mol), P_3^BFe=N-NH_2^+ (51 kcal/mol), and P_3^BFe=N-NH_2 (47 kcal/mol). We conclude that PCET from Cp*Co(η^4-C_5Me_5H)$^+$ to generate intermediates of these types is thermodynamically favorable in each case. To generate the first and most challenging intermediate (eq 3.5), the enthalpic driving force for PCET is estimated at ~4 kcal/mol (ΔG_{calc} = −9 kcal/mol). This driving force, and hence the plausibility of PCET steps, increases sharply as further downstream Fe-N_xH_y intermediates are considered.[24]

$$P_3^BFeN_2 + Cp^*Co(\eta^4\text{-}C_5Me_5H)^+ \rightarrow P_3^BFe\text{-}N{=}NH + Cp^*_2Co^+ \quad (3.5)$$

Independent studies of H_2 evolution from cobaltocene have invoked a protonated cobaltocene intermediate.[25,26] The observation of a background H_2 evolution reaction (HER) when employing metallocene reductants, but in the absence of an N_2-to-NH_3 conversion catalyst, suggests that metallocene protonation is kinetically competent.[6c,27]

3.3. Discussion

Given the prevalence of metallocene reductants in N_2-to-NH_3 (or -N_2H_4) conversion,[6,8] especially for the well-studied Mo catalyst systems, it is worth considering metallocene-mediated PCET more generally. For instance, a role for ET/PT steps (or conversely PT/ET) in N_2-to-NH_3 conversion catalyzed by [$HIPTN_3N$]Mo ($HIPTN_3N$ = [(3,5-(2,4,6-$^i Pr_3C_6H_2)_2C_6H_3NCH_2CH_2)_3N]^{3-}$, a bulky triamidoamine ligand) has been frequently posited.[27] But PCET steps may play a critical role, too. In the latter context, we note reports from Schrock and coworkers that have shown both acid and reductant are required to

observe productive reactivity with [HIPTN$_3$N]MoN$_2$. These observations are consistent with PCET to generate [HIPTN$_3$N]Mo-N=NH.[28e] A PCET scenario has been discussed in this general context of N_2-to-NH_3 conversion, where a lutidinyl radical intermediate formed via ET from Cp*$_2$Cr has been suggested as a PCET reagent that can be generated in situ.[27,29] However, our own calculations predict that the lutidinyl radical should not be accessible with Cp*$_2$Cr as the reductant (ΔG_{calc} = +10 kcal/mol; Figure 3C).[30] We instead propose protonation of Cp*$_2$Cr by the lutidinium acid as far more plausible (ΔG_{calc} = −5.3 kcal/mol; Figure 3D) to generate a highly reactive decamethylchromocene-derived PCET reagent.

While N–H bond strengths have not been experimentally determined for the [HIPTN$_3$N]Mo-system, using available published data we deduce the N–H bond of [HIPTN$_3$N]Mo-N=NH to be ca. 49 kcal/mol and we calculate it via DFT (truncated HIPTN$_3$N; See Appendix 2) as 51 kcal/mol.[31] The $BDE_{N\text{-}H}$ for this Mo diazenido species is hence much larger than we predict for P_3^BFe-N=NH (35 kcal/mol), perhaps accounting for its higher stability.[28e] A PCET reaction between *endo*-Cp*Cr(η^4-C_5Me_5H)$^+$ (BDE_{calc} = 37 kcal/mol) and [HIPTN$_3$N]MoN$_2$ to generate [HIPTN$_3$N]Mo-N=NH and Cp*$_2$Cr$^+$ would be highly exergonic. Furthermore, we predict a similarly weak $BDE_{C\text{-}H}$ for Cp-protonated cobaltocene, CpCo(η^4-C_5H_6)$^+$ (BDE_{calc} = 35 kcal/mol). These considerations are consistent with the reported rapid formation of [HIPTN$_3$N]Mo-N=NH using either Cp*$_2$Cr or Cp$_2$Co in the presence of lutidinium acid.[32]

3.4 Conclusions

To close, we have demonstrated catalytic N_2-to-NH_3 conversion by P_3^BFe$^+$ at a much lower driving force (nearly 100 kcal/mol) than originally reported via combination of a weaker

reductant (Cp^*_2Co) and acid ($[Ph_2NH_2][OTf]$ or $[Ph_3NH][OTf]$). Significantly improved efficiency for NH_3 formation is observed (up to 72% at standard substrate loading), and by reloading additional substrate at low temperature the highest turnover number yet observed for any synthetic molecular catalyst (84 ± 8 equiv NH_3 per Fe) has been achieved. Freeze-quench Mössbauer spectroscopy under turnover conditions reveals differences in the speciation of P_3^BFe compared to previous studies with $HBAr^F_4$ and KC_8, suggesting changes in the rates of key elementary steps. Using DFT calculations we have considered the viability of a decamethylcobaltocene-mediated PCET pathway as an alternative to previously formulated ET-PT and PT-ET pathways. Based on our calculations, we propose that protonated metallocenes should serve as discrete, very reactive PCET reagents in N_2-to-NH_3 conversion catalysis. Indeed, the achievement of high efficiency for N_2-to-NH_3 conversion by both P_3^BFe and various Mo catalysts that benefit from metallocene reductants raises the intriguing possibility that metallocene-based PCET reactivity is a potentially widespread and overlooked mechanism. Efforts are underway to further explore such pathways.

3.5. References

[1] Smil, V. *Enriching the Earth.* Cambridge: MIT Press, 2001.

[2] van der Ham, C. J.; Koper, M. T.; Hetterscheid, D. G. *Chem. Soc. Rev.* **2014**, *43*, 5183.

[3] (a) Shaver, M. P.; Fryzuk, M. *Adv. Synth. Catal.* **2003**, *345*, 1061. (b) Macleod, K. C.; Holland, P. L. *Nat. Chem.* **2013**, *5*, 559.

[4] Hoffman, B. M.; Lukoyanov, D.; Yang, D. Y.; Dean, D. R.; Seefeldt, L. C. *Chem. Rev.* **2014**, *114*, 4041.

[5] (a) Anderson, J. S.; Rittle, J.; Peters, J. C. *Nature* **2013**, *501*, 84. (b) Creutz, S.; Peters, J. C. *J. Am. Chem. Soc*. **2014**, *136*, 1105. (c) Ung, G.; Peters, J. C. *Angew. Chem. Int. Ed*.**2015**, *54*, 532. (d) Kuriyama, S.; Arashiba, K.; Nakajima, K.; Matsuo, Y.; Tanaka, H.; Ishii, K.; Yoshizawa, K.; Nishibayashi, Y. *Nat. Commun.* **2016**, *7*, 12181.

[6] (a) Yandulov, D. V.; Schrock, R. R. *Science* **2003**, *301*, 76. (b) Arashiba, K.; Miyake, Y.; Nishibayashi, Y. *Nat. Chem*. **2011**, *3*, 120. (c) Kuriyama, S.; Arashiba, K.; Nakajima, K.; Tanaka, H.; Kamaru, N.; Yoshizawa, K.; Nishibayashi, Y. *J. Am. Chem. Soc*. **2014**, *136*, 9719. (d) Arashiba, K.; Kinoshita, E.; Kuriyama, S.; Eizawa, A.; Nakajima, K.; Tanaka, H.; Yoshizawa, K.; Nishibayashi, Y. *J. Am. Chem. Soc*. **2015**, *137*, 5666.

[7] The enthalpic driving force ($\Delta\Delta H_f$) has been estimated here by taking $3*(BDE_{H\cdot} - BDE_{effective})$, where BDE is bond dissociation enthalpy. This allows for an evaluation of the driving force for a given reaction with respect to that for a hypothetical N_2-to-NH_3 conversion catalyst that uses H_2 as the proton and electron source. This is achieved by using Bordwell's equation (with the assumption that $S(X^{\cdot}) = S(XH)$; See Appendix 2) and literature values for p*K*a, redox potential, the enthalpy of reaction for $H^+ + e^- \rightarrow H^{\cdot}$ (C_H = 66 kcal/mol in THF), and the energy of $H^{\cdot}$ in THF (52 kcal/mol): (a) Bordwell, F. G.; Cheng, J.-P.; Harrelson, Jr., J. A. *J. Am. Chem. Soc.* **1988**, *110*, 1229. (b) Connelly, N. G.; Geiger, W. E. *Chem. Rev.* **1996**, *96*, 877. (c) Garido, G.; Rosés, M.; Ràfols, C.; Bosch, E. *J. Sol. Chem.* **2008**, *37*, 689. (d) Kaljurand, I.; Kütt, A.; Sooväli, L.; Rodima, T.; Mäemets, V.; Leito, I.; Koppel, I. A. *J. Org. Chem.* **2005**, *70*, 1019. (e) Cappellani, E. P.; Drouin, S. D.; Jia, G.; Maltby, P. A.; Morris, R. H.; Schweitzer, C. T. *J. Am. Chem. Soc.* **1994**, *116*, 3375.

[8] While initiating our studies we became aware of a phosphine-supported Fe system that catalyzes N_2-to-N_2H_4 conversion using Cp^*_2Co and $[Ph_2NH_2][OTf]$ with efficiency as high

as 72% for e^- delivery to N_2: Hill, P. J.; Doyle L. R.; Crawford A. D.; Myers W. K.; Ashley, A. E. *J. Am. Chem. Soc.* **2016**, *138*, 13521.

[8] Warren, J. J.; Tronic, T. A.; Mayer, J. M. *Chem. Rev.* **2010**, *110*, 6961.

[9] Anderson, J. S. *Catalytic conversion of nitrogen to ammonia by an iron model complex. Ph.D. Thesis, California Institute of Technology, September 2013.*

[10] Del Castillo, T. J.; Thompson, N. B.; Peters, J. C. *J. Am. Chem. Soc.* **2016**, *138*, 5341.

[11] Previously reported molecular Fe catalysts for N_2-to-NH_3 conversion utilize KC_8 and $HBAr^F_4$ and achieve NH_3 selectivities ≤ 45% with respect to their limiting reagent (see ref 5) at a similar reductant loading. Lower selectivities are observed with higher loading (see refs **Error! Bookmark not defined.**a and **Error! Bookmark not defined.**).

[12] In catalytic runs performed with labeled $[Ph_2{}^{15}NH_2][OTf]$ under an atmosphere of natural abundance $^{14}N_2$ the production of exclusively $^{14}NH_3$ is observed, demonstrating that the NH_3 formed during catalysis is derived from N_2 and not degradation of the acid (See Appendix 2).

[13] (a) Whited, M. T.; Mankad, N. P.; Lee, Y.; Oblad, P. F.; Peters, J. C. *Inorg. Chem.* **2009**, *48*, 2507. (b) Del Castillo, T. J.; Thompson, N. B.; Suess, D. L.; Ung, G.; Peters, J. C. *Inorg. Chem.* **2015**, *54*, 9256.

[14] Rittle, J.; Peters, J. C. *J. Am. Chem. Soc.* **2016**, *138*, 4243.

[15] Anderson, J. S.; Cutsail, 3rd, G. E.; Rittle, J.; Connor, B. A.; Gunderson, W. A.; Zhang, L.; Hoffman, B. M.; Peters, J. C. *J. Am. Chem. Soc.* **2015**, *137*, 7803.

[16] The presence of $P_3{}^BFeN_2^-$ was confirmed by freeze-quench EPR spectroscopy experiments (See Appendix 2). The asymmetry observed in the Mössbauer lineshapes is characteristic of this species. A redox equilibrium between $P_3{}^BFeN_2{}^{0/-}$ and $Cp^*_2Co^{+/0}$ is also

observed in the reaction of $P_3^BFe^+$ with excess Cp^*_2Co in the absence of acid (See Appendix 2).

[17] The distinct properties of tetrahedral, high spin Fe(II) leads to high isomer shifts (0.9-1.3) and large quadrupole splittings (> 2.5) that are characteristic of these types of species: (a) E. Münck, in *Physical Methods in Bioinorganic Chemistry: Spectroscopy and Magnetism* (Ed.: L. Que Jr.), University Science Books, Sausalito, CA, **2000**, pp. 287-320. (b) Daifuku, S. L.; Kneebone, J. L.; Snyder, B. E.; Neidig, M. L. *J. Am. Chem. Soc.* **2015**, *137*, 11432.

[18] Hamashima, Y.; Somei, H.; Shimura, Y.; Tamura, T.; Sodeoka, M. *Org. Lett.* **2004**, *6*, 1861.

[19] Experimental $BDE_{N\text{-}H}$'s for related species ($P_3^{Si}Fe\text{-}C{=}NH^+$, $P_3^{Si}Fe\text{-}C{=}NH$, $P_3^{Si}Fe\text{-}C{=}N(Me)H^+$, $P_3^{Si}Fe\text{-}C{=}N(Me)H$, and $P_3^{Si}Fe\text{-}N{=}N(Me)H^+$) have been measured and are in good agreement with the $BDE_{N\text{-}H}$ values calculated using the DFT methods described in this work (See Appendix 2 for full details): Rittle, J.; Peters, J. C. manuscript submitted for publication.

[20] Note: Efforts to instead optimize a $[Cp^*_2Co\text{-}H]^+$ species led to hydride transfer to the ring system.

[21] Zhao Y.; Truhlar D. G. *J. Chem. Phys.* **2006**, *125*, 194101.

[22] Weigend F.; Ahlrichs R. *Phys. Chem. Chem. Phys.* **2005**, *7*, 3297.

[23] Studies have shown that the Marcus cross-relation holds quite well for many PCET reactions. This is indicative of a substantial correlation between thermodynamic driving force and reaction kinetics; it is, however, unclear whether the proposed reactivity would demonstrate such behavior: (a) Roth, J. P.; Yoder, J. C.; Won, T.–J.; Mayer, J. M. *Science*,

2001, *294*, 2524. (b) Mayer, J. M.; Rhile, I. J. *Biochim. Biophys. Acta, Bioenerg.* **2004**, *1655*, 51. (c) Hammes-Schiffer, S. *Acc. Chem. Res.* **2001**, *34*, 273.

[24] Koelle, U.; Infelta, P. P.; Grätzel, M. *Inorg. Chem.* **1988**, *27*, 879.

[25] For recent studies relevant to protonated metallocenes in the context of HER see: (a) Pitman, C. L.; Finster, O. N. L.; Miller, A. J. M. *Chem. Commun.* **2016**, *52*, 9105. (b) Aguirre Quintana, L. M.; Johnson, S. I.; Corona, S. L.; Villatoro, W.; Goddard, 3rd, W. A.; Takase, M. K.; VanderVelde, D. G.; Winkler, J. R.; Gray, H. B.; Blakemore, J. D. *Proc. Natl. Acad. Sci. U.S.A.* **2016**, *113*, 6409.

[26] Munisamy, T.; Schrock, R. R. *Dalton Trans.* **2012**, *41*, 130.

[27] (a) Studt, F.; Tuczek, F. *Angew. Chem. Int. Ed.* **2005**, *44*, 5639. (b) Reiher, M.; Le Guennic, B.; Kirchner, B. *Inorg. Chem.* **2005**, *44*, 9640. (c) Studt, F.; Tuczek, F. *J. Comput. Chem.* **2006**, *27*, 1278. (d) Thimm, W.; Gradert, C.; Broda, H.; Wennmohs, F.; Neese, F.; Tuczek, F. *Inorg. Chem.* **2015**, *54*, 9248. (e) Yandulov, D. V.; Schrock, R. R. *Inorg. Chem.* **2005**, *44*, 1103.

[28] Pappas, I.; Chirik, P. J. *J. Am. Chem. Soc.* **2016**, *138*, 13379.

[29] Although our calculations for a hypothetical lutidinyl radical predict a weak N–H bond ($BDE_{N\text{-}H}$ ~ 35 kcal/mol), the oxidation potential of this species is calculated to be −1.89 V vs $Fc^{+/0}$ in THF (See Appendix 2). Experimental determination of this reduction potential for calibration has been contentious; however, our calculated reduction potential is similar to that previously calculated for pyridinium in aqueous media (−1.37 V vs SCE): (a) Yan, Y.; Zeitler, E. L.; Gu, J.; Hu, Y.; Bocarsley, A. B. *J. Am. Chem. Soc.* **2013**, *135*, 14020. (b) Keith, J. A.; Carter, E. A. *J. Am. Chem. Soc.* **2012**, *134*, 7580.

[30] It has been reported that $[HIPTN_3N]MoN_2^-$/[HIPTN$_3$N]Mo-N=NH is in equilibrium with DBU/$DBUH^+$ (DBU = 1,8-diazabicyclo[5.4.0]undec-7-ene; pK_a = 18.5 in THF; see refs 7c-d). Taken with the reported reduction potential of [HIPTN$_3$N]MoN_2 ($E_{1/2}$ = −1.81 V vs $Fc^{+/0}$ in THF, see ref 28e), the experimental BDE can be approximated with the Bordwell equation and the enthalpy of reaction for $H^+ + e^- \rightarrow H^\cdot$ (see ref 7).

[31] In addition to lutidinium salts, [Et_3NH][OTf] has been shown to affect the formation of [HIPTN$_3$N]Mo-N=NH from [HIPTN$_3$N]MoN_2 in the presence of metallocene reductants (see ref 28e).

Chapter 4. Fe-Mediated Nitrogen Fixation with a Metallocene Mediator: Exploring pKa Effects and Demonstrating Electrocatalysis

4.1 Introduction

There has been substantial recent progress in the development of soluble, well-defined molecular catalysts for N_2-to-NH_3 conversion, commonly referred to as the nitrogen reduction reaction (N_2RR).[1] Nevertheless, a significant and unmet challenge is to develop molecular catalysts, and conditions, compatible with electrocatalytic N_2RR. Progress in this area could have both fundamental and practical benefits, including access to informative in situ mechanistic studies via electrochemical techniques, and an electrochemical means to translate solar or otherwise derived chemical currency (H^+/e^-) into NH_3. The latter goal, which has been the subject of numerous studies using heterogeneous catalysts, is key to the long-term delivery of new ammonia synthesis technologies for fertilizer and/or fuel.[2]

Many soluble coordination complexes are now known that electrocatalytically mediate the hydrogen evolution reaction (HER),[3] the carbon dioxide reduction reaction (CO_2RR),[4] and the oxygen reduction reaction (ORR).[5] The study of such systems has matured at a rapid pace in recent years, coinciding with expanded research efforts towards solar-derived fuel systems. In this context, it is noteworthy how little corresponding progress has been made towards the discovery of soluble molecular catalysts that mediate electrocatalytic N_2RR. To our knowledge, only two prior systems address this topic directly.[6-8]

Pickett and coworkers reported, more than three decades ago, that a Chatt-type tungsten-hydrazido complex ($W{=}NNH_2$) could be electrochemically reduced to release ammonia (and trace hydrazine), along with some amount of a reduced $W–N_2$ product; the latter species serves as the source of the $W{=}NNH_2$ species (via its protonation by acid).[6a]

By cycling through such a process, an electrochemical, but not an electrocatalytic, synthesis of ammonia was demonstrated. Indeed, efforts to demonstrate electrocatalysis with this and related system instead led to substoichiometric NH_3 yields.[6c]

An obvious limitation to progress in electrochemical N_2RR by molecular systems concerns the small number of synthetic N_2RR catalysts that have been available for study; it is only in the past five years that sufficiently robust catalyst systems have been identified to motivate such studies. In addition, the conditions that have to date been employed to mediate N_2RR have typically included non-polar solvents, such as heptane, toluene, and diethyl ether (Et_2O), that are not particularly well-suited to electrochemical studies owing to their low conductivity.[1]

Nevertheless, several recent developments, including by our lab, point to the likelihood that iron (and perhaps other) molecular coordination complexes may be able to mediate electrocatalytic N_2RR in organic solvent. Specifically, our lab recently reported that a tris(phosphine)borane iron complex, $P_3{}^BFe^+$, that is competent for catalytic N_2RR, can also mediate electrolytic N_2-to-NH_3 conversion,[6d] with the available data (including this study) pointing to bona fide electrocatalysis in Et_2O.

Focusing on the $P_3{}^BFe^+$ system we have studied, a development relevant to the current study was its recently demonstrated compatibility with reagents milder than those originally employed.[1c] Thus decamethylcobaltocene (Cp^*_2Co) and diphenyl ammonium acid ($Ph_2NH_2^+$) are effective; these reagents give rise to fast, and also quite selective (>70% vs HER) N_2RR catalysis at low temperature and pressure in ethereal solvent. In addition, based on preliminary spectroscopic evidence and density functional theory (DFT) predictions, it appears that a protonated metallocene species, $Cp^*(\eta^4\text{-}C_5Me_5H)Co^+$, may be

an important intermediate of N_2RR catalysis under such conditions. Indeed, we have suggested that Cp*(η^4-C_5Me_5H)Co^+ may be an effective proton-coupled-electron-transfer (PCET) donor ($BDE_{C–H}$(calc) = 31 kcal/mol), thereby mediating net H-atom transfers to generate N−H bonds during N_2RR. The presence of a metallocene mediator might, therefore, enhance N_2RR during electrocatalysis.[9]

We present here a study of the effect of pK_a on the selectivity of $P_3^BFe^+$ for N_2RR vs HER. By using substituted anilinium acids, we are able to vary the acidity over 9 orders of magnitude and find that the selectivity is highly correlated with the pK_a. In our efforts to investigate the origin of the observed pK_a effect, we found to our surprise that the catalytically relevant acids were unable to faciltate productive early-stage N–H bond formation in stoichiometric reactions and therefore hypothesized that the formation of a protonated metallocene species Cp*(η^4-C_5Me_5H)Co^+ indeed played a critical role in N–H bond-forming reactions either via PCET or PT during N_2RR catalysis. DFT studies support this hypothesis and also establish that the observed pK_a effect can be explained by the varying ability of the acids to protonate Cp^*_2Co. The critical role of this protonated metallocene intermediate in N–H bond forming reactions led us to test the effect of $Cp^*_2Co^+$ as an additive in the electrolytic synthesis of NH_3 by $P_3^BFe^+$. We found that the addition of co-catalytic $Cp^*_2Co^+$ enhances both yield of NH_3 and Faradaic efficiency (FE), and thus furnishes the first unequivocal demonstration of electrocatalytic N_2RR with a soluble, molecular coordination complex.

4.2. Results and Discussion

4.2.1 pK_a studies.

In our recent study on the ability of $P_3^BFe^+$ to perform N_2RR with Cp^*_2Co as the chemical reductant, we found that there was a marked difference in efficiency for NH_3 demonstrated by diphenylammonium triflate ($[Ph_2NH_2][OTf]$) and anilinium triflate ($[PhNH_3][OTf]$).**Error! Bookmark not defined.** In that study we posited that this difference could a rise from a variety of sources including the differential solubility, sterics, or pK_a's of these acids. To better investigate this last possibility we explored the efficiency of the catalysis by quantifying the NH_3 and H_2 produced when using substituted anilinium acids with different pK_a values (**Table 4.1**). The table is organized in descending acid strength, from [$^{4\text{-OMe}}$PhNH$_3$][OTf] as the weakest acid to the perchlorinated derivative ([$^{\text{per-Cl}}$PhNH$_3$][OTf]) as the strongest. Importantly, good total electron yields (85.8 ± 3.3) were obtained in all cases. As can be seen from the table, the NH_3 efficiencies are found to be strongly correlated with pK_a.[10]

In particular, a comparison of the efficiency for NH_3 with the pK_a of the anilinium acid used gives rise to four distinct activity regimes (**Table 4.1**). Firstly, a regime that is completely inactive for N_2RR, but active for HER, is defined by the weakest acid [$^{4\text{-OMe}}$PhNH$_3$][OTf] (pK_a = 8.9).[11] A gradual increase in observed NH_3 yields, coupled with a decreased H_2 yield, comprises a second regime in which the acid is strengthened from $[PhNH_3][OTf]$ (pK_a = 7.8), to [$^{2,6\text{-Me}}$PhNH$_3$][OTf] (pK_a = 6.8), to [$^{2\text{-Cl}}$PhNH$_3$][OTf] (pK_a = 5.6). Yet stronger acids, [$^{2,5\text{-Cl}}$PhNH$_3$][OTf] (pK_a = 4.1), [$^{2,6\text{-Cl}}$PhNH$_3$][OTf] (pK_a = 3.4), and [$^{2,4,6\text{-Cl}}$PhNH$_3$][OTf] (pK_a = 2.1), provide the third, most active N_2RR regime in which the H_2 yields are nearly invariant.[12] The highest selectivity for N_2RR (~78%) was observed

using [$^{2,5\text{-Cl}}$PhNH$_3$][OTf] as the acid. A fourth regime of very low N_2RR activity is encountered with [$^{\text{per-Cl}}$PhNH$_3$][OTf] (pK_a = 1.3) as the acid. We suspect this last acid undergoes unproductive reduction via ET, thereby short-circuiting N_2RR. Intriguingly the observed behavior is remarkably similar to that for nitrogenase which is the only other N_2RR system for which such pK_a effects have been well-studied (**Figure 4.4.1**).[13,14]

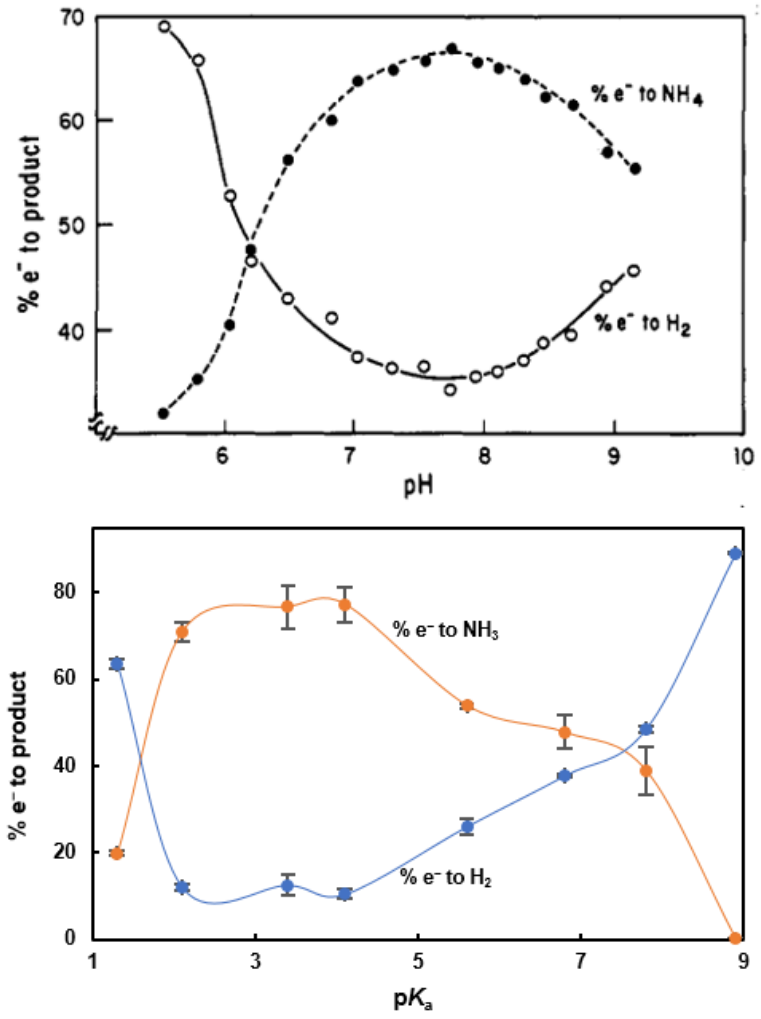

Figure 4.1. (top) Percentage of electrons being used to form NH_3 and H_2 at different pH values by the FeMo-nitrogenase in *A. vinelandii*. Reprinted with permission from Pham, D. N.; Burgess, B. K. *Biochemistry* **1993**, *32*, 13725. Copyright 1993 American Chemical

Society. (bottom) Percentage of electrons being used to form NH_3 and H_2 at different pK_a values by $P_3^BFe^+$.

In our previous study on Cp^*_2Co mediated N_2RR with $P_3^BFe^+$, we had identified that $P_3^BFeN_2^-$ forms under catalytic conditions. Earlier studies on the reactivity of $P_3^BFeN_2^-$ with excess of soluble acids such as HOTf or $[H(OEt_2)_2][BAr^F_4]$ ($HBAr^F_4$, BAr^F_4 = tetrakis(3,5-bis(trifluoromethyl)phenyl)borate)) at low temperature in Et_2O had determined that $P_3^BFe{=}NNH_2^+$ was rapidly formed.[15] Furthermore, recent computational work from our group posits that under catalytic conditions with a soluble acid the disparate efficiency for N_2RR demonstrated by P_3^EFe catalysts (E = B, C, Si) is determined by the rate of formation and consumption of early N_2RR intermediates (*i.e.* $P_3^EFe{=}NNH$ and $P_3^EFe{=}NNH_2^{+/0}$).[16] Thus we were interested in the reactivity of these anilinium triflate acids with $P_3^BFeN_2^-$ and hypothesized that they may show differential efficiency in the formation of $P_3^BFe{=}NNH_2^+$.

Table 4.1. Literature[10] and calculated[a,b] pK_a values and efficiencies observed in catalytic N_2-to-NH_3 conversion

	pK_a^{exp}	pK_a^{calc}	pK_d^{calc}	NH_3/Fe	%NH_3/e^-	%H_2/e^{-c}
$[^{4\text{-OMe}}PhNH_3][OTf]$	8.9	9.6	15.7	0.04 ± .01	0.2 ± 0.1	89.1 ± 0.2
$[PhNH_3][OTf]$	7.8	7.7	13.8	7.3 ± 0.1	40.4 ± 0.5	48.6 ± 0.7
$[^{2,6\text{-Me}}PhNH_3][OTf]$	6.8	7.3	13.2	8.6 ± 0.7	47.5 ± 4.0	37.8 ± 0.2
[Cp*(*exo*-η^4-C_5Me_5H)Co][OTf]	N/A	9.2	11.8	—	—	—
$[^{2\text{-Cl}}PhNH_3][OTf]$	5.6	5.6	6.0	10.7 ± 0.1	53.9 ± 0.4	26.1 ± 1.9

[$^{2,5\text{-Cl}}$PhNH$_3$][OTf]	4.1	4.0	5.0	13.9 ± 0.7	77.5 ± 3.8	10.5 ± 1.1
[$^{2,6\text{-Cl}}$PhNH$_3$][OTf]	3.4	3.4	3.4	13.8 ± 0 .9	76.7 ± 4.9	12.6 ± 2.5
[$^{2,4,6\text{-Cl}}$PhNH$_3$][OTf]	2.1	2.7	1.8	12.8 ± 0.4	70.9 ± 2.2	12.0 ± 0.8
[$^{\text{per-Cl}}$PhNH$_3$][OTf]	1.3	0.8	0.4	3.6 ± 0.1	19.9 ± 0.5	63.5 ± 1.1

[$^{4\text{-OMe}}$PhNH$_3$][OTf] = 4-methoxyanilinium triflate, [PhNH$_3$][OTf] = anilinium triflate, [$^{2,6\text{-Me}}$PhNH$_3$][OTf] = 2,6-dimethylanilinium triflate, [$^{2\text{-Cl}}$PhNH$_3$][OTf] = 2-chloroanilinium triflate, [$^{2,5\text{-Cl}}$PhNH$_3$][OTf] = 2,5-dichloroanilinium triflate, [$^{2,6\text{-Cl}}$PhNH$_3$][OTf] = 2,6-dichloroanilinium triflate, [$^{2,4,6\text{-Cl}}$PhNH$_3$][OTf] = 2,4,6-trichloroanilinium triflate, [$^{\text{per-Cl}}$PhNH$_3$][OTf] = 2,3,4,5,6-pentachloroanilinium triflate. [a]Acidities calculated at 298 K in THF and referenced to the known literature value for [$^{2,6\text{-Cl}}$PhNH$_3$][OTf]. [b]All species calculated as the ion-paired OTf$^-$ species in Et$_2$O at 195 K and referenced to the known literature value for [$^{2,6\text{-Cl}}$PhNH$_3$][OTf] in THF.

To our surprise the freeze-quench EPR spectrum of the reaction of excess [$^{2,6\text{-Cl}}$PhNH$_3$][OTf] (high efficiency regime) at −78 °C in Et$_2$O with $P_3^BFeN_2^-$ did not reveal any $P_3^BFe{=}NNH_2^+$. In accord with this result, freeze-quench Mössbauer experiments show only the formation of oxidized Fe products, namely $P_3^BFeN_2$ and $P_3^BFe^+$. Finally, analysis of such reactions for NH$_3$ or N$_2$H$_4$ after warming led to the observation of no fixed-N products. The observation of exclusively oxidation rather than productive N−H bond formation is reminiscent of experiments in which only 1 equiv of a soluble acid source (HBAr$^F_4$ or HOTf) is added to $P_3^BFeN_2^-$. In these cases, we have proposed that the unstable $P_3^BFe{=}NNH$ is formed and without excess acid to trap it as $P_3^BFe{=}NNH_2^+$ it decays with the loss of 1/2 an equivalent of H$_2$ to form $P_3^BFeN_2$.

Although large excesses of the triflate acids (25 eq) were employed in these experiments to mimic catalytic conditons, the low solubility of these anilinium triflate acids under the catalytically relevant conditions (Et_2O, -78 °C) likely leads to a situation in which the formed $P_3^BFe{=}NNH$ is not sufficienctly rapidly captured by acid and hence decays with loss of H_2. Further evidence in support of this hypothesis comes from experiments employing $[^{2,6\text{-Cl}}PhNH_3][BAr^F{}_4]$ as a soluble source of acid. In this case, freeze-quench EPR of the reaction between $P_3^BFeN_2^-$ and 25 eq of acid leads to the observation of $P_3^BFe{=}NNH_2^+$ and the quantification of fixed-N products upon warming (0.20 ± 0.04 eq. NH_3 per Fe).

While internally consistent, these observations must be reconciled with the seemingly contradictory observation of highly efficient N_2RR when $[^{2,6\text{-Cl}}PhNH_3][OTf]$ and other anilinium triflate acids are employed under catalytic conditions. In fact, we have previously observed that $[Ph_2NH_2][OTf]$ leads to superior efficiencies for NH_3 than observed with $[Ph_2NH_2][BAr^F{}_4]$ (72 ± 3% and 42 ± 6% respectively). An obvious difference between the stoichiometric reactions described above and the catalytic reaction is the presence of $Cp^*{}_2Co$ in the latter. We had previously postulated that $Cp^*{}_2Co$ could be protonated under the catalytic reaction conditions to form $Cp^*(\eta^4\text{-}C_5Me_5H)Co^+$. This species could then play a role in N−H bond forming reactions. The results herein suggest that such a mechanism is not only plausible but likely necessary to explain the observed catalytic results with anilinium triflate acids. Given the effect of pK_a on the efficiency for N_2RR, we hypothesized that this effect might arise from the thermodynamics or kinetics of $Cp^*{}_2Co$ protonation by the different anilinium acids.

4.2.2. Computational Studies

To investigate the kinetics and thermodynamics of Cp^*_2Co protonation by anilinium triflate acids we employed DFT. DFT-D_3[17]calculations were performed at the TPSS/def2-TZVP(Fe); def2-SVP[18] level of theory that our group has previously successfully employed in studies of this system.[19] We calculated the free energy of H^+ exchange (ΔG_a) for all of the used acids (one example in **eq 4.1**) and $Cp^*(exo\text{-}\eta^4\text{-}C_5Me_5H)Co^+$ in Et_2O at 298 K. These free energies were then used to determine the pK_a by including a term to adjust them to the literature pK_a value for [$^{2,6\text{-Cl}}PhNH_3$] [OTf] at 298 K in THF (**eq 4.2**).

$$PhNH_2 + {}^{2,6\text{-Cl}}PhNH_3^+ \rightarrow PhNH_3^+ + {}^{2,6\text{-Cl}}PhNH_2 \quad \text{(eq 4.1)}$$

$$pK_a(PhNH_3^+) = -\Delta G_a/(2.303\times RT) + pK_a({}^{2,6\text{-Cl}}PhNH_3^+) \quad \text{(eq 4.2)}$$

However, because we believe that the variable triflate hydrogen bonding effects (0.5–10 kcal/mol) are likely important under the catalytic conditions (low temperature and low polarity solvent), we additionally calculated the free energy for net HOTf exchange reactions (ΔG_d) at 195 K in Et_2O (one example in **eq 4.3**). The free energy of these reactions can then be used to determine a pK_d, which were also referenced to the pK_a value for [$^{2,6\text{-Cl}}PhNH_3$][OTf] at 298 K in THF for ease of comparison (**eq 4.4**). Going forward we will use the pK_d values in our discussion, but using the pK_a values would not substantively alter the conclusions.

$$PhNH_2 + [{}^{2,6\text{-Cl}}PhNH_3][OTf] \rightarrow [PhNH_3][OTf] + {}^{2,6\text{-Cl}}PhNH_2 \text{ (eq 4.3)}$$

$$pK_d([PhNH_3][OTf]) = -\Delta G_d/(2.303\times RT) + pK_a({}^{2,6\text{-Cl}}PhNH_3^+) \quad \text{(eq 4.4)}$$

Calculations of the pK_d of all of the relevant species (**Table 4.1**) leads to the observation that the pK_d of [Cp*(η^4-C_5Me_5H)Co][OTf] (pK_d^{calc} = 11.8; **Table 4.1**), falls within the range of acids studied ($0.4 \leq pK_d^{calc} \leq 15.7$; **Table 4.1**) suggesting there would be a significant acid dependence on the kinetics and thermodynamics of Cp*$_2$Co protonation. To better elucidate the differences in Cp*$_2$Co protonation between the acids, we investigated in detail the kinetics for three acids, [$^{2,6\text{-Cl}}$PhNH$_3$][OTf] (high selectivity; pK_d^{calc} = 3.4), [$^{2,6\text{-Me}}$PhNH$_3$][OTf] (modest selectivity; pK_d^{calc} = 13.2), and [$^{4\text{-OMe}}$PhNH$_3$][OTf] (poor selectivity; pK_d^{calc} = 15.8). Transition states were readily located for all three acids and as can be seen in **Figure 4.2**, protonation of Cp*$_2$Co is found to have only a moderate barrier in all three cases ([$^{4\text{-OMe}}$PhNH$_3$][OTf], [$^{2,6\text{-Me}}$PhNH$_3$][OTf] and [$^{2,6\text{-Cl}}$PhNH$_3$][OTf]: $\Delta G^{\ddagger}$ = +4.5 kcal/mol, +3.8 kcal/mol and +1.3 kcal/mol, respectively). This suggests that Cp*$_2$Co protonation is kinetically accessible in all cases, in agreement with the experimental observation of background HER with all of these acids (see SI).

The small differences in rate, and the large variance in the equilibrium constant defined in eq 4.5 (K_{eq}, **Figure 4.2**) illustrates the significant difference in the population of protonated metallocene for these different acids.

$$K_{eq} = \frac{[{}^{R}PhNH_2 - Cp^*(\eta^4 - C_5Me_5H)Co - OTf]}{[OTf - H_3N\,{}^{R}Ph - Cp^*_2Co]} \quad \text{(eq 4.5)}$$

The low solubility of the anilinium triflate acids and the low catalyst concentration leads to a situation in which the interaction between the acid and the Cp*$_2$Co significantly affects the kinetics of productive N−H bond formation. As such, the difference in [Cp*(η^4-C_5Me_5H)Co][OTf] population and formation rate is the origin of the observed pK_a effect, rather than differences in rates involving the direct interaction of a $P_3{}^{B}Fe$ species with acid.

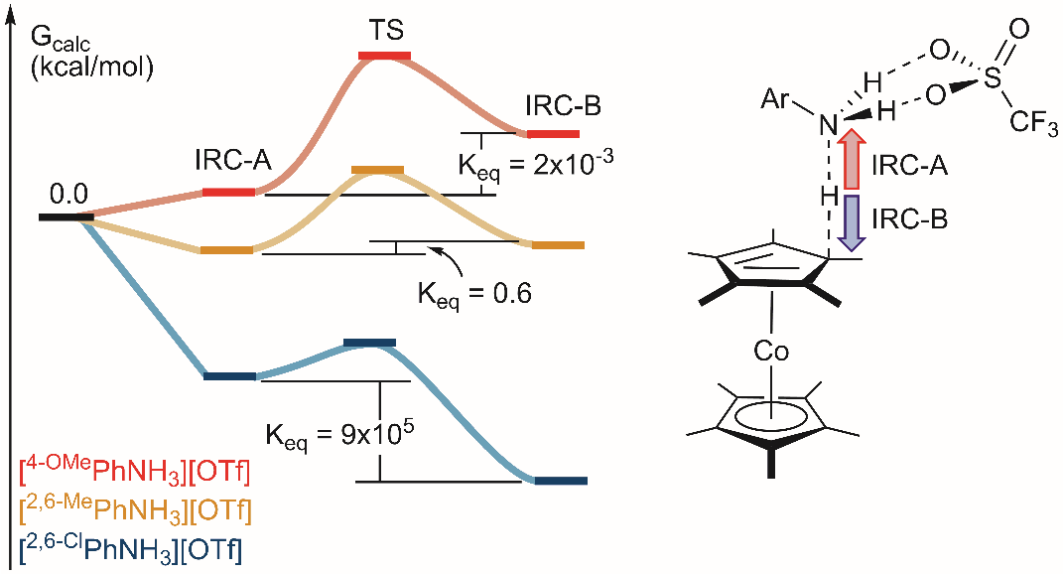

Figure 4.2. The kinetics and thermodynamics of protonation of Cp^*_2Co for three acids from different catalytic efficiency regimes.

As we discussed in our previous study, $[Cp^*(\eta^4\text{-}C_5Me_5H)Co][OTf]$ is a strong PCET donor.[20] This reaction can occur either in a synchronous fashion akin to HAT or in an asynchronous fashion that approaches a PT-ET reaction.[21] We believe that this reagent is likely effective in a variety of N−H bond forming reactions under the catalytic conditions. However, the experimental results suggest that this reagent likely plays a critical role in trapping the unstable $P_3^BFe{=}NNH$ (**Figure 4.3**) before it can decompose. Indeed, both a synchronous PCET reaction ($\Delta G_{PCET} = -17.3$ kcal/mol; **eq 4.6**), and the two individual steps of an asynchronous PCET reaction ($\Delta G_{PT} = -5.7$ kcal/mol, $\Delta G_{ET} = -11.6$ kcal/mol; **eq 4.7-4.8**) are found to be thermodynamically favorable.

$P_3^BFe{=}NNH + [Cp^*(\eta^4\text{-}C_5Me_5H)Co][OTf] \rightarrow P_3^BFe{=}NNH_2 + [Cp^*_2Co][OTf]$ (eq 4.6)

$P_3^BFe{=}NNH + [Cp^*(\eta^4\text{-}C_5Me_5H)Co][OTf] \rightarrow P_3^BFe{=}NNH_2^+ + Cp^*_2Co$ (eq 4.7)

$P_3^BFe{=}NNH_2^+ + Cp^*_2Co \rightarrow P_3^BFe{=}NNH_2 + [Cp^*_2Co][OTf]$ (eq 4.8)

To evaluate the kinetics of these reactions the Marcus theory expressions[22] and the Hammes-Schiffer method[23] were used to approximate relative rates of bimolecular ET and PCET. We find that there is a slight kinetic preference for the fully synchronous PCET reaction ($k_{rel}^{PCET} \sim 2x10^3 – 4.5x10^3$ kcal/mol) compared to the fully asynchronous PT-ET reaction ($k_{rel}^{ET} \equiv 1\ M^{-1}s^{-1}$; **Figure 4.3**) but both reaction mechanisms appear viable.[24]

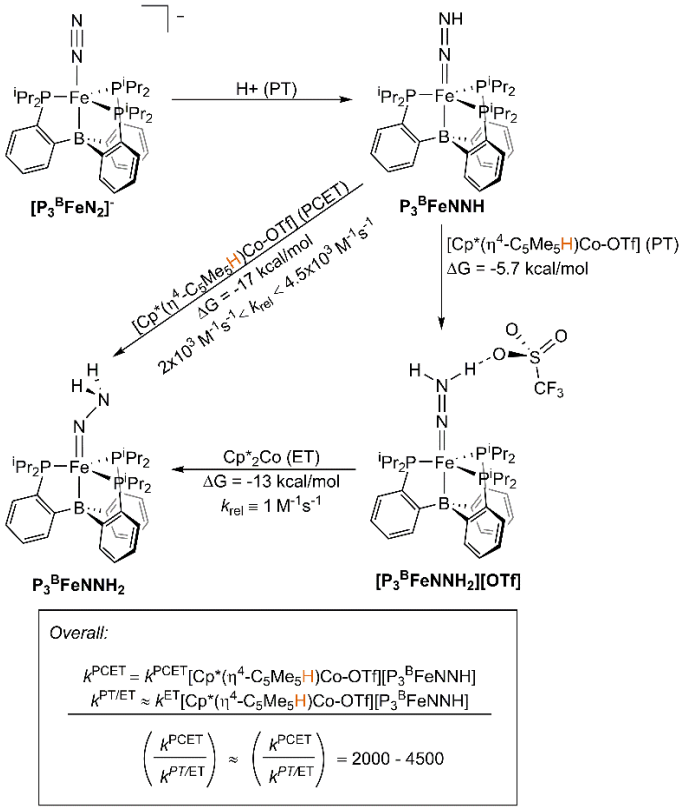

Figure 4.3. The calculated thermodynamics and kinetics of the proposed synchronous PCET and asynchronous PCET (PT–ET) reaction between P_3^BFeNNH and [Cp*(η^4-C_5Me_5H)Co][OTf].

This leads to the conclusion that the efficiency for NH_3 formation in this system is coupled to the kinetics and/or thermodynamics of the reaction between the acid and reductant. As the protonation of the reductant is also the first step on the background HER reaction[25] this conclusion is somewhat counterintuitive. The fact that an HER intermediate

can be intercepted and used for productive N_2RR steps is a potentially important design principle in the catalysis. Furthermore, this expanded role for metallocenes opens up an exciting new avenue of research into these reagents and the potentially multifaceted role that they play in the proton-coupled reduction of a variety of small molecule substrates. In N_2RR systems, efforts are often made to suppress the 'background' reaction between the acid and reductant.[1a-b] We were thus particularly curious whether the inclusion of a metallocene co-catalyst could improve the yield and Faradaic efficiency (FE) for NH_3 formed in controlled potential electrolysis (CPE) experiments.

4.2.3. Electrolysis studies.

In our previous study, we had shown that ~2.2 equiv NH_3 (per Fe) could be generated via controlled potential electrolysis (CPE; −2.3 V vs $Fc^{+/0}$) at a reticulated vitreous carbon working electrode, using $P_3^BFe^+$ as the (pre)catalyst in the presence of $HBAr^F_4$ (50 equiv) at −45 °C under an atmosphere of N_2. This yield of NH_3 corresponds to a ~25% FE which, while modest in terms of overall chemoselectivity, compares favorably to FE's typically reported for heterogeneous electrocatalysts for N_2RR that operate below 100 °C (< 2%).[2,26]

To further explore the possibility of using $P_3^BFe^+$ as an electrocatalyst for N_2RR, we have since surveyed various conditions to determine whether, from CPE experiments enhanced yields of NH_3 could be obtained. For example, screening various applied potentials (ranging from −2.1 to −3.0 V vs $Fc^{+/0}$), varying the concentrations of $P_3^BFe^+$ and $HBAr^F_4$, varying the ratio of acid to catalyst, and varying the rate at which acid was delivered to the system (initial loading, batch-wise addition, reloading, or continuous slow

addition) all led to no substantial improvement (<2.5 eq NH_3 obtained per Fe). Attempts to vary the ratio of electrode surface area to working compartment solution volume, either by employing smaller cell geometries or using different morphologies of glassy carbon as the working electrode (reticulated porous materials of different pore density or plates of different dimensions) also yielded no substantial improvement of NH_3 yield with respect to Fe. The replacement of $HBAr^F_4$ with 50 equiv of $[Ph_2NH_2][OTf]$ as the acid led to similar yields of NH_3 (**Table 4.2, entry 1**).

To investigate the potential effect of the $Cp^*_2Co^+$ additive, a systematic cyclic voltammetry study was undertaken. Traces of cyclic voltammograms (**Figure 4.4**) are provided for $[Ph_2NH_2][OTf]$ (both panels, gray trace), $Cp^*_2Co^+$ (panel **A**, yellow trace), $Cp^*_2Co^+$ with the addition of ten equiv of $[Ph_2NH_2][OTf]$ (panel **A**, green trace), $P_3{}^BFe^+$ (panel **B**, dark blue trace), $P_3{}^BFe^+$ with the addition of ten equiv of $[Ph_2NH_2][OTf]$ (panel **B**, light blue trace), and $P_3{}^BFe^+$ with the addition of five equiv of $Cp^*_2Co^+$ and ten equiv of $[Ph_2NH_2][OTf]$ (both panels, red trace).

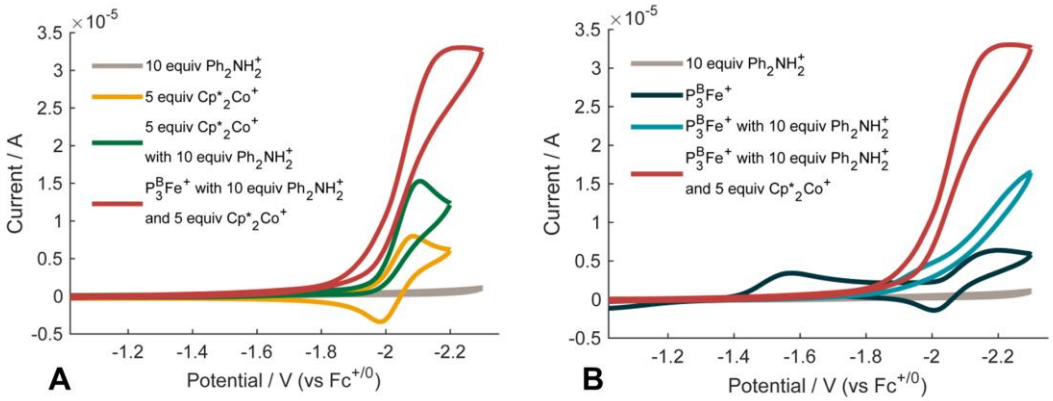

Figure 4.4. A) Cyclic voltammograms of 10 equiv $[Ph_2NH_2][OTf]$ (gray trace), 5 equiv $[Cp^*_2Co][BAr^F_4]$ ($Cp^*_2Co^+$) (yellow trace), 5 equiv $Cp^*_2Co^+$ with 10 equiv $[Ph_2NH_2][OTf]$ (green trace), and 1 equiv $P_3{}^BFe^+$ with 5 equiv of $Cp^*_2Co^+$ and 10 equiv $[Ph_2NH_2][OTf]$ (red trace). **B**) Cyclic voltammograms of 10 equiv $[Ph_2NH_2][OTf]$ (gray trace), 1 equiv

$P_3^BFe^+$ (dark blue trace), 1 equiv $P_3^BFe^+$ with 10 equiv $[Ph_2NH_2][OTf]$ (light blue trace), and $P_3^BFe^+$ with 5 equiv of $Cp^*_2Co^+$ and 10 equiv $[Ph_2NH_2][OTf]$ (red trace). All spectra are collected in 0.1 M $NaBAr^F_4$ solution in Et_2O at -35 °C using a glassy carbon working electrode, and externally referenced to the $Fc^{+/0}$ couple. Scan rate is 100 mV/s.

CPE studies were undertaken to characterize the reduction products associated with the red trace at ~−2.1 V vs $Fc^{+/0}$. These studies employed a glassy carbon plate electrode, a Ag/Ag^+ reference electrode that was isolated by a CoralPor™ frit and referenced externally to the ferrocene/ferricinium redox couple ($Fc^{+/0}$), and a solid sodium auxiliary electrode.[27] Unless otherwise noted, CPE experiments were performed at −2.1 V versus $Fc^{+/0}$, again with 0.1 M $NaBAr^F_4$ as the ether-soluble electrolyte, at −35 °C under an atmosphere of N_2, electrolysis was generally continued until the current measurement dropped to 1% of the initial current measured or until 21.5 hours had passed. The Supporting Information provides additional details.

CPE experiments were conducted with the inclusion of 0, 1, 5, and 10 equiv of $Cp^*_2Co^+$ with respect to $P_3^BFe^+$, using excess $[H_2NPh_2][OTf]$ as the acid. In the absence of added $Cp^*_2Co^+$, a significant amount of NH_3 was generated (2.4 equiv per Fe), consistent with the previous finding, in the presence of a strong acid, that $P_3^BFe^+$ can electrolytically mediate N_2-to-NH_3 conversion.[6d] We found that inclusion of 1.0 equiv of $Cp^*_2Co^+$ significantly enhanced the NH_3 yield, by a factor of 1.5 and led to improvements in the FE (**Table 4.2, entry 2**). The data provide a total yield, with respect to both Fe and Co, that confirm modest, but unequivocal, N_2RR electrocatalysis. The best NH_3 yield we have observed, in a single-run experiment, was 4.4 equiv per Fe.

Increasing the amount of added $Cp^*_2Co^+$ did not affect the NH_3 yield (**entry 3, 5**). However, the addition of a second loading of [Ph2NH2][OTf] following the first electrolysis (**entry 4**) followed by additional electrolysis, leads to an improved yield of NH_3 suggesting that some active catalyst is still present after the first run.[6d,9] Notably when a CPE experiment that did not include added $Cp^*_2Co^+$ was reloaded with additional acid after electrolysis and electrolyzed again the yield of NH_3 did not improve above the levels obtained from a single loading of acid (2.2 equiv NH_3 per Fe).

Table 4.2. Yields and Faradaic Efficiencies of NH_3 from CPE Experiments with $P_3^BFe^+$

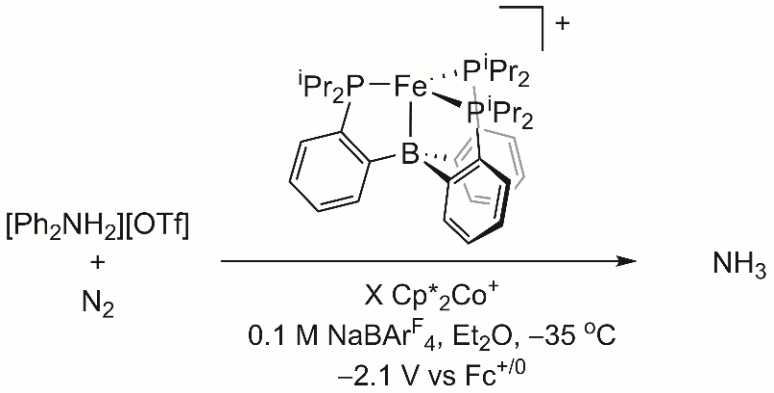

Entry	Equiv $Cp^*_2Co^+$	Equiv NH_3 (per Fe)	Equiv NH_3 (per Co)	NH_3 FE (%)
1	0	2.6 ± 0.4	—	22 ± 6

2	1	4.0 ± 0.6	4.0 ± 0.6	28 ± 5
3	5	4.0 ± 0.6	0.8 ± 0.1	25 ± 3
4[a]	5	5.5 ± 0.9	1.1 ± 0.2	19 ± 1
5	10	4 ± 1	0.4 ± 0.1	24 ± 7
6[b]	5	0.9 ± 0.4	0.2 ± 0.1	6 ± 3
7[c]	5	1.9 ± 0.2	0.4 ± 0.1	10 ± 1

All CPE experiments conducted at −2.1 V vs $Fc^{+/0}$ with 0.1 M $NaBAr^F_4$ in Et_2O as solvent, cooled to −35 °C under an N_2 atmosphere, featuring a glassy carbon plate working electrode, Ag/Ag^+ reference couple isolated by a CoralPor™ frit referenced externally to $Fc^{+/0}$, and a solid sodium auxiliary electrode. Working and auxiliary chambers separated by a sintered glass frit. See SI for further experimental details, controls, and additional data. [a]After initial electrolysis with 50 equiv $[Ph_2NH_2][OTf]$, an additional 50 equiv $[Ph_2NH_2][OTf]$ in 0.1 M $NaBAr^F_4$ Et_2O solution was added to the working chamber, via syringe through a rubber septum, followed by additional CPE at −2.1 V vs $Fc^{+/0}$. [b]$[PhNH_3][OTf]$ employed as the acid. [c]$[^{2,6\text{-Cl}}PhNH_3][OTf]$ employed as the acid.

CPE of $P_3^BFe^+$ in the presence of $Cp^*_2Co^+$ was also explored with other acids, replacing $[Ph_2NH_2][OTf]$ in these experiments with $[^{2,6\text{-Cl}}PhNH_3][OTf]$ led to lower yields of NH_3 and $[PhNH_3][OTf]$ led to even lower yields of NH_3 (Table 4.1, entries 7 and 6

respectively). The lower but nonzero yield of NH_3 provided by [$PhNH_3$][OTf] in these CPE experiments is consistent with chemical trials employing various acids (vide supra) and can be rationalized similarly by the relative pK_a of the acids (Table 4.1). The intermediate yield of NH_3 provided by [$^{2,6\text{-Cl}}PhNH_3$][OTf] in these CPE experiments is less consistent with a simple pK_a consideration, suggesting that additional factors contribute to acid compatibility with these CPE conditions perhaps including the relative stability of the acid or conjugate base to electrolysis.

To probe whether electrode-immobilized iron might contribute to the N_2RR electrocatalysis, X-ray photo-electron spectroscopy (XPS) was used to study the electrode. After a standard CPE experiment with $P_3^BFe^+$, 5 equiv of $Cp^*_2Co,^+$ and 50 equiv [Ph_2NH_2][OTf], the electrode was removed, washed with fresh 0.1 M $NaBAr^F_4$ Et_2O solution, then fresh Et_2O, and the electrode surface was then probed by XPS. A *very low* coverage of Fe (<0.3 atom % Fe) was detected in the post-electrolysis material; no Fe was detected on a segment of the electrode which was not exposed to the electrolytic solution. This observation implies a modest degree of degradation of $P_3^BFe^+$ over the course of a 15 hour CPE experiment. Worth noting is that no Co was detected on the post-electrolysis electrode.

To test whether the small amount of deposited Fe material might be catalytically active for N_2RR, following a standard CPE experiment the electrode was removed from the cold electrolysis solution, washed with fresh 0.1 M $NaBAr^F_4$ Et_2O at −35 °C (the electrode itself was maintained at −35 °C at all times), and then used for an additional CPE experiment, under identical conditions except that $P_3^BFe^+$ was excluded. This CPE experiment yielded no detectable NH_3. The charge passed, and H_2 yield, were very similar

to a "no $P_3^BFe^+$" control experiment conducted with a freshly cleaned electrode (See SI for further details). Accordingly, a CPE experiment in the absence of $P_3^BFe^+$ demonstrated that $Cp^*_2Co^+$ serves as an effective electrocatalyst for HER with $[Ph_2NH_2][OTf]$ as the acid source, but does not catalyze the N_2RR reaction (0% FE for NH_3, 76% FE for H_2; see SI). This background HER and the observed catalytic response to the addition of $[Ph_2NH_2][OTf]$ at the $Cp^*_2Co^{+/0}$ couple provides circumstantial evidence for the formation of a protonated decamethylcobaltocene intermediate, $Cp^*(\eta^4\text{-}C_5Me_5H)Co^+$ on a timescale similar to that of the N_2RR mediated by $P_3^BFe^+$.

To probe the possibility that the sodium auxiliary electrode used in the CPE experiments might play a non-innocent role as a chemical reductant, a standard CPE experiment with $P_3^BFe^+$, 5 equiv $Cp^*_2Co^+$, and 50 equiv $[Ph_2NH_2][OTf]$ was assembled, but was left to stir at −35 °C for 43 hours without an applied potential bias. This experiment yielded 0.3 equiv NH_3 (relative to Fe), suggesting that background N_2RR due to the sodium auxiliary electrode is very minor. To ensure the NH_3 produced was derived from the N_2 atmosphere during these electrolysis experiments, as opposed to degradation of the acid used, a standard CPE experiment using $P_3^BFe^+$, 5 equiv $Cp^*_2Co^+$, and 50 equiv of $[Ph_2{}^{15}NH_2][OTf]$ was performed. Only $^{14}NH_3$ product was detected.

We also sought to compare the chemical N_2RR catalysis efficiency of the $P_3^BFe^+$ catalyst under conditions similar to those used for electrocatalysis. Hence, chemical catalysis with $P_3^BFe^+$, employing Cp^*_2Co as a reductant and $[Ph_2NH_2][OTf]$ as the acid, at −35 °C in a 0.1 M $NaBAr^F_4$ Et_2O solution, afforded lower yields of NH_3 (1.8 ± 0.7 equiv of NH_3 per Fe) than the yields observed via electrolysis with $Cp^*_2Co^+$ as an additive. The lower yields of NH_3 in these chemical trials, compared with our previously reported

conditions (12.8 ± 0.5 equiv of NH_3 per Fe),[Error! Bookmark not defined.] may be attributable to i ncreased competitive HER resulting from a more solubilizing medium (0.1 M $NaBAr^F{}_4$ Et_2O vs pure Et_2O) and a higher temperature (−35 °C vs −78 °C).[Error! Bookmark not defined.] T hese results illustrate that an electrochemical approach to NH_3 formation can improve performance, based on selectivity for N_2RR, of a molecular catalyst under comparable conditions.

4.3. Conclusion

Herein we report the first pK_a studies on a synthetic nitrogenase and find a strong correlation between pK_a and N_2RR efficiency. Chemical studies revealed that, on their own, the anilinium triflate acids employed in catalysis are unable to form the N−H bonds in early-stage N_2RR intermediates. We propose that the insolubility of these acids prevents the sufficiently rapid proton transfer necessary to capture the critical, unstable $P_3{}^BFe$=NNH intermediate. Under catalytic conditions, we believe that the presence of the metallocene reductant ($Cp^*{}_2Co$) is critical, as that species can be protonated to form $Cp^*(\eta^4\text{-}C_5Me_5H)Co^+$ which in turn plays a key role in N−H bond formation. This leads to the intriguing conclusion that an intermediate on the background HER pathway is actually a critical species in productive N_2RR chemistry.

We thus investigated the protonation of $Cp^*{}_2Co$ by anilinium triflate acids using DFT. This study unveiled that the pK_a effect on the N_2RR efficiency could be explained by the variation in the kinetics and thermodynamics of $Cp^*{}_2Co$ protonation by the different acids. Detailed investigation of the reactivity of $Cp^*(\eta^4\text{-}C_5Me_5H)Co^+$ with the critical $P_3{}^BFe$=NNH intermediate revealed that indeed PCET reactivity, either synchronous or

asynchronous, was favorable and proceeds with only a small barrier suggesting that this intermediate could indeed be rapidly trapped by this reagent. Although we have highlighted this particular reaction, we believe $Cp^*(\eta^4\text{-}C_5Me_5H)Co^+$ may be involved in a variety of N−H bond forming reactions during catalysis. Indeed given the widespread use of metallocene reductants in chemical N_2RR, we believe that this type of PCET reactivity may be an overlooked mechanism for N–H bond formation.

Intrigued by the idea that the conjugate acid of Cp^*_2Co was playing an important role in N−H bond formation, we decided to investigate the effect of $Cp^*_2Co^+$ as a catalytic additive in electrochemical N_2RR experiments. Indeed despite the fact that $Cp^*_2Co^+$ itself only catalyzes HER under the conditions employed for electrocatalysis, we found that its inclusion in CPE experiments containing $P_3{}^BFe^+$ and acid led to improvements in the yield of NH_3 and the FE for NH_3. This system represents the first unambiguous example of electrocatalytic N_2RR with a soluble, molecular coordination complex. This discovery opens the door for further studies in this area. Although the yield of NH_3 is modest the FE is far superior to almost all known heterogenous electrocatalysts that operate at low temperature, suggesting that such studies could provide important design criteria in the development of electrocatalytic N_2RR.

4.4. References

[1] (a) Yandulov, D. V.; Schrock, R. R. *Science* **2003,** *301,* 76. (b) Arashiba, K.; Miyake, Y.; Nishibayashi, Y. *Nat. Chem.* **2010,** *3,* 120. (c) Anderson, J. S.; Rittle, J.; Peters, J. C. *Nature* **2013,** *501,* 84. (d) Imayoshi, R.; Tanaka, H.; Matsuo, Y.; Yuki, M.; Nakajima, K.; Yoshizawa, K.; Nishibayashi, Y. *Angew. Chem. Int. Ed.* **2015**, *21*, 8905. (e) Ung, G.;

Peters, J. C. *Angew. Chem. Int. Ed.* **2015**, *54*, 532. (f) Kuriyama, S.; Arashiba, K.; Nakajima, K.; Matsuo, Y.; Tanaka, H.; Ishii, K.; Yoshizawa, K.; Nishibayashi, Y. *Nat. Commun.* **2016,** *7*, 12181. (g) Hill, P. J.; Doyle, L. R.; Crawford, A. D.; Myers, W. K.; Ashley, A. E. *J. Am. Chem. Soc.* **2016**, *138*, 13521. (h) Buscagan, T. M.; Oyala, P. H.; Peters, J. C. *Angew. Chem. Int. Ed.* **2017**, *56*, 6921. (i) Wickramasinghe, L. A.; Ogawa, T.; Schrock, R. R.; Müller, P. *J. Am. Chem. Soc.* **2017,** *139*, 9132. (j) Fajardo Jr., J.; Peters, J. C. *J. Am. Chem. Soc.* **2017**, *139*, 16105.

[2] (a) Shipman, M. A.; Symes, M. D. *Catal. Today* **2017,** *286*, 57. (b) Kyriakou, V.; Garagounis, I.; Vasileiou, E.; Vourros, A.; Stoukides, M. *Catal. Today* **2017,** *286*, 2.

[3] (a) McKone, J. R.; Marinescu, S. C.; Brunschwig, B. S.; Winkler, J. R.; Gray, H. B. *Chem. Sci.* **2014,** *5*, 865. (b) Bullock, R. M.; Appel, A. M.; Helm, M. L. *Chem. Commun.* **2014,** *50*, 3125.

[4] (a) Benson, E. E.; Kubiak, C. P.; Sathrum, A. J.; Smieja, J. M. *Chem. Soc. Rev.* **2009,** *38*, 89. (b) Appel, A. M.; Bercaw, J. E.; Bocarsly, A. B.; Dobbek, H.; DuBois, D. L.; Dupuis, M.; Ferry, J. G.; Fujita, E.; Hille, R.; Kenis, P. J. A.; Kerfeld, C. A.; Morris, R. H.; Peden, C. H. F.; Portis, A. R.; Ragsdale, S. W.; Rauchfuss, T. B.; Reek, J. N. H.; Seefeldt, L. C.; Thauer, R. K.; Waldrop, G. L. *Chem. Rev.* **2013,** *113*, 6621. (c) Francke, R.; Schille, B.; Roemelt, M. *Chem. Rev.* **2018,** *DOI: 10.1021/acs.chemrev.7b00459*.

[5] Zhang, W.; Lai, W.; Cao, R. *Chem. Rev.* **2017,** *117*, 3717.

[6] (a) Pickett, C. J.; Talarmin, J. *Nature* **1985,** *317*, 652. (b) Al-Salih, T. I.; Pickett, C. J. *J. Chem. Soc. Dalton Trans.* **1985**, 1255. (c) Pickett, C. J.; Ryder, K. S.; Talarmin, J. *J. Chem. Soc. Dalton Trans.* **1986**, 1453. (d) Del Castillo, T. J.; Thompson, N. B.; Peters, J. C. *J. Am. Chem. Soc.* **2016,** *138*, 5341.

[7] In this context a recent report in which the bioelectrosynthesis of ammonia by nitrogenase is coupled to H_2 oxidation is also noteworthy: Milton, R. D.; Cai, R.; Abdellaoui, S.; Leech, D.; De Lacey, A. L.; Pita, M.; Minteer, S. D. *Angew. Chem. Int. Ed.* **2017,** *56*, 2680.

[8] Very recently there was a report of electrolytic NH_3 synthesis by Cp_2TiCl_2 but although rates and Faradaic efficiencies are discussed no yields of NH_3 are reported: Jeong, E.-Y.; Yoo, C.-Y.; Jung, C. H.; Park, J. H.; Park, Y. C.; Kim, J.-N.; Oh, S.-G.; Woo, Y.; Yoon, H. C. *ACS Sustainable Chem. Eng.* **2017**, *5*, 9662.

[9] Chalkley, M. J.; Del Castillo, T. J.; Matson, B. D.; Roddy, J. P.; Peters, J. C. *ACS Cent. Sci.* **2017,** *3*, 217.

[10] In some cases the pK_a of a particular anilinium acid was already known in THF in which case this value was used. In cases where the pK_a was not reported in THF a literature procedure was used to appropriately convert the pK_a so that it would be comparable. See SI for details.

[11] Consistent with this observation is that efforts to use other weak, non-anilinium acids such as benzylammonium triflate and collidinium triflate also led to no observed NH_3 formation.

[12] These results are also consistent with our previous observation of $[Ph_2NH_2][OTf]$ (pK_a in THF of 3.2) yielding 72% ± 3 NH_3. See reference 9.

[13] Pham, D. N.; Burgess, B. K. *Biochemistry* **1993,** *32*, 13275.

[14] In some other reports on N_2RR by molecular catalysts, efficiencies for NH_3 have been reported for several acids but typically these acids span only a small pK_a range, electron yields are inconsistent, and variations are not explained.

[15] Anderson, J. S.; Cutsail III, G. E.; Rittle, J.; Connor, B. A.; Gunderson, W. A.; Zhang, L.; Hoffman, B. M.; Peters, J. C. *J. Am. Chem. Soc.* **2015,** *137*, 7803.

[16] Matson, B. D.; Peters, J. C. *ACS Catal.* **2018,** *8*, 1448.

[17] Grimme, S.; Antony, J.; Ehrlich, S.; Krieg, H. *J. Chem. Phys.* **2010**, *132*, 154104.

[18] (a) Tao, J.; Perdew, J. P.; Staroverov, V. N.; Scuseria, G. E., *Phys. Rev. Lett.* **2003,** *91*, 146401. (b) Weigend, F.; Ahlrichs, R., *Phys. Chem. Chem. Phys.* **2005,** *7*, 3297.

[19] We have found that this functional and basis set are able to reproduce accurately not only crystallographic details but also known singlet-triplet gaps, reduction potentials, and N−H BDFE's. For further detail see Reference 16.

[20] In this section we present DFT data that includes explicit OTf^- interactions. It should be noted that while the absolute thermodynamics and kinetics are dependent on the OTf^-, calculations in its absence suggest that the trends discussed here are more broadly applicable with respect to more non-coordinating anions.

[21] The reactivity of ring-functionalized Cp rings has been discussed previously in the context of hydride transfer in HER with 4d and 5d metals: (a) Pitman, C. L.; Finster, O. N. L.; Miller, A. J. M. *Chem. Commun.* **2016**, *52*, 9105. (b) Quintana, L. M. A.; Johnson, S. I.; Corona, S. L.; Villatoro, W.; Goddard, W. A.; Takase, M. K.; VanderVelde, D. G.; Winkler, J. R.; Gray, H. B.; Blakemore, J. D. *Proc. Natl. Acad. Sci.* **2016**, *113*, 6409. (c) Peng, Y.; Ramos-Garcés, M. V.; Lionetti, D.; Blakemore, J. D. *Inorg. Chem.* **2017**, *56*, 10824.

[22] Marcus, R. A. *J. Chem. Phys.* **1956**, *24*, 966–978.

[23] Iordanova, N.; Decornez, H.; Hammes-Schiffer, S. *J. Am. Chem. Soc.* **2001**, *123*, 3723–3733.

[24] We have assumed a PT/ET mechanism in which ET is rate limiting based on significantly lowered reorganization energies and barriers for PT compared to ET. See SI for full description.

[25] Koelle, U.; Infelta, P. P.; Graetzel, M., *Inorg. Chem.* **1988,** *27*, 879.

[26] Very recently there has been a report of electrocatalytic N_2RR under ambient conditions in ionic liquids with Fe nanoparticles that achieve FE's as high as 60%: Li, S.-J.; Bao, D.; Shi, M.-M.; Wulan, B.-R.; Yan, J.-M.; Jiang, Q., *Adv. Mater.* **2017,** *29*, 1700001.

[27] A sodium auxiliary electrode was employed because oxidation of Et_2O or $NaBAr^F{}_4$ at an inert electrode lead to prohibitively high compliance voltage requirements. Likewise due to the extensive diffusion between the working and auxiliary chambers the application of a counter redox process which produced an oxidation product which could diffuse to the working electrode and be re-reduced at −2.1 V vs $Fc^{+/0}$ lead to excessive nonproductive redox cycling between chambers over the course of the lengthy CPE experiments. Using sodium metal as an electrode material provided a suitable solution to these technical challenges as the product of its oxidation (Na^+) is stable to the CPE conditions. Concern regarding whether the sodium electrode could serve directly as a reducant in a chemical process to form NH_3 under these conditions was addressed in a control experiment described in the text.

Chapter 5. Predicting BDFE Values Using DFT

5.1. Introduction

As demonstrated in the preceding chapters of this thesis, the ability to efficiently and accurately predict the bond dissociation free-energies (BDFE) of highly reactive intermediates can be a powerful tool in investigating the mechanism of multi-proton, multi-electron reduction of N_2 (the N_2 reduction reaction, N_2RR).[1] Accordingly, there are a variety of studies that have attempted to quantify the strength of catalytically relevant E–H bonds ($BDFE_{E\text{-}H}$) in N_2RR intermediates.[1,2] These $BDFE_{E\text{-}H}$ values can provide crucial information regarding the stability and reactivity of catalytic intermediates, and can provide fundamental insight to guide experimental studies, particularly those which involve proton-coupled electron transfer (PCET).

Studies aimed at predicting $BDFE_{N\text{-}H}$ bonds strengths in N_2RR catalysis have established density functional theory (DFT) as a useful method for the prediction of relative BDFEs. DFT is most powerful, however, when it can be calibrated to experimental values and, as such, the accurate prediction of relative and absolute $BDFE_{E\text{-}H}$ values across a wide variety of E–H bonds, both metal bound and free, is highly desirable. In this chapter, a DFT method for the calibration of literature $BDFE_{E\text{-}H}$ values is presented which leads to the accurate (within 4 kcal/mol) prediction of both free and metal bound E–H bond strengths in the gas-phase. While the prediction of solvated $BDFE_{E\text{-}H}$ values is shown to have only slightly higher overall errors (ca. 5 kcal/mol) for organic E-H bonds, accurate calibration of solution phase metal bound E-H bonds remains less understood due to the relative lack of literature data. Nonetheless, similar empirical corrections appear to show similar

promise with a smaller library of literature data in MeCN and THF. In sum, the method outlined in the following presents an efficient method for gas-phase $BDFE_{E-H}$ predictions and suggest simple empirical corrections that can allow for solution phase values within ca. 5 kcal/mol.

5.2. Calibration of Gas-Phase $BDFE_{E-H}$ Values

Gas-phase organic molecules provide an ideal starting point from which to begin calibrating a DFT method. This is due to the large library of literature values and the lack of any solvation induced weakening or strengthening of the E-H bond.[3] To investigate the efficacy of $BDFE_{E-H}$ prediction for gas-phase values, four common functionals, B3LYP,[4] BP86,[5] M06-L[6] and TPSS,[7] were used to calculate known gas-phase $BDFE_{E-H}$ values using a common and efficient basis set (def2-SVP).[8]

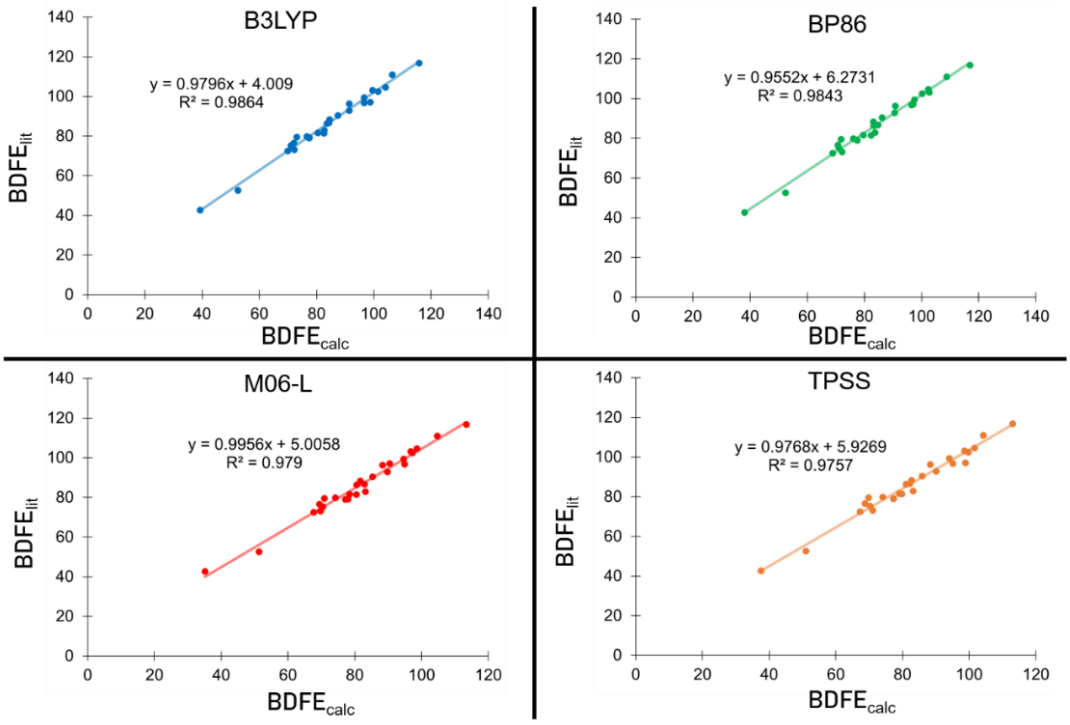

Figure 5.1. Plots of $BDFE_{calc}$ vs $BDFE_{lit}$ for known gas-phase literature values using 4 common functionals.

As shown in Figure 5.1, all four functionals produced calibration curves with similar parameters (slope from 0.95 to 1.0; intercept from 4 to 6.5; Figure 5.1). Using each calibration equation, errors were calculated for each functional (Table 5.1) and were shown to vary between 2.3 (B3LYP) and 4.6 (M06-L). It is further noted that the hybrid functional, B3LYP, was found to have significantly lowered errors compared to the pure functionals. The ability of any of the these functionals to be effectively reproduce gas-phase $BDFE_{E-H}$ values, however, is a useful observation. In particular, our research has shown large functional dependences on properties of P_3^EFe species, with TPSS and BP86 providing

superior predictions for spin-state energy gaps, reduction potentials and $BDFE_{N-H}$ values than B3LYP and M06-L. Notably, B3LYP and M06-L have been observed to favor high-spin states, a factor that is crucial in metal bound $BDFE_{E-H}$ predictions but not relevant in prediction of free, organic E-H bond strengths.

In addition to evaluating the overall errors for gas-phase $BDFE_{E-H}$ values, the data in Figure 5.1 and Table 5.1 allow us to confirm that these errors are normally distributed. Normal probability plots of the errors from each functional are shown in Figure 5.2. Notably, all four functionals tested shown a linear relationship and r-values that are greater than the critical value of 0.96 at a 5% confidence level. Accordingly, it is reasonable to assume that upon application of the lines of best fit shown in Figure 5.1, any errors are normally distributed.

Table 5.1. Errors Obtained from Figure 5.1.

O-H Bonds	B3LYP	BP86	M06-L	TPSS
HOO–H	−4.1	−4.7	−4.1	−5.6
MeO–H	−3.0	−3.4	−3.4	−4.2
EtOO–H	−2.0	−2.8	−2.5	−3.6
HO–H	−2.7	−0.8	−1.8	−3.3
PhOH	−0.8	−0.8	−1.1	−1.6
OO–H	−0.3	−0.1	−2.8	−0.1
HC(O)OO–H	−0.3	0.4	0.7	−0.6

$O–H^-$	−1.6	1.3	−1.8	−0.9
C–H Bonds	B3LYP	BP86	M06−L	TPSS
$Me_3C–H$	−1.5	−2.7	−2.1	−1.6
Me_2CH_2	−0.8	−1.9	−0.5	−0.6
C_6H_6	1.2	−0.7	−1.5	0.5
C_2H_4	0.8	−0.6	−0.7	0.8
C_2H_6	0.7	−0.1	1.4	1.0
$PhCH_3$	1.1	0.7	1.5	1.5
CH_4	1.8	1.5	2.7	2.0
CpH	1.4	2.0	1.2	2.1
N–H Bonds	B3LYP	BP86	M06−L	TPSS
Et_2NH	−0.6	−0.7	−1.3	−1.3
NH_2NH_2	−0.1	−0.6	−0.3	−1.0
NH_3	−0.8	−0.1	−0.2	−1.6
NH_4^+	0.5	1.0	1.0	−0.6
$PhNH_2$	3.3	3.4	3.6	2.4
NHNH	2.8	3.7	3.5	3.1
Other E–H Bonds	B3LYP	BP86	M06−L	TPSS
PhSH	−1.8	−1.2	−0.2	−0.7
MeSH	0.6	1.0	3.3	2.2

EtSH	0.7	1.2	2.7	2.2
H_2S	1.9	3.2	4.8	4.1
H_2	3.5	1.8	−2.2	5.3
MSE	0.0	0.0	0.0	0.0
MUE	2.3	3.7	4.6	4.0

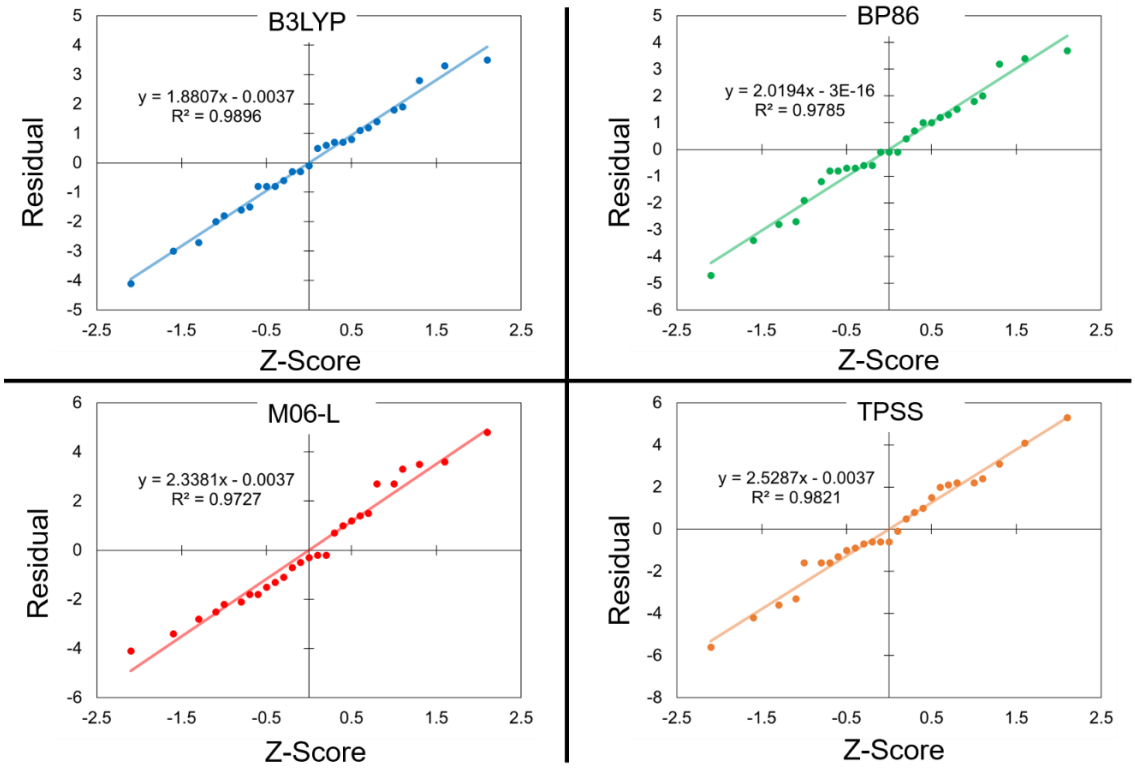

Figure 5.2. Normal probability plots for the errors in Table 5.1.

5.3. Solution Phase $BDFE_{E-H}$ Values

Given the similarity between functional calibration and the accuracy with which TPSS has been shown to treat P_3^EFe complexes, we turned our attention to its use in solution phase $BDFE_{E-H}$ predictions and metal bound $BDFE_{E-H}$ predictions. Within the context of free, organic $BDFE_{E-H}$ species, a simple empirical formula (eq. 5.1) was shown to produce only slightly higher errors when compared to the gas-phase values. As shown in Table 5.2, the combined errors for $BDFE_{soln}$ range from 0.2 to 1.1 kcal/mol greater than the baseline error in $BDFE_{gas}$ (4.0 kcal/mol; Table 5.1).

$$BDFE_{soln} = BDFE_{gas} + C_{solv} \quad \text{(eq. 5.1)}$$

Table 5.2. Solvent correction (C_{solv}) and total rrors for several E-H bond/solvent combinations[a] using TPSS/def2-SVP

	C_{DMSO} {Total Error}[b]	C_{MeCN} {Total Error}	C_{C6H6} {Total Error}
C-H, H-H bonds	+4.9 kcal/mol {4.4 kcal/mol)	+3.9 kcal/mol {4.2 kcal/mol}	+8.3 kcal/mol {4.6 kcal/mol}
O-H, N-H, S-H bonds	+11.0 kcal/mol {5.1 kcal.mol}	+10.1 kcal/mol {4.8 kcal/mol}	N. D.

[a]Using TPSS/def2-SVP level of theory. [b] Error = $(\sqrt{[\delta(BDFE_{gas})^2 + (\delta C_{solv})^2]})$

5.4. Transition Metal Bound E–H Bonds

Transition metal bound E–H bonds provide additional challenges, in large part due to a smaller library of literature values and the lack of any well-defined values in the gas-phase. Application of the gas-phase calibration (TPSS; Figure 5.1) and eq. 5.1 provides solvent correction terms for transition metal bound $BDFE_{E\text{-}H}$ values in THF and MeCN (Table 5.3). It is notable that the correction terms show a significantly decreased magnitude and opposite sign. The decrease in the magnitude of solvent corrections for transition metal species is not surprising, as the large size and comparatively constant ligand entropy in the E–H and $E^{\bullet}$ species leads to decreased relative role of entropic factors. While not investigated in this research, the $BDFE_{E\text{-}H}$ values of several transition metal species are known in DMSO and H_2O, leading to the possible expansion of the approached described to transition metal systems in polar and/or protic solvents.

Table 5.3. Solvent correction (C_{solv}) and total errors for several transition metal based E-H bond/solvent combinations

	C_{solv}	Total Error
MeCN	–3.2 kcal/mol	4.1 kcal/mol
THF	–2.5 kcal/mol	4.4 kcal/mol

[a]Using TPSS/def2-TZVP(TM); def2-SVP. [b] Error = $(\sqrt{[\delta(BDFE_{gas})^2 + (\delta C_{solv})^2]})$

5.5. Conclusions

In conclusion, a simple and efficient method for predicting free and transition metal bound $BDFE_{E-H}$ values is presented. The method describe relies first on producing a calibration curve using literature data for $BDFE_{E-H}$ species in the gas-phase. It has been shown with four common functionals that these calibrations can be accomplished with errors of ca. 4 kcal/mol. Further, it has been shown that an empirical correction for the type of bond and solvent can be added to these gas-phase values with only marginally increased total errors (0.2 – 1.1 kcal/mol; total errors: 4 – 5 kcal/mol).

5.6. References

[1] (a) Matson, B. D.; Peters, J. C. *ACS Catalysis*, **2018**, *8*, 1448-1455. (b) Chalkley, M. J.; Del Castillo, T. J.; Matson, B. D.; Roddy, J. P.; Peters, J. C. *ACS Central Science* **2017**, *3*, 217-223.

[2] (a) Rittle, J.; Peters, J. C. *J. Am. Chem. Soc.* **2017**, *139*, 3161–3170. (b) Pappas, I.; Chirik, P. J. *J. Am. Chem. Soc.* **2016**, *138*, 13379.

[3] (a) Warren, J. J.; Tronic, T. A.; Mayer, J. M. *Chem. Rev.* **2010**, *110*, 6961–7001. (b) Yandulov, D. V.; Schrock, R. R. *Inorg. Chem.* **2005**, *44*, 1103.

[4] (a) Becke, A. D. *J. Chem. Phys.* **1993**, *98*, 5648-5652. (b) Lee, C.; Yang, W.; Parr, R. G. *Phys. Rev. B.* **1988**, *37*, 785-789. (c) Vosko, S. H.; Wilk, L.; Nusair, M.; *Can. J. Phys.* **1980**, *58*, 1200-1211. (d) Stephens, P. J.; Devlin, F. J.; Chabalowski, C. F.; Frisch, M. J. *J. Phys. Chem.* **1994**, *98*, 11623-11627.

[5] (a) Becke, A. D. *Phys. Rev. A.* **1988**, *38*, 3098-30100. (b) Perdew, J. P. *Phys. Rev. B.* **1986**, *33* 8822-8824.

[6] Zhao, Y.; Schultz, N. E.; Truhlar, D. G. *J. Chem. Theory and Comput.* **2006**, *2*, 364-382.

[7] Tao, J. M.; Perdew, J. P.; Staroverov, V. N.; Scuseria, G. E. *Phys. Rev. Lett.* **2003**, *91*, 146401.

[8] Weigend, F.; Ahlrichs, R. *Phys. Chem. Chem. Phys.* **2005**, *7*, 3297–3305.

Appendix 1. Supplementary Data for Chapter 2

A1.1. General Computational Details

All stationary point geometries were calculated using dispersion corrected DFT-D_3[1] with a TPSS functional,[2] a def2-TZVP basis set on transition metals and a def2-SVP basis set on all other atoms.[3] Calculations were performed, in part, using Xtreme Science and Engineering Discovery Environment (XSEDE) resources.[4] Calculations were performed on the full P_3^EFe scaffolds. Geometries were optimized using the NWChem 6.5 package or Orca 3.0.3 package.[5] All single point energy, frequency and solvation energy calculations were performed with the Orca 3.0.3 package. Frequency calculations were used to confirm true minima and to determine gas phase free energy values (G_{gas}). Single point solvation calculations were done using an SMD solvation model[6] with diethyl ether solvent and were used to determine solvated internal energy (E_{soln}). Free energies of solvation were approximated using the difference in gas phase internal energy (E_{gas}) and solvated internal energy ($\Delta G_{solv} \approx E_{soln} - E_{gas}$) and the free energy of a species in solution was then calculated using the gas phase free energy (G_{gas}) and the free energy of solvation ($G_{soln} = G_{gas} + \Delta G_{solv}$). All reduction potentials were calculated referenced to $Fc^{+/0}$ using the standard Nernst relation $\Delta G = -nFE^0$.

A1.2. Fe–H Formation

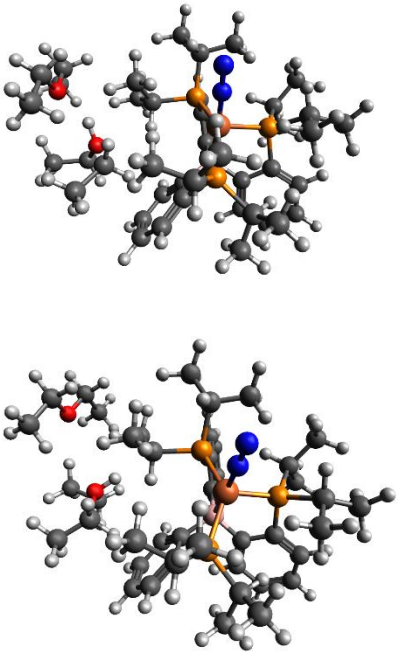

Figure A1.1. Structure of $P_3^BFeN_2^-$ + $(Et_2O)_2H^+$ immediately before (top) and after (bottom) dissociation of a Et2O moiety. The relaxed surface scan reveals little change in the $P_3^BFeN_2^-$ unit before Et_2O dissociation, indicative of the presence of a $(Et_2O)_2H^+ \leftrightarrow (Et_2O)H^+ + Et_2O$ pre-equilibrium.

A1.3. BDFE Calculations

Bond dissociation free energies (BDFE) of X–H bonds were calculated in the gas-phase using a series of known reference compounds.[7] The free-energy difference between the H-atom donor/acceptor pair was calculated based on the thermochemical information provided by frequency calculations after structure optimizations using the procedure described in the general computational section. A linear plot of ΔG *vs* $BDFE_{lit}$ was

generated to form a calibration curve (**Figure A1.1**). BDFE predictions were generated by application of the line of best fit to the calculated ΔG of the unknown species. Errors were calculated by application of the trend line to the calculated free-energies of known species and comparison to their literature BDFE value. Errors are reported as the average of $BDFE_{calc}$-$BDFE_{lit}$ (mean signed error, MSE = 0.0) and the average of the absolute values of $BDFE_{calc}$-$BDFE_{lit}$ (mean unsigned error, MUE = 1.3).

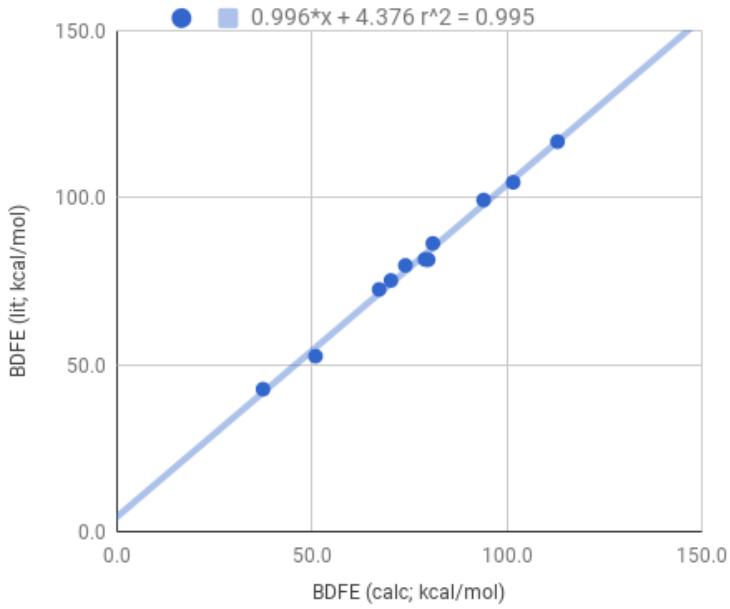

Figure A1.2. Plot of calculated BDFE vs literature BDFE. Line of Best fit shown with equation along with r^2 value.

Table A1.1. Summary of BDFEs used for calibration.

	ΔG (E-H)	**ΔG (E*)**	**ΔG_{calc}**	**$BDFE_{lit}$**	**Error**

$PhNH_2$	-287.4	-286.7	79.8	81.5	-2.4
NH_2NH_2	-111.8	-111.1	67.3	72.6	1.2
PhSH	-630.2	-629.5	70.3	75.3	0.9
PhH	-271.3	-270.7	79.0	81.6	-1.5
C_6H_6	-232.1	-231.4	101.6	104.7	-0.9
PhOH	-307.2	-306.6	74.0	79.8	1.7
NH_3	-56.5	-55.8	94.0	99.4	1.3
NHNH	-110.6	-110.0	51.0	52.6	-2.6
Me_2NH	-213.6	-212.9	81.0	86.4	1.3
NH_4 (+)	-56.8	-56.1	113.0	116.9	0.0
OOH	-150.8	-150.2	37.5	42.7	1.0
				MUE	1.4
				MSE	0.1

A1.4. Approximation of $P_3^EFe(NNH_y)$ Radius

The radius of $P_3^EFe(NNH_y)$ was approximated by using the average molar volume of several relevant crystal structures to determine a radius assuming a spherical molecule.

Table A1.2. Volume and Calculated Radius of Previous Characterized P_3^EFe Species from XRD Data

	Volume (Å^3)	**r_{calc} (Å)**	**Ref**
$P_3^{Si}Fe(N_2)$	881.2	5.9	8
$P_3^{Si}Fe(CN)$	1101.9	6.2	9

$P_3^{Si}Fe(CNMe)$	915.7	6.0	10
$P_3^{C}Fe(N_2)$	869.3	5.9	11
$P_3^{C}Fe(H)(N_2)$	869.8	5.9	9
$P_3^{B}Fe(NH_2)$	866.1	5.9	12
		Average	6.0 Å
		Std Dev	0.1 Å

A1.5. Calculated Reorganization Energies

The inner-sphere reorganization energy for electron transfer ($\lambda_{is,ET}$) was estimated assuming non-adiabatic behavior and by calculating the difference between the single point energies of the relevant species in its ground state and the corresponding single point energy of this ground state in the oxidized or reduced geometry.

$$\lambda_{is,ET} = [E(Fe^{ox}{}_{ox}) - E(Fe^{ox}{}_{red})] + [E(Fe^{red}{}_{red}) - E(Fe^{red}{}_{ox})] \qquad \text{(Eq. A1.1)}$$

Relative reduction barriers were approximated by first defining the barrier for $P_3^{B}Fe(NNH_2)^+$ to be 1.0 kcal/mol. Subsequent back-calculation of λ_{tot} yielded solutions of 30.5 kcal/mol and 56.5 kcal/mol, corresponding to the solutions in the inverted and normal regimes, respectively. The reorganization energy leading to the inverted solution would imply very small energies for KC_8 and solvent reorganization ($\lambda_{KC8} + \lambda_{OS} = 7.5$ kcal/mol). This led us to assume that the reduction steps were in the normal region. To check this assumption, outer-sphere reorganization energy was approximated using a continuum

model.[13] For electron transfer ($\lambda_{os,ET}$) reactions the KC_8 reductant was modeled as an electrode surface ($r_{KC8} >> r_{cat}$). The radius of the P_3^EFe molecules (r_{cat}; Eq. 2) was approximated using the volumes of several relevant crystal structures. The values for the static and optical dielectric constant (ε_s and ε_{op}) of diethyl ether were taken as the values used in the SMD solvation model. This value was approximated at 33 kcal/mol, consistent with the reductions of interest occurring in the normal region. Accordingly, the total reorganization for $P_3^BFe(NNH_2)^+$ reduction (G* ≡ 1.0 kcal/mol) was assumed to be 56.5 kcal/mol. Perturbation of this value by the differences between $\lambda_{IS}^{Si/C}$ and λ_{IS}^{B} lead to the relative barriers shown in **Table S3.**

Table A1.3. Summary of Calculated Reorganization Energies[a]

Redox Couple	$\lambda_{IS,ET}$	$\lambda_{OS} + \lambda_{KC8}$	G^*_{rel}
$P_3^BFe(NNH_2)^{+/0}$	23.0	33.5	1.0[b]
$P_3^{Si}Fe(NNH_2)^{+/0}$	29.7	33.5	4.4
$P_3^CFe(NNH_2)^{+/0}$	29.7	33.5	5.2

[a] All energies are in kcal/mol [b] G* values expressed relative to that of $P_3^BFe(NNH_2)^+$ reduction, defined as 1.0 kcal/mol

A1.6. Determination of the Work Function

The work required to bring two cationic iron species together was approximated following the methods of Hammes-Schiffer and Mayer (Eq 1).[14]

$$w_r = \frac{e^2 Z_1 Z_2 f}{\epsilon_o r} \qquad \text{(eq. A1.2)}$$

Here Z_1 and Z_2 are the charges on each complex ($Z_1 = Z_2 = +1$) and e is the elementary charge. The distance between iron centers was taken as twice the radius of the P_3^EFe species (r = 12 Å) and ϵ_o is the static dielectric constant. The debye screening factor (f) was calculated using eq. 2.

$$f^{-1} = 1 + r\sqrt{\frac{8\pi N_A e^2 \mu}{10^{27}\epsilon_o k_B T}} \qquad \text{(eq. A1.3)}$$

Where μ is the ionic strength (taken as [Fe] = 1.3 mM) and N_A are k_B Avogadro's number and the Boltzmann constant, respectively. The temperature was taken as the standard temperature for catalysis (T =195 K). Substitution of the appropriate values into Eq. 1 and 2 yields w_r = 5.2 kcal/mol.

A1.7. Summary of Wiberg Indices

Table A1.4. Summary of Wiberg Bond Indices for $P_3^EFe(N_2)$ complexes

P_3^BFe	Alpha	Beta	Total	$P_3^{Si}Fe$	Alpha	Beta	Total	P_3^CFe	Alpha	Beta	Total
Fe-N_1	0.2	0.2	0.9	Fe-N_1	0.2	0.3	1.0	Fe-N_1	0.2	0.3	1.0
Fe-N_2	0.1	0.1	0.4	Fe-N_2	0.1	0.1	0.4	Fe-N_2	0.1	0.1	0.4
N-N	0.7	0.6	2.6	N-N	0.6	0.6	2.6	N-N	0.6	0.6	2.5
Fe-B	0.1	0.1	0.4	Fe-Si	0.2	0.2	0.7	Fe-C	0.2	0.2	0.7
Fe-P_1	0.2	0.2	0.7	Fe-P_1	0.2	0.2	0.8	Fe-P_1	0.2	0.2	0.8
Fe-P_2	0.2	0.2	0.7	Fe-P_2	0.2	0.2	0.8	Fe-P_2	0.2	0.2	0.8
Fe-P_3	0.2	0.2	0.7	Fe-P_3	0.2	0.2	0.7	Fe-P_3	0.2	0.2	0.7

Table A1.5. Summary of Wiberg Bond Indices for $P_3^EFe(NNH)$ complexes

P_3^BFe	Alpha	Beta	Total	$P_3^{Si}Fe$	Alpha	Beta	Total	P_3^CFe	Alpha	Beta	Total
Fe-N_1	0.4	0.4	1.6	Fe-N_1	0.4	0.4	1.6	Fe-N_1	0.3	0.3	1.2
Fe-N_2	0.1	0.1	0.4	Fe-N_2	0.1	0.1	0.4	Fe-N_2	0.0	0.0	0.2
N-N	0.5	0.4	1.8	N-N	0.4	0.4	1.8	N-N	0.4	0.4	1.5
N-H	0.2	0.2	0.8	N-H	0.2	0.2	0.8	N-H	0.2	0.2	0.8

Fe-B	0.1	0.1	0.5	Fe-Si	0.2	0.2	0.7	Fe-C	0.1	0.1	0.5
Fe-P_1	0.2	0.2	0.7	Fe-P_1	0.2	0.2	0.8	Fe-P_1	0.2	0.2	0.7
Fe-P_2	0.2	0.2	0.8	Fe-P_2	0.2	0.2	0.8	Fe-P_2	0.2	0.2	0.8
Fe-P_3	0.2	0.2	0.8	Fe-P_3	0.2	0.2	0.8	Fe-P_3	0.2	0.2	0.7

Table A1.6. Summary of Bond Indices for $P_3^EFe(NNH_2)$ complexes

P_3^BFe	**Alpha**	**Beta**	**Total**	**$P_3^{Si}Fe$**	**Alpha**	**Beta**	**Total**	**P_3^CFe**	**Alpha**	**Beta**	**Total**
Fe-N_1	0.5	0.5	1.9	Fe-N_1	0.2	0.4	1.2	Fe-N_1	0.3	0.4	1.4
Fe-N_2	0.0	0.0	0.2	Fe-N_2	0.0	0.0	0.2	Fe-N_2	0.0		0.1
N-N	0.3	0.3	1.2	N-N	0.4	0.3	1.4	N-N	0.4	0.3	1.4
N-H	0.2	0.2	0.8	N-H	0.2	0.2	0.8	N-H	0.2	0.2	0.8
N-H	0.2	0.2	0.8	N-H	0.2	0.2	0.8	N-H	0.2	0.2	0.8

Fe-B	0.1	0.1	0.4	Fe-Si	0.2	0.2	0.7	Fe-C	0.1	0.1	0.5
Fe-P_1	0.2	0.2	0.8	Fe-P_1	0.2	0.2	0.8	Fe-P_1	0.2	0.2	0.8
Fe-P_2	0.2	0.2	0.8	Fe-P_2	0.2	0.2	0.8	Fe-P_2	0.2	0.2	0.8
Fe-P_3	0.2	0.2	0.8	Fe-P_3	0.2	0.2	0.8	Fe-P_3	0.2	0.2	0.8

Table A1.7. Summary of Wiberg Bond Indices for $P_3^EFe(N(4\text{-}OMe\text{-}Ph))$

P_3^BFe	**Total**
Fe-N_1	1.8
N-C	1.2
Fe-B	0.4
Fe-P_1	0.8
Fe-P_2	0.8
Fe-P_3	0.8

Table A1.8. Summary of Wiberg Bond Indices for C_2H_4 and C_2H_5

C_2H_4	Alpha	Beta	Total	C_2H_5	Alpha	Beta	Total
C_1-H_1	0.94	0.94	1.9	C_1-H_1	0.24	0.24	0.96
C_1-H_2	0.94	0.94	0.2	C_1-H_2	0.24	0.24	0.96
C_1-C_2	0.94	0.94	1.2	C_1-C_2	0.23	0.23	0.93
C_2-H_3	0.94	0.94	0.8	C_2-H_3	0.23	0.23	0.93
C_2-H_4	2.05	2.05	0.8	C_2-H_4	0.23	0.22	0.90
				C_2-H_5	0.27	0.28	1.10

A1.8. Comparison of Calculated to Known Experimental Values

Table A1.9. Comparing of calculated to experimental values for several parameters of interest.

	Parameter	Calculated	Experimental	Ref
$P_3^{Si}Fe(NNMe_2)^+$	Singlet-Triplet Gap	6.9 kcal/mol	6.0	9
$P_3^{Si}Fe(NNMe_2)^+$	Reduction Potential	-1.81 V vs $Fc^{+/0}$	-1.73 V vs $Fc^{+/0}$	9
$P_3^{B}Fe(NNMe_2)$	Singlet-Triplet Gap	5.5 kcal/mol	4.0 kcal/mol	15
$P_3^{B}Fe(NNMe_2)$	Reduction Potential	-1.29 V vs $Fc^{+/0}$	-1.20 V vs $Fc^{+/0}$	14
$P_3^{Si}Fe(CNH)$	$BDFE_{N-H}$	43.5 kcal/mol	41.4 kcal/mol	9
$P_3^{Si}Fe(CNH)$	$BDFE_{N-H}$	61.8 kcal/mol	61.9 kcal/mol	9
$P_3^{Si}Fe(NNMeH)^+$	$BDFE_{N-H}$	45.9 kcal/mol	44.9 kcal/mol	9

A1.9. References

[1] Grimme, S.; Antony, J.; Ehrlich, S.; Krieg, H. *J. Chem. Phys.* **2010**, *132*, 154104.

[2] Tao, J. M.; Perdew, J. P.; Staroverov, V. N.; Scuseria, G. E. *Phys. Rev. Lett.* **2003**, *91*, 146401.

[3] Weigend, F.; Ahlrichs, R. *Phys. Chem. Chem. Phys.* **2005**, *7*, 3297–3305.

[4] *John Towns, Timothy Cockerill, Maytal Dahan, Ian Foster, Kelly Gaither, Andrew Grimshaw, Victor Hazlewood, Scott Lathrop, Dave Lifka, Gregory D. Peterson, Ralph Roskies, J. Ray Scott, Nancy Wilkins-Diehr, "XSEDE: Accelerating Scientific Discovery", Computing in Science & Engineering, vol.16, no. 5, pp. 62-74, Sept.-Oct. 2014, doi:10.1109/MCSE.2014.80*

[5] (a) Valiev, M.; Bylaska, E. J.; Govind, N.; Kowalski, K.; Straatsma, T. P.; Van Dam, H. J. J.; Wang, D.; Nieplocha, J.; Apra, E.; Windus, T. L.; de Jong, W. A. *Comput. Phys. Commun.* **2010**, *181*, 1477–1489. (b) Neese, F. *Wiley interdisciplinary Reviews - Computational Molecular Science*, **2012**, *2:1*, 73-78.

[6] (a) Klamt, A.; Schüürmann, G. *J. Chem. Soc. Perkin Trans. 2.* **1993**, *2*, 799–805. (b)Marten, B.; Kim, K.; Cortis, C.; Friesner, R. A.; Murphy, R. B.; Ringnalda, M. N.; Sitkoff, D.; Honig, B. *J. Phys. Chem.* **1996**, *100*, 11775–11788.

[7] Warren, J. J.; Tronic, T. A.; Mayer, J. M. *Chem. Rev.* **2010**, *110*, 6961–7001.

[8] Lee, Y.; Mankad, N. P.; Peters, J. C. *Nature Chem.* **2010**, *2*, 558-565.

[9] Rittle, J.; Peters, J. C. *Angew. Chem. Int. Ed.* **2016**, *55*, 12262 –12265.

[10] Rittle, J.; Peters, J. C. *J. Am. Chem. Soc.* **2017**, *139*, 3161–3170.

[11] Creutz, S. E.; Peters, J. C. *J. Am. Chem. Soc.* **2014**, *136*, 1105−1115.

[12] Anderson, J. S.; Moret, M-. E.; Peters, J. C. *J. Am. Chem. Soc.* **2013**, *135*, 534−537.

[13] Marcus, R. A. *J. Chem. Phys.* **1956**, *24*, 966–978.

[14] (a) Iordanova, N.; Decornez, H.; Hammes-Schiffer, S. *J. Am. Chem. Soc.* **2001**, *123*, 3723-3733. (b) Roth, J. P.; Lovell, S.; Mayer, J. M. *J. Am. Chem. Soc.* **2000**, *122*, 5486-5498.

[15] Thompson, N. B.; Green, M. T.; Peters, J. C. *J. Am. Chem. Soc.* **2017**, *139*, 15312–15315.

Appendix 2. Supplementary Data for Chapter 3

A2.1. Experimental details

A2.1.1 General Considerations:

All manipulations were carried out using standard Schlenk or glovebox techniques under an N_2 atmosphere. Solvents were deoxygenated and dried by thoroughly sparging with N_2 followed by passage through an activated alumina column in a solvent purification system by SG Water, USA LLC. Non-halogenated solvents were tested with sodium benzophenone ketyl in tetrahydrofuran (THF) in order to confirm the absence of oxygen and water. Deuterated solvents were purchased from Cambridge Isotope Laboratories, Inc., degassed, and dried over activated 3-Å molecular sieves prior to use.

Cp^*_2Co,[1] $[P_3^BFe][BAr^F_4]$,[2] $P_3^{Si}FeN_2$,[3] $[P_3^BCoN_2][Na(12\text{-crown-}4)_2]$,[4] $P_3^{Si}CoN_2$,[5] $[P_3^BFeN_2][Na(12\text{-crown-}4)_2]$,[6] and $[Ph_2{}^{15}NH_2][OTf]$[7] were prepared according to literature procedures. $Ph^{15}NH_2$ was obtained from Sigma-Aldrich, Inc. degassed, and dried over activated 3-Å molecular sieves prior to use**.** All other reagents were purchased from commercial vendors and used without further purification unless otherwise stated. Diethyl ether (Et_2O) used in the experiments herein was stirred over Na/K ($\geq$ 2 hours) and filtered or vacuum-transferred before use unless otherwise stated.

A2.1.2 Physical Methods:

^1H chemical shifts are reported in ppm relative to tetramethylsilane, using ^1H resonances from residual solvent as internal standards. IR measurements were obtained as

solutions or thin films formed by evaporation of solutions using a Bruker Alpha Platinum ATR spectrometer with OPUS software (solution IR collected in a cell with KBr windows and a 1 mm pathlength). H_2 was quantified on an Agilent 7890A gas chromatograph (HP-PLOT U, 30 m, 0.32 mm ID; 30 °C isothermal; nitrogen carrier gas) using a thermal conductivity detector.

A2.1.3 Mössbauer Spectroscopy:

Mössbauer spectra were recorded on a spectrometer from SEE Co. (Edina, MN) operating in the constant acceleration mode in a transmission geometry. The sample was kept in an SVT-400 cryostat form Janis (Wilmington, MA). The quoted isomer shifts are relative to the centroid of the spectrum of a metallic foil of α-Fe at room temperature (RT). Solution samples were transferred to a sample cup and chilled to 77 K inside of the glovebox, and unless noted otherwise, quickly removed from the glovebox and immersed in liquid N_2 until mounted in the cryostat. Data analysis was performed using version 4 of the program WMOSS (www.wmoss.org) and quadrupole doublets were fit to Lorentzian lineshapes. See discussion below for detailed notes on the fitting procedure.

A2.1.4 Ammonia and Hydrazine Quantification:

Reaction mixtures are cooled to 77 K and allowed to freeze. The reaction vessel is then opened to atmosphere and to the frozen solution is slowly added an excess (with respect to acid) solution of a NaO^tBu solution in MeOH (0.25 mM) over 1-2 minutes. This

solution is allowed to freeze, then the headspace of the tube is evacuated and the tube is sealed. The tube is then allowed to warm to RT and stirred at RT for at least 10 minutes. An additional Schlenk tube is charged with HCl (3 mL of a 2.0 M solution in Et_2O, 6 mmol) to serve as a collection flask. The volatiles of the reaction mixture are vacuum transferred at RT into this collection flask. After completion of the vacuum transfer, the collection flask is sealed and warmed to RT. Solvent is removed in vacuo, and the remaining residue is dissolved in H_2O (1 mL). An aliquot of this solution (10–100 μL) is then analyzed for the presence of NH_3 (present as NH_4Cl) by the indophenol method.[8] A further aliquot of this solution is analyzed for the presence of N_2H_4 (present as N_2H_5Cl) by a standard colorimetric method.[9] Quantification is performed with UV−vis spectroscopy by analyzing absorbance at 635 nm. In this case of runs with $[PhNH_3][OTf]$ we found that aniline in the form of anilinium chloride was present in the receiving vessels. The anilinium chloride interfered with the indophenol and hydrazine detection method. Therefore, quantification for NH_3 was performed by extracting the solid residue into 1 mL of DMSO-d_6 that has 20 mmol of trimethoxybenzene as an internal standard. Integration of the ^1H NMR peak observed for NH_4 was then integrated against the two peaks of trimethoxybenzene to quantify the ammonium present. This ^1H NMR detection method was also used to differentiate $[^{14}NH_4][Cl]$ and $[^{15}NH_4][Cl]$ produced in the control reactions conducted with $[^{15}NPh_2H_2][OTf]$.

A2.1.5 EPR Spectroscopy

X-band EPR spectra were obtained on a Bruker EMX spectrometer. Samples were collected at powers ranging from 6-7 mW with modulation amplitudes of 2.00 G, modulation frequencies of 100.00 kHz, over a range of 2450 to 2900 Gauss. Spectra were baseline corrected using the algorithm in SpinCount.[10] EPR spectra were modeled using the easyspin program.[11]

A2.1.6 Computational Methods

All stationary point geometries were calculated using DFT with an M06-L functional,[12] a def2-TZVP[13] basis set on transition metals (Stuttgart ECP[14] was used on Mo atoms) and a def2-SVP[13] basis set on all other atoms. Calculations were performed, in part, using Xtreme Science and Engineering Discovery Environment (XSEDE) resources.[15] Calculations were performed on the full P_3^EFe scaffolds. Calculations on the [HIPTN_3N]Mo system were performed on a truncated scaffold in which the isopropyl groups were removed (i.e. [{3,5-$(C_6H_4)_2C_6H_3NCH_2CH_2\}_3N]^{3-}$). Geometries were optimized using the NWChem 6.5 package.[16] All single point energy, frequency and solvation energy calculations were performed with the Gaussian09 package.[17] Frequency calculations were used to confirm true minima and to determine gas phase free energy values (G_{gas}). Single point solvation calculations were done using an SMD solvation model with diethyl ether solvent and were used to determine solvated internal energy (E_{soln}). Free energies of solvation were approximated using the difference in gas phase internal energy

(E_{gas}) and solvated internal energy ($\Delta G_{solv} \approx E_{soln} - E_{gas}$) and the free energy of a species in solution was then calculated using the gas phase free energy (G_{gas}) and the free energy of solvation ($G_{soln} = G_{gas} + \Delta G_{solv}$).[18] All reduction potentials were calculated referenced to $Fc^{+/0}$ using the standard Nernst relation $\Delta G = -nFE^0$.

A2.2. Synthetic Details:

A2.2.1 General Procedure for the Synthesis of the Acids:

Prior to use the amine was purified (aniline by distillation, diphenylamine and triphenylamine by recrystallization). To a 250 mL round bottom flask in the glovebox was added the amine which was subsequently dissolved in 100 mL of Et_2O (no additional drying with NaK). To this was added dropwise (1 equiv) of HOTf with stirring over five minutes. Immediate precipitation of white solid was observed and the reaction mixture was allowed to stir for one hour at RT. The reaction mixture was then filtered and the resulting white powder was washed with Et_2O (50 mL), pentane (50 mL) and Et_2O again (50 mL). The resulting white microcrystalline material was then dried under vacuum. Yields of greater than 90% of microcrystalline material was obtained in this manner in all cases.

A2.3. Ammonia production and quantification studies

A2.3.1 Standard NH_3 Generation Reaction Procedure:

All solvents are stirred with Na/K for ≥2 hours and filtered prior to use. In a nitrogen-filled glovebox, the precatalyst (2.3 μmol) was weighed into a vial.* The

precatalyst was then transferred quantitatively into a Schlenk tube using THF. The THF was then evaporated to provide a thin film of precatalyst at the bottom of the Schlenk tube. The tube is then charged with a stir bar and the acid and reductant are added as solids. The tube is then cooled to 77 K in a cold well. To the cold tube is added Et_2O to produce a concentration of precatalyst of 2.3 mM. The temperature of the system is allowed to equilibrate for 5 minutes and then the tube is sealed with a Teflon screw-valve. This tube is passed out of the box into a liquid N_2 bath and transported to a fume hood. The tube is then transferred to a dry ice/acetone bath where it thaws and is allowed to stir at -78 °C for three hours. At this point the tube is allowed to warm to RT with stirring, and stirred at RT for 5 minutes. To ensure reproducibility, all experiments were conducted in 200 mL Schlenk tubes (51 mm OD) using 25 mm stir bars, and stirring was conducted at ~900 rpm.

* In cases where less than 2.3 μmol of precatalyst was used stock solutions were used to avoid having to weigh very small amounts.

Table A2.1: UV-vis quantification results for standard NH_3 generation experiments with $P_3^BFe^+$

Entry	$P_3^BFe^+$ (μmol)	Acid equiv	Cp^*_2Co equiv	NH_4Cl (μmol)	N_2H_5Cl (μmol)	Equiv NH_3/Fe	% Yield NH_3 Based on e^-
A	2.3	108[a]	54	31.4	0.0	13.5	75.6
B	2.3	108[a]	54	28.5	0.0	12.3	68.6
C	2.3	108[a]	54	29.2	0.0	12.6	70.4
Avg.						12.8 ± 0.5	72 ± 3
D	2.3	322[a]	162	76.4	2.0	33.0	61.4
E	2.3	322[a]	162	80.0	0.7	34.5	64.2

Avg.						34 ± 1	63 ± 2
F	2.3	638[a]	322	60.4	0.5	26.0	24.3
G	2.3	638[a]	322	63.2	0.3	27.3	25.4
Avg.						26.7 ± 0.9	25 ± 1
H	1.1	108[b]	54	7.8	0.0	6.9	37.6
I	2.3	108[b]	54	19.2	0.0	8.3	46.3
Avg.						8 ± 1	42 ± 6
J	2.3	108[c]	54	17.7	N.D.	7.7	43.1
K	2.3	108[c]	54	13.8	N.D.	6.0	33.6
Avg.						7 ± 1	38 ± 7
L	2.3	322[c]	162	39.8	N.D.	17.3	32.0
M	2.3	322[c]	162	31.9	N.D.	13.9	25.7
Avg.						16 ± 3	29 ± 4

N.D. indicates the value was not determined [a]Acid used is $[Ph_2NH_2][OTf]$ [b]Acid used is $[Ph_2NH_2][BAr^F{}_4]$ [c]Acid used is $[PhNH_3][OTf]$

Table A2.2: UV-vis quantification results for standard NH_3 generation experiments with $P_3{}^{Si}FeN_2$

Entry	$P_3{}^{Si}FeN_2$ (µmol)	Acid equiv	Cp^*_2Co equiv	NH_4Cl (µmol)	N_2H_5Cl (µmol)	Equiv NH_3/Fe	% Yield NH_3 Based on e^-
A	2.3	108[a]	54	6.6	0.0	1.7	9.3
B	2.3	108[a]	54	2.7	0.0	0.7	3.8
Avg.						1.2 ± 0.2	6.5 ± 0.3

[a]Acid used is $[Ph_2NH_2][OTf]$

Table A2.3: UV-vis quantification results for standard NH_3 generation experiments with $P_3{}^{B}CoN_2{}^-$

Entry	$P_3{}^{B}CoN_2{}^-$ (µmol)	Acid equiv	Cp^*_2Co equiv	NH_4Cl (µmol)	N_2H_5Cl (µmol)	Equiv NH_3/Fe	% Yield NH_3 Based on e^-
A	2.3	108[a]	54	3.0	0.0	1.3	7.2

B	2.3	108[a]	54	1.8	0.0	0.8	4.4
Avg.						1.1 ± 0.4	6 ± 2

[a]Acid used is $[Ph_2NH_2][OTf]$

Table A2.4: UV-vis quantification results for standard NH_3 generation experiments with $P_3^{Si}CoN_2$

Entry	$P_3^{Si}CoN_2$ (µmol)	Acid equiv	Cp^*_2Co equiv	NH_4Cl (µmol)	N_2H_5Cl (µmol)	Equiv NH_3/Fe	% Yield NH_3 Based on e^-
A	2.3	108[a]	54	0.0	0.0	0.0	0.0
B	2.3	108[a]	54	0.0	0.0	0.0	0.0
Avg.						0.0	0.0

[a]Acid used is $[Ph_2NH_2][OTf]$

A2.3.2 Ammonia production studies with $[Ph_2{}^{15}NH_2][OTf]$:

The procedure was the same as the general procedure presented in section 3.1 with 2.3 µmol of $P_3^BFe^+$ catalyst, 54 equiv Cp^*_2Co, and 108 equiv $[Ph_2{}^{15}NH_2][OTf]$. Product analyzed by ^1H NMR as described in section 1.4 and only the diagnostic triplet of $[^{14}NH_4][Cl]$ is observed.

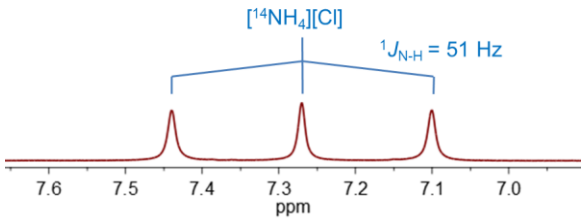

Figure A2.1: ^{1}H NMR spectrum (300 MHz, DMSO-d_6) of [$^{14}NH_4$][Cl] produced from catalytic N_2-to-NH_3 conversion conducted with $P_3{}^{B}Fe^{+}$ catalyst, 54 equiv Cp^*_2Co, and 108 equiv [$Ph_2{}^{15}NH_2$][OTf] under an atmosphere of $^{14}N_2$.

A2.4. NH_3 Generation Reaction with Periodic Substrate Reloading – Procedure with $P_3{}^{B}Fe^{+}$:

All solvents are stirred with Na/K for ≥2 hours and filtered prior to use. In a nitrogen-filled glovebox, the precatalyst (2.3 μmol) was weighed into a vial. The precatalyst was then transferred quantitatively into a Schlenk tube using THF. The THF was then evaporated to provide a thin film of precatalyst at the bottom of the Schlenk tube. The tube is then charged with a stir bar and the acid and reductant are added as solids. The tube is then cooled to 77 K in a cold well. To the cold tube is added 1 mL of Et_2O. The temperature of the system is allowed to equilibrate for 5 minutes and then the tube is sealed with a Teflon screw-valve. The cold well cooling bath is switched from a $N_{2(l)}$ bath to a dry ice/acetone bath. In the cold well the mixture in the sealed tube thaws with stirring and is allowed to stir at -78 °C for 3 hours. Then, without allowing the tube to warm above -78 °C, the cold well bath is switched from dry ice/acetone to $N_{2(l)}$. After fifteen minutes the reaction mixture is observed to have frozen, at this time the tube is opened. To the cold tube is added acid (324 equiv) and reductant (162 equiv) as solids. To the tube then 1 additional mL of Na/K-dried Et_2O is added. The cold well cooling bath is switched from a $N_{2(l)}$ bath to a dry ice/acetone bath. In the cold well the mixture in the sealed tube thaws with stirring and is allowed to stir at -78 °C for 3 hours. These reloading steps are repeated

the desired number of times. Then the tube is allowed to warm to RT with stirring, and stirred at RT for 5 minutes.

Table A2.5: UV-vis quantification results for NH_3 generation experiments with $P_3^BFe^+$, with reloading

	Number of Loadings	$P_3^BFe^+$ (µmol)	Acid equiv	Cp^*_2Co equiv	NH_4Cl (µmol)	N_2H_5Cl (µmol)	Equiv NH_3/Fe	% Yield Based on H^+
A	2	2.3	[322] x2[a]	[162]x2	115.0	0.1	49.6	46.2
B	2	2.3	[322] x2[a]	[162]x2	145.6	0.0	62.8	58.5
Avg.							56 ± 9	52 ± 9
C	3	2.3	[322] x3[a]	[162]x3	182.4	0.3	78.7	48.9
D	3	2.3	[322] x3[a]	[162]x3	207.3	0.1	89.5	55.5
Avg.							84 ± 8	52 ± 5

[a]Acid used is $[Ph_2NH_2][OTf]$

A2.5. Time-resolved H_2 quantification of background acid and Cp^*_2Co reactivity:

Inside of a nitrogen filled glovebox, solid acid (0.248 mmol) and Cp^*_2Co (0.124 mmol) are added to a 260 mL glass tube charged with a stir bar. The vessel is sealed with a septum at RT and subsequently chilled to -196 °C in a cold well in the nitrogen filled glovebox. Et_2O (1 mL) is added via syringe into the vessel and completely frozen. The vessel is passed out of the glovebox into a liquid N_2 bath, and subsequently thawed in a dry ice/acetone bath with stirring at ~900 rpm. The timer was started as soon as the vessel was

transferred to the dry ice/acetone bath. The headspace of the reaction vessel was periodically sampled with a sealable gas sampling syringe (10 mL), which was loaded into a gas chromatograph, and analyzed for the presence of $H_{2(g)}$. From these data, the percent H_2 evolved (relative to Cp^*_2Co) was calculated, correcting for the vapor pressure of Et_2O and the removed H_2 from previous samplings. Each time course was measured from a single reaction maintained at -78 °C.

Table A2.6: Time-resolved H_2 quantification for the reaction of Cp^*_2Co and acid in Et_2O at -78 °C in the absence of an Fe precatalyst

Acid	Time (min)	$H_{2(g)}$ (μmol)	% H_2 Based on Cp^*_2Co
$[Ph_2NH_2][OTf]^a$	10	1.0 ± 0.4	1.6 ± 0.6
	60	2.1 ± 0.6	3 ± 1
$[Ph_2NH_2][BAr^F{}_4]^b$	10	3.7 ± 0.1	6.0 ± 0.2
	60	12.7 ± 0.8	21 ± 1

[a]Average of two experiments [b]Average of three experiments

A2.6. Mössbauer Spectra:

A2.6.1 General Procedure for Preparation of Rapid-freeze-quench Mössbauer Samples of Catalytic Reaction Mixtures using $P_3{}^BFe^+$:

All manipulations are carried out inside of a nitrogen filled glovebox. The precatalyst, $[P_3{}^B(^{57}Fe)][BAr^F{}_4]$, is weighed into a vial (3.5 mg, 2.3 μmol) and transferred

using THF into a 150 mL Schlenk tube. The solvent is evaporated to form a thin film of the precatalyst and a stir bar is added. The $[Ph_2NH_2][OTf]$ (79.4 mg, 0.248 mmol) and Cp^*_2Co (40.3 mg, 0.124 mmol) are added to the Schlenk tube as solids. The Schlenk tube is then placed in $N_{2(l)}$ and the temperature is allowed to equilibrate. To the tube 1 mL of Et_2O is added. The tube is then sealed with a Teflon screw tap and transferred to a pre-chilled cold well at -78 °C. The timer is set to zero as soon as the stir bar is freed from the thawing solvent. At the desired time, the tube is opened and the well-stirred suspension is transferred to a Delrin cup pre-chilled to -78 °C using a similarly pre-chilled pipette. The sample in the Delrin cup is then rapidly frozen in $N_{2(l)}$. At this point the sample, immersed in $N_{2(l)}$, is taken outside of the glovebox and mounted in the cryostat.

A2.6.2 General Procedure for Preparation of Rapid-freeze-quench Mössbauer Samples of the Reaction of $P_3^BFe^+$ with Reductants:

All manipulations are carried out inside of a nitrogen filled glovebox. The precatalyst, $[P_3^B(^{57}Fe)][BAr^F_4]$, is weighed into a vial (3.5 mg, 2.3 μmol) and .5 mL of THF is added. The solvent is then evaporated to provide a thin film of $[P_3^B(^{57}Fe)][BAr^F_4]$. To this is added the desired reductant as a solid (46.0 μmol, 20 equiv). This vial is then placed in $N_{2(l)}$ and the temperature is allowed to equilibrate. To this is added 1 mL of NaK-dried Et_2O. The vial is then sealed with a cap and transferred to a pre-chilled cold well at -78 °C. The timer is set to zero as soon as the stir bar is freed from the thawing solvent. After five minutes using a pre-chilled pipette the well-stirred reaction mixture is transferred to a

Delrin cup that has been pre-chilled to -78 °C. The sample in the Delrin cup is then rapidly frozen in $N_{2(l)}$. At this point the sample, immersed in $N_{2(l)}$, is taken outside of the glovebox and mounted in the cryostat.

A2.6.3 General Procedure for Fitting of Rapid-freeze-quench Mössbauer Samples: Data analysis was performed using version 4 of the program WMOSS (www.wmoss.org) and quadrupole doublets were fit to Lorentzian lineshapes. Simulations were constructed from the minimum number of quadrupole doublets required to attain a quality fit to the data (convergence of χ_R^2). Quadrupole doublets were constrained to be symmetric, unless $[P_3^BFe–N_2][Na(12\text{-crown-}4)_2]$ was included in the model. With $[P_3^BFe–N_2][Na(12\text{-crown-}4)_2]$ since it is known to have characteristic asymmetry we started with the observed linewidths in the authentic sample and allowed them to then relax. It is known that the exact linewidths are sensitive to the particular sample but the relative line breadth should be fairly constant. Using the non-linear error analysis algorithm provided by WMOSS, the errors in the computed parameters are estimated to be 0.02 mm s^{-1} for δ and 2% for Δ_{Eq}.

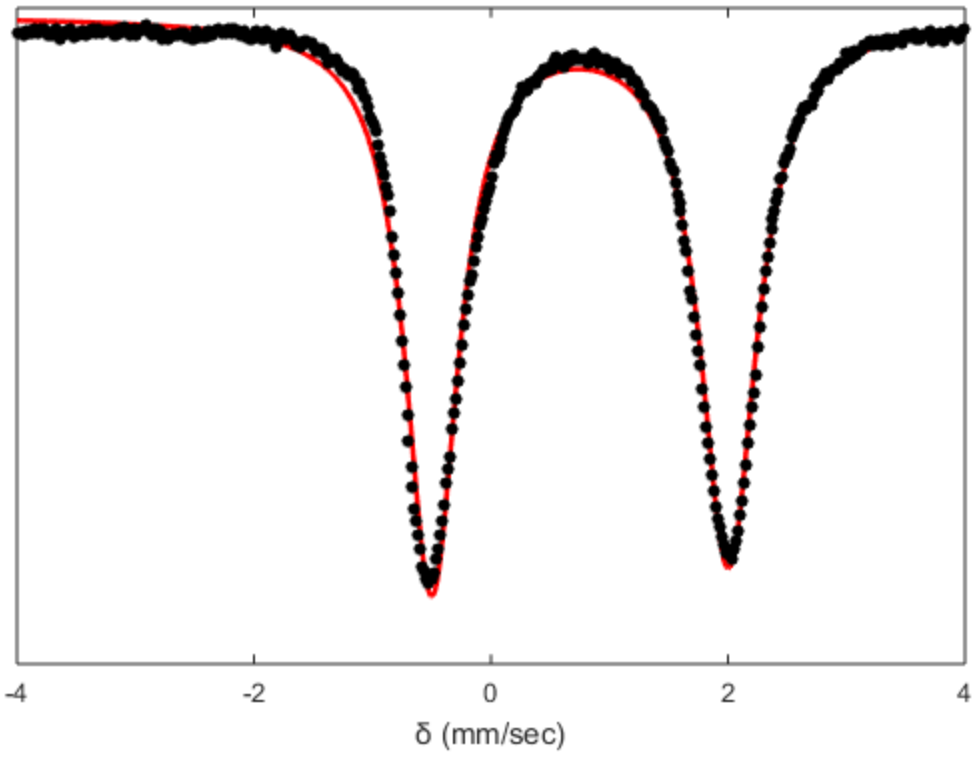

Figure A2.2: Mössbauer spectrum collected on $P_3^B(^{57}Fe)^+$ that was used for the Mössbauer experiments conducted in this paper. The parameters used to model this species are extremely similar to those used previously to model this species (δ = 0.75 mm/sec, Δ_{Eq} = 2.55 mm/sec, $\Gamma_r = \Gamma_l$ = 0.52 mm/sec).

Table A2.7. Fit parameters for $P_3^BFe^+$.[18 19]

Component	δ (mm s^{-1})	ΔE_Q (mm s^{-1})	Linewidths, Γ_L/Γ_R (mm s^{-1})
Fit	0.75 ± 0.02	2.50 ± 0.05	0.54/0.58

A2.6.4. Details of Individual RFQ Mossbauer spectra:

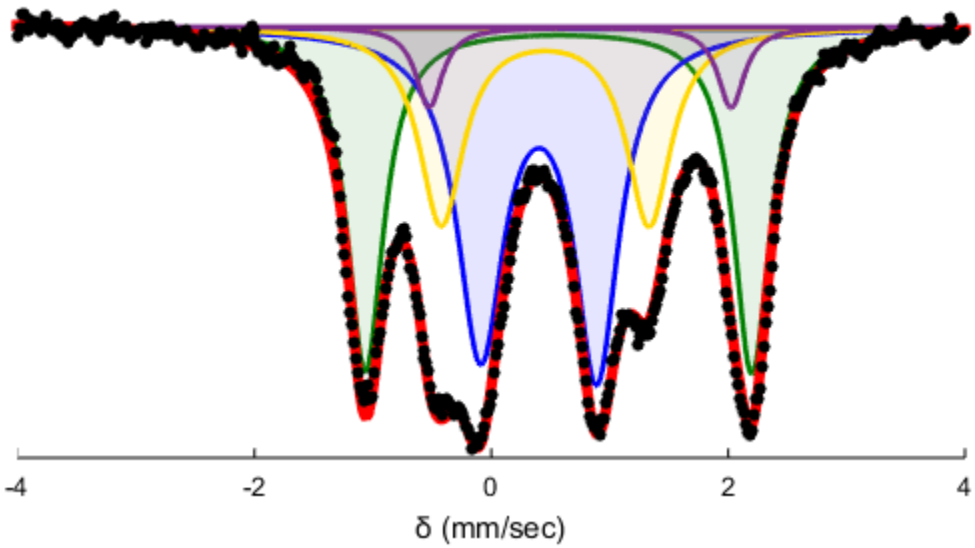

Figure A2.3. Mössbauer spectrum collected from a reaction quenched after 5 minutes between $P_3^BFe^+$ and excess Cp^*_2Co (20 equiv). Raw data shown as black points, simulation as a solid red line, with components in green, blue, yellow, and purple (see Table S for parameters). Collected at 80 K with a parallel applied magnetic field of 50 mT as a suspension in Et_2O.

Fitting details for Figure A2.3: Four quadrupole doublets were found to be necessary to obtain an adequate simulation. The simulation parameters are given in Table S6.2. The two major species in this spectrum are well simulated as $P_3^BFe–N_2$ and $P_3^BFe–N_2^-$. The residual signal exhibits only two well resolved absorbances but to obtain a good fit with symmetric lineshapes two additional quadrupole doublets were necessary. One of these can be identified as $[P_3^BFe]^+$ based on the asymmetry in the lineshape of the right feature of $P_3^BFe–N_2$. The similarity of the other two quadrupole doublets to those identified in the five-

minute freeze quench make this a logically consistent fit but one that is not strictly required by the data.

Table A2.8. Fit Parameters for Figure A2.3.

Component	δ (mm s^{-1})	ΔE_Q (mm s^{-1})	Linewidths, Γ_L/ Γ_R (mm s^{-1})	Relative area
A (green)	0.57 ± 0.02	3.26 ± 0.06	0.29/0.29	0.33
B (purple)	0.75 ± 0.02	2.55 ± 0.05	0.27/0.27	0.06
C (yellow)	0.45 ± 0.02	1.76 ± 0.04	0.45/0.45	0.23
D (blue)	0.40 ± 0.02	0.98 ± 0.02	0.48/0.45	0.39

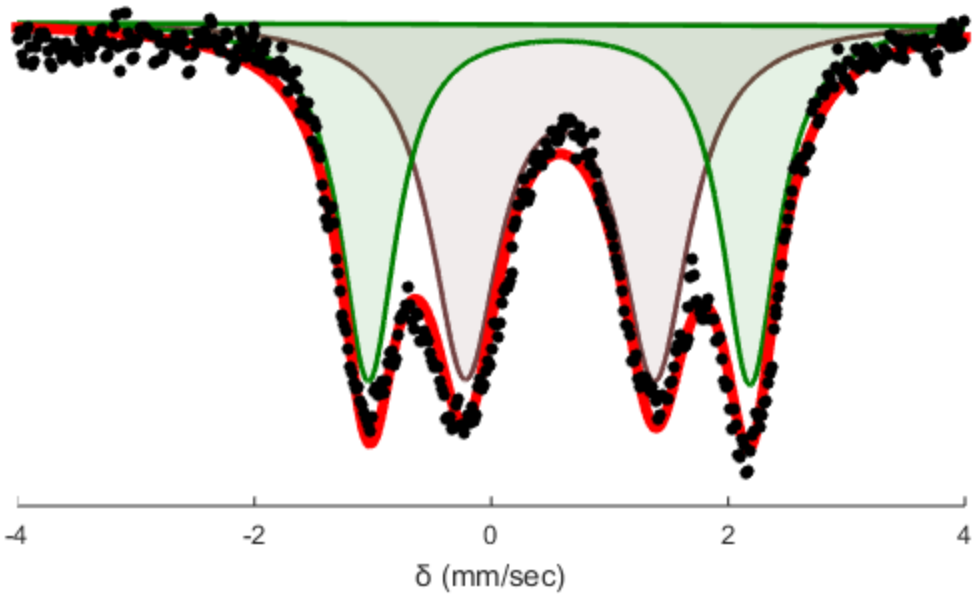

Figure A2.4. Mössbauer spectrum collected from a reaction quenched after 5 minutes between $P_3^BFe^+$ and excess Cp^*_2Cr (20 equiv). Raw data shown as black points, simulation as a solid red line, with components in green and (see Table S for parameters). Collected at 80 K with a parallel applied magnetic field of 50 mT as a suspension in Et_2O.

Fitting details for Figure A2.4. The two well-resolved quadrupole doublets can be simulated. The simulation parameters are given in Table S6.3. One of the two major species in this spectrum is well simulated as $P_3^BFe–N_2$. The other feature has a very similar isomer shift but a significantly narrower quadrupole splitting. Given the labile nature of the N_2 ligand this other species may represent a vacant neutral species or a dimeric N_2 bridged species.

Table A2.9. Fit Parameters for Figure A2.4.

Component	δ (mm s^{-1})	ΔE_Q (mm s^{-1})	Linewidths, Γ_L/ Γ_R (mm s^{-1})	Relative area
A (green)	0.57 ± 0.02	3.22 ± 0.06	0.29/0.29	0.46
B (brown)	0.58 ± 0.02	1.60 ± 0.05	0.71/0.71	0.54

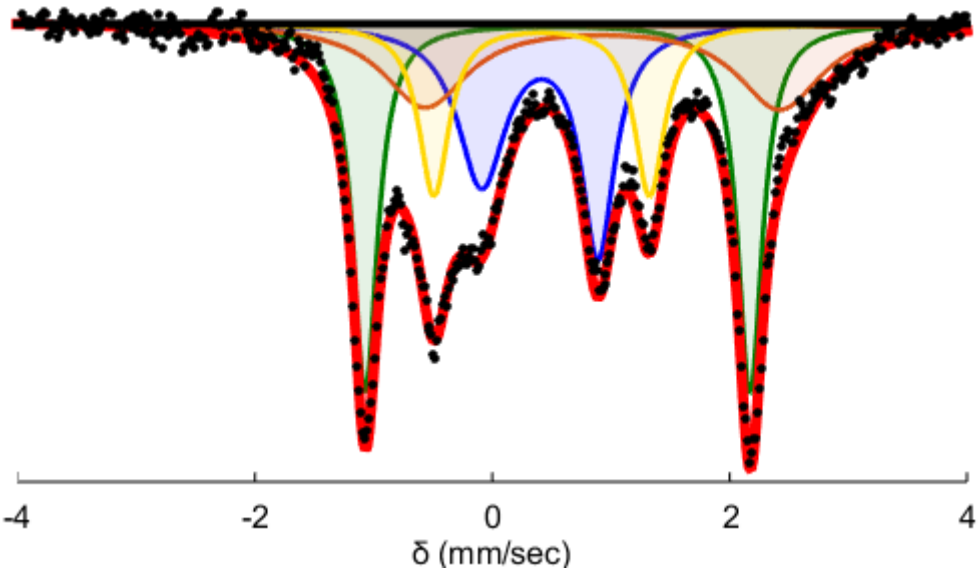

Figure A2.5. Mossbauer spectrum collected from a catalytic reaction quenched after 5 minutes. Conditions: $[P_3^B(^{57}Fe)][BArF]$ = 0.23 mM, $[Ph_2NH_2][OTf]$ = 24.8 mM (108 equiv), and Cp^*_2Co 12.4 mM (54 equiv). Raw data shown as black points, simulation as a solid red line, with components in green, blue, yellow, and orange (see Table S for parameters). Collected at 80 K with a parallel applied magnetic field of 50 mT.

Fitting details for Figure A2.5. Four pairs of quadrupole doublets were found to be necessary to obtain an adequate simulation of these data. The simulation parameters are given in Table S6.1. The outer pair of sharp features clearly belong to $P_3{}^BFeN_2$. The inner feature is highly suggestive of $P_3{}^BFeN_2{}^-$ the presence of which was confirmed by freeze-quench EPR. The residual then consists of two sharp features which were simulated with the quadrupole doublet in yellow and a broader residual feature that is captured by the quadrupole doublet in orange. The exact isomer shift and quadrupole splitting of orange is not determined by this model but the one here is representative.

Table A2.10. Simulation parameters for Mossbauer spectrum in Figure A2.6.4.

Component	**δ (mm s^{-1})**	**ΔE_Q (mm s^{-1})**	**Linewidths, Γ_L/ Γ_R (mm s^{-1})**	**Relative area**
A (green)	0.55 ± 0.02	3.24 ± 0.06	0.25/0.25	0.32
B (blue)	0.40 ± 0.02	0.98 ± 0.02	0.49/0.34	0.26
C (yellow)	0.42 ± 0.02	1.82 ± 0.04	0.31/0.31	0.18
D (orange)	0.93 ± 0.02	2.99 ± 0.06	0.87/0.87	0.24

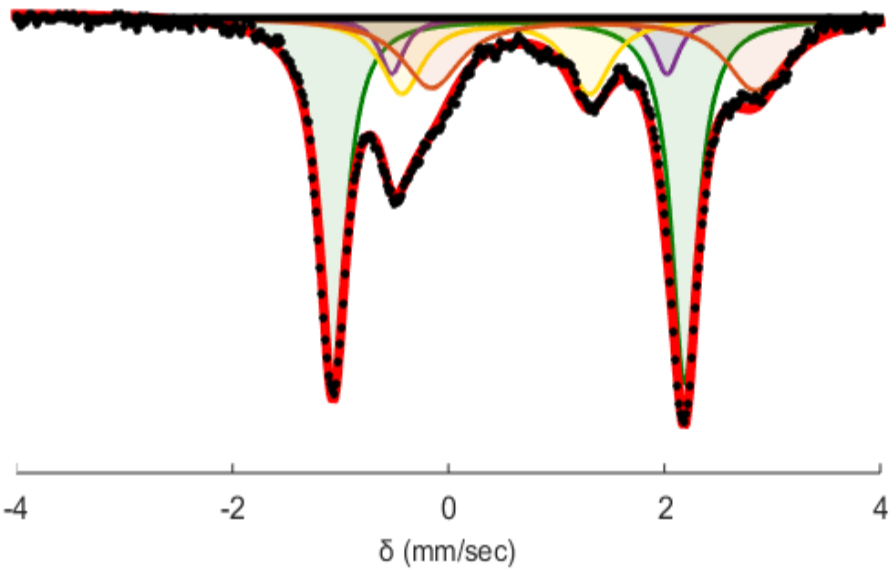

Figure A2.6. Mössbauer spectrum collected from a catalytic reaction quenched after 30 minutes. Conditions: $[P_3^B(^{57}Fe)][BArF]$ = 0.23 mM, $[Ph_2NH_2][OTf]$ = 24.8 mM (108 equiv), and Cp^*_2Co 12.4 mM (54 equiv). Raw data shown as black points, simulation as a solid red line, with components in green, purple, yellow, and orange (see Table A2.6.5 for parameters). Collected at 80 K with a parallel applied magnetic field of 50 mT.

Fitting details for Figure A2.6. Four quadrupole doublets were found to be necessary to obtain an adequate simulation. The simulation parameters are given in Table A2.11. The major species in this spectrum is again well simulated as $P_3^BFe–N_2$. The residual signal exhibits only three well resolved absorbances but to obtain a good fit with symmetric lineshapes three additional quadrupole doublets were necessary. One of these can be identified as $[P_3^BFe]^+$ based on the asymmetry in the lineshape of the right feature of $P_3^BFe–N_2$. The similarity of the other two quadrupole doublets to those identified in the five-

minute freeze quench make this a logically consistent fit but one that is not strictly required by the data.

Table A2.11. Simulation parameters for Mossbauer spectrum in Figure A2.6.

Component	δ (mm s^{-1})	ΔE_Q (mm s^{-1})	Linewidths, Γ_L/Γ_R (mm s^{-1})	Relative area
A (green)	0.55 ± 0.02	3.24 ± 0.06	0.29/0.29	0.53
B (purple)	0.75 ± 0.02	2.55 ± 0.05	0.27/0.27	0.08
C (yellow)	0.44 ± 0.02	1.74 ± 0.04	0.48/0.48	0.18
D (orange)	1.35 ± 0.02	3.00 ± 0.06	0.67/0.67	0.22

A2.7. EPR Spectra:

A2.7.1 General Procedure for Preparation of Rapid-freeze-quench EPR Samples of Catalytic Reaction Mixtures using $P_3^BFe^+$:

All manipulations are carried out inside of a nitrogen filled glovebox. The precatalyst, $[P_3^BFe][BAr^F_4]$, is weighed into a vial (3.5 mg, 2.3 μmol) and transferred using THF into a 150 mL Schlenk tube. The solvent is evaporated to form a thin film of the precatalyst and a stir bar is added. The $[Ph_2NH_2][OTf]$ (79.4 mg, 0.248 mmol) and Cp^*_2Co (40.3 mg, 0.124 mmol) are added to the Schlenk tube as solids. The Schlenk tube is then placed in $N_{2(l)}$ and the temperature is allowed to equilibrate. To the tube 1 mL of Et_2O is

added. The tube is then sealed with a Teflon screw tap and transferred to a pre-chilled cold well at -78 °C. The timer is set to zero as soon as the stir bar is freed from the thawing solvent. At the desired time, the tube is opened and the well-stirred suspension is transferred to an EPR tube that is prechilled to -78 °C using a pipette that has similarly been pre-chilled to -78 °C. The EPR sample is then rapidly frozen in $N_{2(l)}$. At this point the sample is quickly transferred out of the glovebox and put into $N_{2(l)}$ before it can warm.

A2.7.2 General Procedure for Preparation of Rapid-freeze-quench EPR Samples of the Reaction of $P_3^BFe^+$ with Reductants:

All manipulations are carried out inside of a nitrogen filled glovebox. The precatalyst, $[P_3^BFe][BAr^F{}_4]$, is weighed into a vial (3.5 mg, 2.3 μmol) and .5 mL of THF is added. The solvent is then evaporated to provide a thin film of $[P_3^BFe][BAr^F{}_4]$. To this is added (46.0 μmol, 20 equiv) of the desired reductant as a solid. This vial is then placed in $N_{2(l)}$ and the temperature is allowed to equilibrate. To this is added 1 mL of NaK-dried Et_2O. The vial is then sealed with a cap and transferred to a pre-chilled cold well at -78 °C. The timer is set to zero as soon as the stir bar is freed from the thawing solvent. At the desired time, the tube is opened and the well-stirred suspension is transferred to an EPR tube that is prechilled to -78 °C using a pipette that has similarly been pre-chilled to -78 °C. The EPR sample is then rapidly frozen in $N_{2(l)}$. At this point the sample is quickly transferred out of the glovebox and put into $N_{2(l)}$ before it can warm.

A2.7.3 General Procedure for Preparation of EPR Samples of Cp^*_2Co, $[P_3^BFe][BAr^F_4]$, and $[P_3^BFeN_2][Na(12\text{-crown-}4)_2]$:

The desired species was dissolved in 1 mL of Et_2O at RT and transferred to an EPR tube. The EPR tube was then chilled to -78 °C for five minutes. It was then rapidly frozen by transfer to a bath of $N_{2(l)}$.

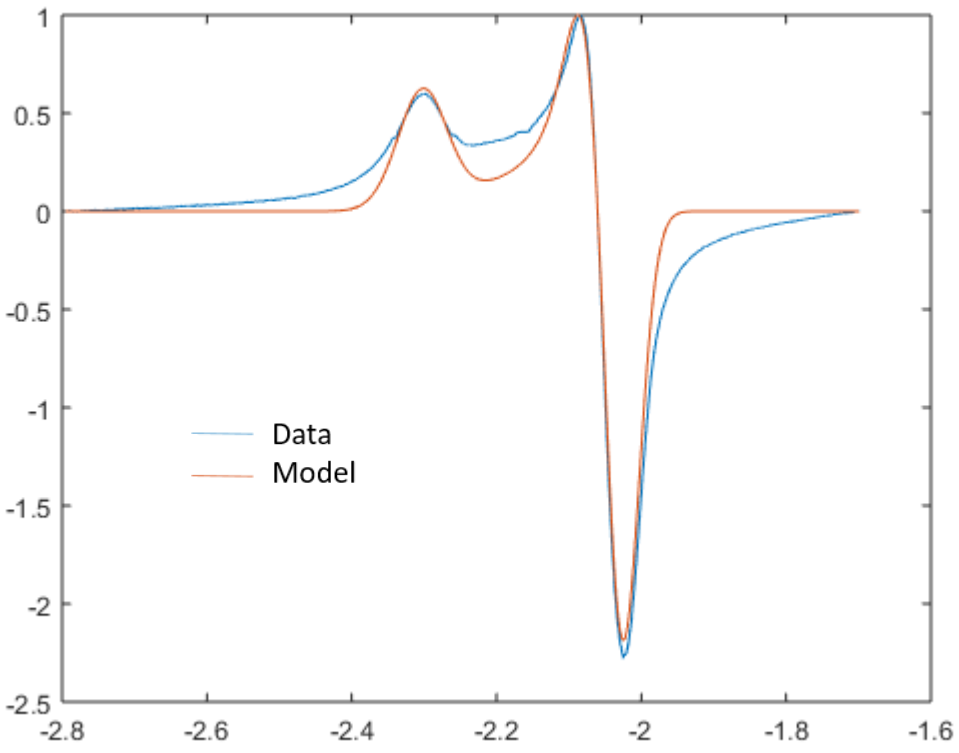

Figure A2.7. The X-band EPR spectrum in a 2-MeTHF glass of 2.3 mM $[P_3^BFe–N_2][Na(12\text{-crown-}4)_2]$ at 77K. Note that the exceeding insolubility of these species when encapsulated in a crown salt prevented its measurement in ether. We note that this species has significantly different parameters than the species in which the Na is not encapusalated

with a crown ether and is therefore interacting with the N_2 ligand. We think this species is more representative of what a hypothetical $[P_3^BFe–N_2][Cp^*_2Co]$ species would look like if isolated.

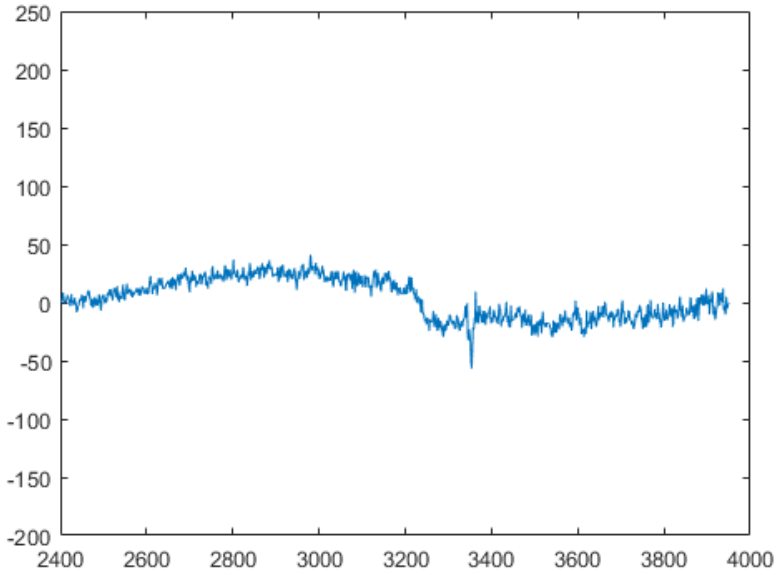

Figure A2.8. The X-band EPR spectrum in Et_2O of 2.3 mM $[P_3^BFe][BAr^F_4]$ at 77K. Note this species is S = 3/2 and as such we would expect no EPR signal at this temperature as is

observed here. We attribute the extremely weak signal observed here to background signal from the cavity

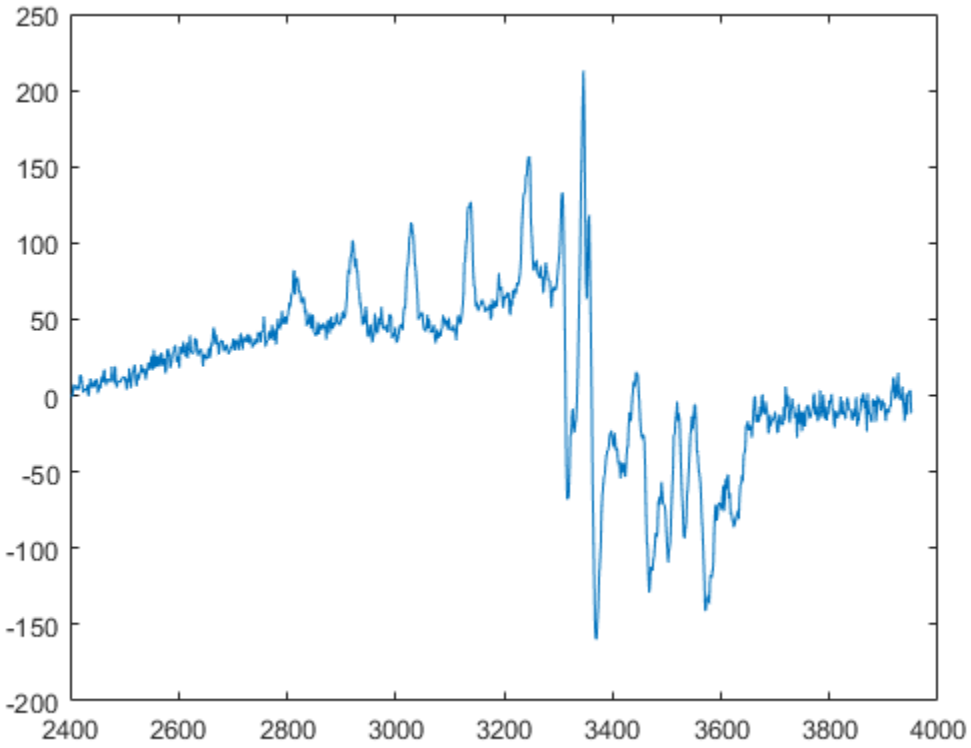

Figure A2.9. The X-band EPR spectrum in Et_2O of 46 mM Cp^*_2Co at 77K. Decamethylcobaltocene is known to be EPR silent at 77 K but at these high concentrations it becomes apparent that there is a small S = ½ impurity present in this spectrum. This persistent impurity is observable in both freeze quenched reactions of this reductant with $[P_3^BFe][BAr^F_4]$ and in spectra of the freeze quenched catalytic reaction mixtures.

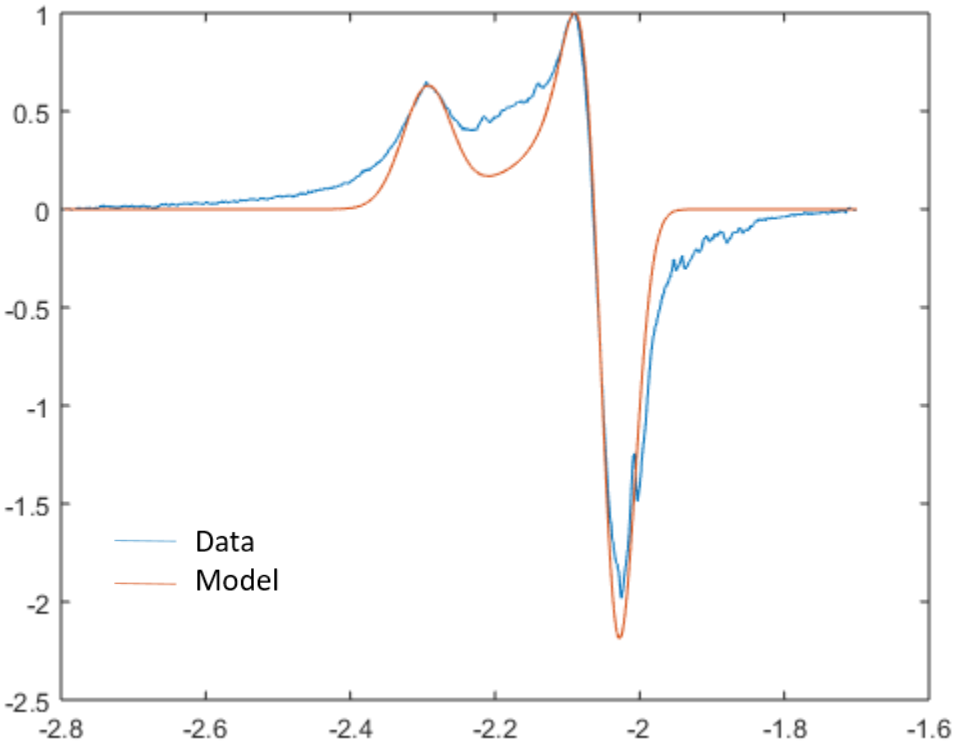

Figure A2.10. The X-band EPR spectrum in Et_2O (1 mL) of the reaction between $P_3{}^BFe^+$ (3.5 mg, 0.0023 mmol) and Cp^*_2Co (15.2 mg, 0.046 mmol) stirred for 5 minutes at -78 °C then rapidly frozen to 77 K.

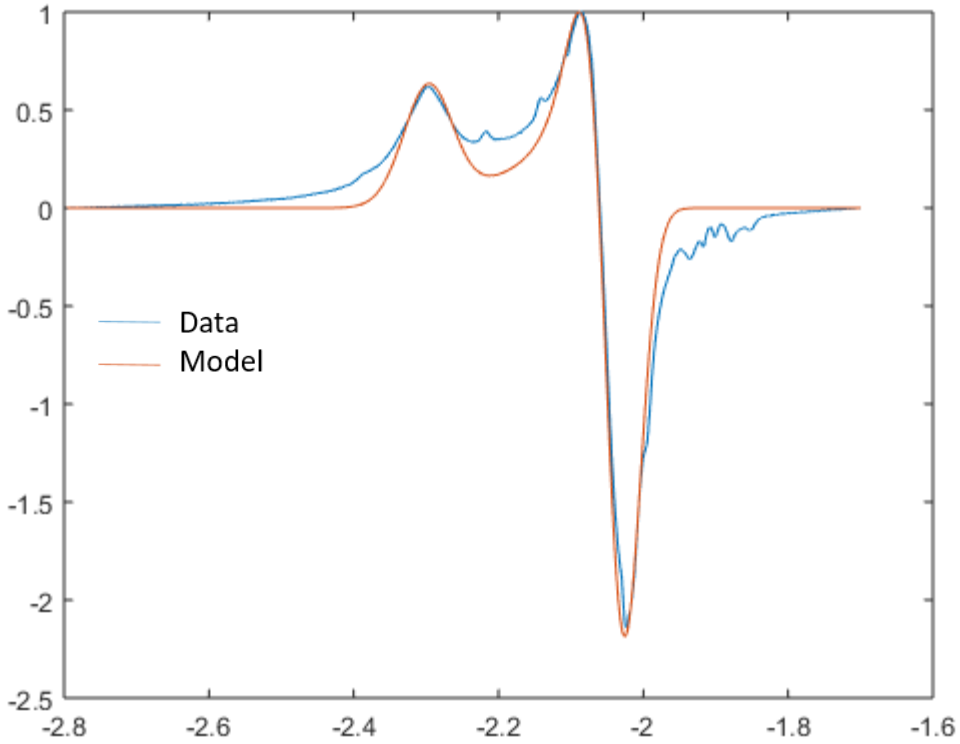

Figure A2.11. The X-band EPR spectrum in Et_2O (1 mL) of the reaction between $P_3{}^BFe^+$ (3.5 mg, 0.0023 mmol) and Cp^*_2Co (40.3 mg, 0.124 mmol) and $[Ph_2NH_2][OTf]$ (79.4 mg, 0.248 mmol) stirred for 5 minutes at -78 °C then rapidly frozen to 77 K.

Table A2.12. A comparison of the best fitting parameters for the authentic sample of $P_3{}^BFeN_2^-$ (A), the freeze quench of the reaction with the reductant (B), the freeze quench of the catalytic reaction mixture (C).

Reaction	g_x	g_y	g_z
A	2.304	2.048	2.032
B	2.295	2.048	2.032
C	2.298	2.048	2.032

A2.8. Details on DFT Estimates of p*K*a and BDE

A2.8.1 Computational Estimates of p*K*a in Et2O:

The pK_a values in diethyl ether were calculated referenced to $H(OEt_2)_2^+$ and were predicted on the basis of the free-energy change of the exchange reaction with $H(OEt_2)_2^+$ and application of Hess' law on the closed chemical cycle. The pK_a of $H(OEt_2)_2^+$ was defined as 0.0.

A2.8.2 Computational Estimates of BDEs:

Bond dissociation enthalpies (BDE) of X–H bonds were calculated in the gas-phase using a series of known reference compounds containing M–OH, M–H and M–NH bonds.[20] The enthalpy difference between the H-atom donor/acceptor pair was calculated based on the thermochemical information provided by frequency calculations after structure optimizations using the procedure described in the general computational section. A linear plot of ΔH *vs* BDE_{lit} was generated to form a calibration curve (**Figure A2.8.1**). BDE predictions were generated by application of the line of best fit to the calculated ΔH of the unknown species. Error were calculated by application of the trend line to the calculated enthalpies of known species and comparison to their literature BDE value.[20-22] Errors are reported as the average of BDE_{calc}-BDE_{lit} (mean signed error, MSE) and the average of the absolute values of BDE_{calc}-BDE_{lit} (mean unsigned error, MUE). The use of

the Bordwell equation for bond dissociation enthalpies is well supported by small ΔS_{calc} = $S(X^{\bullet}) - S(XH)$, as shown in Table A2.14.

Table A2.13. Calculated ΔH values and literature BDE values used for BDE calibration

Species	ΔH_{calc}	BDE_{lit}	BDE_{calc}	Notes
$Cr(H_2O)_5(OH)^{2+}$	97.735	89	90	ref 20
$Fe(H_2O)_6^{2+}$	77.985	77	75	ref 20
$Cr(H_2O)_5(OOH)^{2+}$	77.175	79	75	ref 20
$bimFeN_2^{2+}$	69.255	67	68	ref 20
$P_3^{Si}Fe\text{-}C{=}NH^{+}$	65.905	65	66	ref 21
$bipFeH_2^{2+}$	65.475	62	65	ref 20
$TrenFeOH^{2-}$	64.105	66	64	ref 20
$CpFe(CO)_2H$	57.455	56	59	ref 20
$[HIPTN_3N]Mo\text{-}N{=}NH$	47.715	49	51	Truncated; ref 22
$P_3^{Si}Fe\text{-}N{=}NMeH^{+}$	43.915	48	48	ref 21
$P_3^{Si}Fe\text{-}C{=}NH$	38.915	44	44	ref 21
$P_3^{Si}Fe\text{-}C{=}NMeH$	34.375	45	40	ref 21
$P_3^{Si}Fe\text{-}C{=}NMeH^{+}$	32.955	44	39	ref 21
			MSE	-0.9
			MUE	2.1

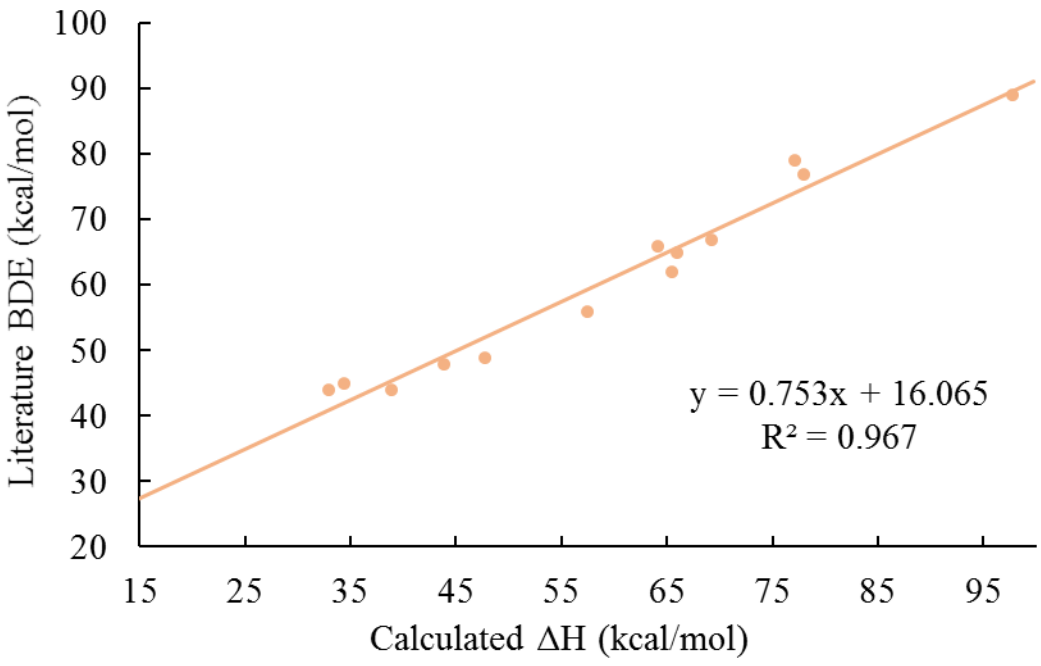

Table A2.14: Calculated entropy (S) for selected XH and X● species.

Species	S(X•) (cal/mol*K)	S(XH) (cal/mol*K)	ΔS (kcal/mol*K)
P_3^BFe-N=NH	271.6	268.9	$2.7x10^{-3}$
P_3^BFe=N-NH_2^+	266.3	273.1	$-6.8x10^{-3}$
P_3^BFe=N-NH_2	268.9	281.3	$-1.2x10^{-2}$
Cp*Co(η^4-C_5Me_5H)$^+$	168.8	162.0	$6.6x10^{-3}$
Cp*Cr(η^4-C_5Me_5H)$^+$	159.5	163.4	$-3.9x10^{-3}$

A2.9. References

[1] Robbins, J. L.; Edelstein, N.; Spencer, B.; Smart, J. C. *J. Am. Chem. Soc.* **1982**, *104*, 1882.

[2] Anderson, J. S.; Moret, M. E.; Peters, J. C. *J. Am. Chem. Soc.* **2013**, *135*, 534.

[3] Mankad, N. P.; Whited, M. T.; Peters, J. C. *Angew. Chem. Int. Ed.* **2007**, *46*, 5768.

[4] Del Castillo, T. J.; Thompson, N. B.; Suess, D. L.; Ung, G.; Peters, J. C. *Inorg. Chem.* **2015**, *54*, 9256.

[5] Suess, D. L.; Tsay, C.; Peters, J. C. *J. Amer. Chem. Soc.* **2012**, *134*, 14158.

[6] Moret, M.-E.; Peters, J. C. *Angew. Chem. Int. Ed.* **2011**, *50*, 2063.

[7] (a) Melzer, M. M.; Mossin, S.; Dai, X.; Bartell, A. M.; Kapoor, P.; Meyer, K.; Warren, T. H. *Angew. Chem. Int. Ed.* **2010**, *49*, 904. (b) Vicente, J.; Chicote, M. T.; Guerrero, R.; Jones, P. G. *J. Chem. Soc., Dalton Trans.* **1995**, *8*, 1251.

[8] Weatherburn, M. W. *Anal. Chem.* **1967**, *39*, 971.

[9] Watt, G. W.; Chrisp, J. D. *Anal. Chem.* **1952**, *24*, 2006.

[10] The Spin Count program developed by the Hendrich group at Carnegie Mellon was used to convert them to the g-value and then baseline them.

[11] Stoll, S.; Schweiger, A. *J. Magn. Reson.* **2006**, *178*, 42.

[12] Zhao, Y; Truhlar, D.G. *J. Chem. Phys.* **2006**, *125*, 1.

[13] (a) Weigend F.; Ahlrichs,R. *Phys. Chem. Chem. Phys*., **2005**, *7*, 3297. (b) Weigend F. *Phys. Chem. Chem. Phys.*, **2006**, *8*, 1057.

[14] Andrae D.; Haeussermann, U.; Dolg, M.; Stoll, H.; Preuss, H. *Theor. Chim. Acta*, **1990**, *77*, 123.

[15] *John Towns, Timothy Cockerill, Maytal Dahan, Ian Foster, Kelly Gaither, Andrew Grimshaw, Victor Hazlewood, Scott Lathrop, Dave Lifka, Gregory D. Peterson, Ralph Roskies, J. Ray Scott, Nancy Wilkins-Diehr, "XSEDE: Accelerating Scientific Discovery", Computing in Science & Engineering, vol.16, no. 5, pp. 62-74, Sept.-Oct. 2014, doi:10.1109/MCSE.2014.80*

[16] Valiev, M.; Bylaska, E.J.; Govind, N; Kowalski, K; Straatsma, T.P.; van Dam, H. J. J.; Wang, D.; Nieplocha, J.; Apra, E.; Windus, T. L.; de Jong, W. A. *Comput. Phys. Commun*. **2010**, *181*, 1477.

[17] Gaussian 09, Revision **B.01**, Frisch, M. J.; Trucks, G. W.; Schlegel, H. B.; Scuseria, G. E.; Robb, M. A.; Cheeseman, J. R.; Scalmani, G.; Barone, V.; Mennucci, B.; Petersson, G. A.; Nakatsuji, H.; Caricato, M.; Li, X.; Hratchian, H. P.; Izmaylov, A. F.; Bloino, J.; Zheng, G.; Sonnenberg, J. L.; Hada, M.; Ehara, M.; Toyota, K.; Fukuda, R.; Hasegawa, J.; Ishida, M.; Nakajima, T.; Honda, Y.; Kitao, O.; Nakai, H.; Vreven, T.; Montgomery, J. A., Jr.; Peralta, J. E.; Ogliaro, F.; Bearpark, M.; Heyd, J. J.; Brothers, E.; Kudin, K. N.; Staroverov, V. N.; Kobayashi, R.; Normand, J.; Raghavachari, K.; Rendell, A.; Burant, J. C.; Iyengar, S. S.; Tomasi, J.; Cossi, M.; Rega, N.; Millam, J. M.; Klene, M.; Knox, J. E.; Cross, J. B.; Bakken,V.; Adamo, C.; Jaramillo, J.; Gomperts, R.; Stratmann, R. E.; Yazyev, O.; Austin, A. J.; Cammi, R.; Pomelli, C.; Ochterski, J. W.; Martin, R. L.; Morokuma, K.; Zakrzewski, V. G.; Voth, G. A.; Salvador, P.; Dannenberg, J. J.; Dapprich, S.; Daniels, A. D.; Farkas, Ö.; Foresman, J. B.; Ortiz, J. V.; Cioslowski, J.; Fox, D. J. Gaussian, Inc., Wallingford CT, 2009.

[18] (a) Ribeiro, R.F.; Marenich, A.V.; Cramer, C.J.; Truhlar, D.G. *J. Phys. Chem. B.* **2011,** *115*, 14556. (b) Wang, T.; Brudvig, G; Batista, V.S. *J. Chem. Theory Comput.* **2010**, *6*, 755. (c) Marten, B.; Kyungsun, K.; Cortis, C.; Friesner, R.A.; Murphy, R.B.; Ringnalda, M.N.; Sitkoff, D.; Honig, B. *J. Phys. Chem.* **1996**, *100*, 11775.

[19] Anderson, J. S.; Cutsail 3rd, G. E.; Rittle, J.; Connor, B. A.; Gunderson, W. A.; Zhang, L.; Hoffman, B. M.; Peters, J. C. *J. Amer. Chem. Soc.* **2015**, *137*, 7803.

[20] Warren, J. J.; Tronic, T. A.; Mayer, J. M. *Chem. Rev.* **2010**, *110*, 6961.

[21] Rittle, J.; Peters, J. C. *Submitted Manuscript.*

[22] Yandulov, D. V.; Schrock, R.R. *Inorg. Chem.* **2005**, *44*, 1103.

Appendix 3. Supplementary Information for Chapter 4

A3.1.Experimental Details

A3.1.1. General Considerations

All manipulations were carried out using standard Schlenk or glovebox techniques under an N_2 atmosphere. Solvents were deoxygenated and dried by thoroughly sparging with N_2 followed by passage through an activated alumina column in a solvent purification system by SG Water, USA LLC. Non-halogenated solvents were tested with sodium benzophenone ketyl in tetrahydrofuran (THF) in order to confirm the absence of oxygen and water. Deuterated solvents were purchased from Cambridge Isotope Laboratories, Inc., degassed, and dried over activated 3-Å molecular sieves prior to use.

Cp^*_2Co,[1] $[P_3^BFe][BAr^F_4]$,[2] $[P_3^BFeN_2][Na(Et_2O)_3]$,[3] $[P_3^BFeN_2][Na(12\text{-crown-}4)_2]$,[3] $[H(OEt2)][BAr^F_4]$ ($HBAr^F_4$; $BArF_4$ = tetrakis- (3,5-bis(trifluoromethyl)phenyl)borate)[4],

$NaBAr^{F}{}_{4}{}^{4}$, and $[Cp^{*}{}_{2}Co][BAr^{F}{}_{4}]$ were prepared according to literature procedures. All other reagents were purchased from commercial vendors and used without further purification unless otherwise stated. Diethyl ether (Et_2O) used in the experiments herein was stirred over Na/K ($\geq$ 2 hours) and filtered through celite before use.

A3.1.2. Gas Chromatography

H_2 was quantified on an Agilent 7890A gas chromatograph (HP-PLOT U, 30 m, 0.32 mm ID; 30 °C isothermal; nitrogen carrier gas) using a thermal conductivity detector. A 10 mL manual injection was used and integration area was converted to percent H_2 composition by use of a calibration obtained from injection of H_2 solutions in N_2 of known concentration.

A3.1.3. Mössbauer Spectroscopy

Mössbauer spectra were recorded on a spectrometer from SEE Co. (Edina, MN) operating in the constant acceleration mode in a transmission geometry. The sample was kept in an SVT-400 cryostat form Janis (Wilmington, MA). The quoted isomer shifts are relative to the centroid of the spectrum of a metallic foil of α-Fe at room temperature (RT). Solution samples were transferred to a sample cup and freeze-quenched with liquid nitrogen inside of the glovebox and then immersed in liquid N_2 until mounted in the cryostat. Data analysis was performed using version 4 of the program WMOSS (www.wmoss.org) and quadrupole doublets were fit to Lorentzian lineshapes. See discussion below for detailed notes on the

fitting procedure.

A3.1.4. Ammonia Quantification

Reaction mixtures are cooled to 77 K and allowed to freeze. The reaction vessel is then opened to atmosphere and to the frozen solution is slowly added a twofold excess (with respect to acid) solution of a NaO^{t}Bu solution in MeOH (0.25 mM) over 1-2 minutes. This solution is allowed to freeze and a Schlenk tube adapter is added and the headspace of the tube is evacuated. After sealing the tube is then allowed to warm to RT and stirred at RT for at least 10 minutes. An additional Schlenk tube is charged with HCl (3 mL of a 2.0 M solution in Et_2O, 6 mmol) to serve as a collection flask. The volatiles of the reaction mixture are vacuum transferred at RT into this collection flask. After completion of the vacuum transfer, the collection flask is sealed and warmed to RT and stirred vigorously for 10 minutes. Solvent is removed in vacuo, and the remaining residue is dissolved in DMSO-d_6 containing 20 mM 1,3,5-trimethoxybenzene as an internal standard. The ammonium chloride is quantified by integration relative to the 1,3,5-trimethoxybenzene internal standard.

A3.1.5. Computational Methods

All stationary point geometries were calculated using DFT-D_3 (Grimmes D_3 dispersion correction[5]) with an TPSS functional,[6] a def2-TZVP[7] basis set on transition metals and a def2-SVP[7] basis set on all other atoms. Calculations were performed, in part, using Xtreme

Science and Engineering Discovery Environment (XSEDE) resources.[8] Calculations were performed on the full P_3^BFe scaffold. Geometries were optimized using the NWChem 6.5 package.[9] All single point energy, frequency and solvation energy calculations were performed with the ORCA package.[10] Frequency calculations were used to confirm true minima and to determine gas phase free energy values (G_{gas}). Single point solvation calculations were done using an SMD solvation model[11, 12] with diethyl ether solvent and were used to determine solvated internal energy (E_{soln}). Free energies of solvation were approximated using the difference in gas phase internal energy (E_{gas}) and solvated internal energy ($\Delta G_{solv} \approx E_{soln} - E_{gas}$) and the free energy of a species in solution was then calculated using the gas phase free energy (G_{gas}) and the free energy of solvation ($G_{soln} = G_{gas} + \Delta G_{solv}$).[13,14] All reduction potentials were calculated referenced to $Fc^{+/0}$ and using the standard Nernst relation $\Delta G = -nFE^0$.

A3.2. Synthetic Details

A3.2.1. General Procedure for the Synthesis of the Anilinium Triflates

Prior to use the amine was purified (aniline and 2,6-dimethylaniline by distillation and the remaining substituted anilines by sublimation). To a 100 mL round bottom flask in the glovebox was added the desired aniline which was subsequently dissolved in 50 mL of Et_2O (no additional drying with NaK). To this was added dropwise (1 equiv) of HOTf with stirring over five minutes. Immediate precipitation of white solid was observed and the reaction mixture was allowed to stir for thirty minutes. The reaction mixture was then filtered and the

resulting white powder was washed with Et_2O (50 mL) and pentane (50 mL). The resulting white microcrystalline material was then dried under vacuum. Yields of greater than 90% of microcrystalline material was obtained in this manner in all cases. The ^1H NMR spectroscopy matched literature reports.[15,16]

A3.3. Ammonia Generation Details

A3.3.1. Standard NH_3 Generation Reaction Procedure

All solvents are stirred with Na/K for ≥2 hours and filtered prior to use. In a nitrogen-filled glovebox, the precatalyst (2.3 μmol) was weighed into a vial. The precatalyst was then transferred quantitatively into a long tube with a female 24-40 joint at the top using THF. The THF was then evaporated to provide a thin film of precatalyst at the bottom of tube. The tube is then charged with a stir bar, the acid (108 eq), and decamethylcobaltocene (41.2 mg, 54 eq) as solids. The tube is then sealed at room temperature with a septum that is secured with copper wire (this ensures a known volume of N_2 in the reaction vessel, which is important for H_2 detection). The tube is then chilled to 77 K and allowed to equilibrate for 10 minutes. To the chilled tube is added 1 mL of Et_2O. The temperature of the system is allowed to equilibrate for 5 minutes. This tube is passed out of the box into a liquid N_2 bath and transported to a fume hood. The tube is then transferred to a dry ice/acetone bath where it thaws and is allowed to stir at −78 °C for four hours. At this point the headspace of the tube is sampled with a 10 mL gas, locking syringe which is used to analyze for H_2. The tube is then allowed to warm to RT with stirring and then stirred at room temperature for a further ten minutes. At this point the previously described procedure for quantifying ammonia was

employed. To ensure reproducibility, all experiments were conducted in 395 mL tubes (51 mm OD) using 25 mm stir bars, and stirring was conducted at ~650rpm.

Table A3.1. NMR quantification results for standard NH_3 generation experiments with $P_3^BFe^+$

Acid	Integration Relative to Internal Standard	% Yield NH_3 (error)	% Yield H_2 (error)
[4-methoxyanilinium][OTf]	0.01, 0.02	0.2(0.1)	89.1(0.2)
[anilinium][OTf]	3.42, 3.33	40.4(0.5)	48.6(0.7)
[2,6-dimethylanilinium][OTf]	4.30, 3.63	47.5(4.0)	37.8(0.2)
[2-chloroanilinium][OTf]	4.98, 4.92	59.3(0.4)	26.1(1.9)
[2,5-dichloroanilinium][OTf]	6.78, 6.15	77.5(3.8)	10.5(1.1)
[2,6-dichloroanilinium][OTf]	6.81, 6.00	76.7(4.9)	12.6(2.5)
[2,6-dichloroanilinium][OTf]*	6.60, 5.81	74.4(4.7)	14.2(3.4)
[2,6-dichloroanilinium][BAr^F_4]	4.12, 3.0	42.7(6.7)	18.8(0.8)
[2,4,6-trichloroanilinium][OTf]	5.73, 6.10	70.9(2.2)	12.0(0.8)

[pentachloroanilinium][OTf]	1.62, 1.70	19.9(0.5)	63.5(1.1)

*Run performed with $[P_3^BFeN_2][Na(Et_2O)_3]$ as the precatalyst.

A3.4. H_2 Monitoring Details

A3.4.1. Standard Background Generation Reaction Procedure

All solvents are stirred with Na/K for ≥2 hours and filtered prior to use. In a nitrogen-filled glovebox, a long tube with a female 24-40 joint is charged with a stir bar, the acid (108 eq) and decamethylcobaltocene (41.2 mg, 54 eq). The tube is then sealed at room temperature with a septum that is secured with copper wire. The tube is then chilled to 77 K and allowed to equilibrate for 10 minutes. To the chilled tube is added 1 mL of Et_2O. The temperature of the system is allowed to equilibrate for 5 minutes. This tube is passed out of the box into a liquid N_2 bath and transported to a fume hood. The tube is then transferred to a dry ice/acetone bath where it thaws and is allowed to stir at −78 °C for four hours. At this point the headspace of the tube is sampled with a 10 mL gas, locking syringe which is used to analyze for H_2.

Table A3.2: Data for Background H_2 Quantification Experiments

Acid	GC Integration for H_2	% Yield H_2
4-methoxyanilinium triflate	49.8	31.5
anilinium triflate	24.0	15.2

2,6-dimethylanilinium triflate	8.2	5.2
2-chloroanilinium triflate	47.2	29.9
2,5-dichloroanilinium triflate	37.1	23.5
2,6-dichloroanilinium triflate	77.8	49.2
2,4,6-trichloroanilinium triflate	34.8	22.0
pentachloroanilinium triflate	98.3	62.3

A3.4.2. H_2 Evolution Kinetics

All solvents are stirred with Na/K for ≥2 hours and filtered prior to use. For the catalyzed run, the precatalyst was then transferred quantitatively into a Schlenk tube using THF. The THF was then evaporated to provide a thin film of precatalyst at the bottom of the long tube with a female 24-40 joint. The tube is then charged with a stir bar and the 2,6-dichloroanilinium triflate (77.9 mg, 108 eq) and decamethylcobaltocene (41.2 mg, 54 eq) are added as solids. The tube is then sealed at room temperature with a septum that is secured with copper wire. The tube is then chilled to 77 K and allowed to equilibrate for 10 minutes. To the chilled tube is added 1 mL of Et_2O. The temperature of the system is allowed to equilibrate for 5 minutes. This tube is passed out of the box into a liquid N_2 bath and transported to a fume hood. The tube is then transferred to a dry ice/acetone bath where it thaws and is allowed to stir at −78 °C. As soon as the stir bar is freed from the frozen solution

and stirring begins the timing is started. At the time points noted below the headspace was sampled for H_2 with a 10 mL gas tight syringe.

Table A3.3. Time points for catalyzed H_2 evolution from 2,6-dichloroanlinium triflate and decamethylcobaltocene

Time	GC Integration for H_2	% Yield H_2 (error)
5	3.8, 6.4	3.3(0.9)
15	11.6, 16.9	9.3(1.8)
25	14.7, 26.2	13.4(3.8)
35	22.5, 20.8	13.9(0.5)

Table A3.4. Time points for uncatalyzed H_2 evolution from 2,6-dichloroanlinium triflate and decamethylcobaltocene

Time	GC Integration for H_2	% Yield H_2 (error)

5	3.3, 2.9	2.0(0.1)
15	7.0, 6.2	4.3(0.3)
25	8.8, 11.1	6.3(0.8)
65	20.7, 27.0	14.5(1.7)

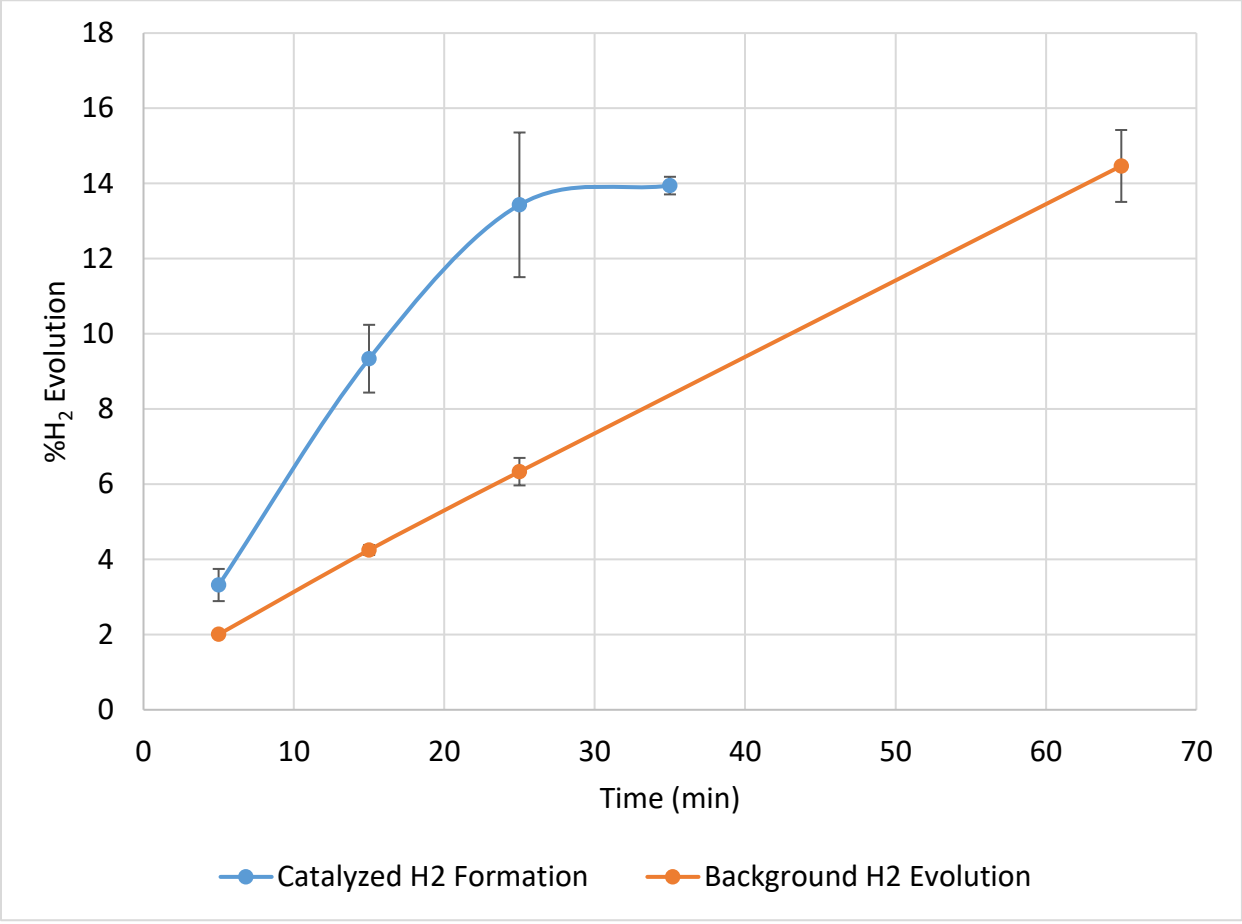

Figure A3.1: Comparison of catalyzed and uncatalyzed H_2 evolution from 2,6-dichloroanlinium triflate and decamethylcobaltocene at early time points.

A3.5. Mössbauer Spectroscopy

A3.5.1. General Procedure for Freeze-Quench Mössbauer Spectroscopy

All solvents are stirred with Na/K for ≥2 hours and filtered prior to use. In a nitrogen-filled glovebox, the desired ^{57}Fe species (0.0023 mmol) is quantitatively transferred using THF to a vial and then evaporated to yield a thin film. That vial is charged with a small stir bar and the other reagents as solids. The vial is then chilled to 77 K in a liquid nitrogen bath and allowed to equilibrate for five minutes. To the chilled tube is added 1 mL of Et_2O and this allowed to equilibrate for another five minutes. The vial is then transferred to a cold well that has been pre-cooled for at least fifteen minutes to −78 °C with a dry ice/acetone bath. When the stir bar is freed from the frozen solvent and begins to stir the time is started. At the time noted the stirring is stopped and using a prechilled pipette the reaction mixture is transferred in one portion to a pre-chilled Mössbauer cup sitting in a vial. The vial is then placed in a liquid nitrogen bath causing the reaction mixture to freeze in approximately twenty seconds. The Mössbauer cup is then submerged in the liquid nitrogen and then removed from the glovebox and standard procedure is used to mount the sample on the Mössbauer spectrometer.

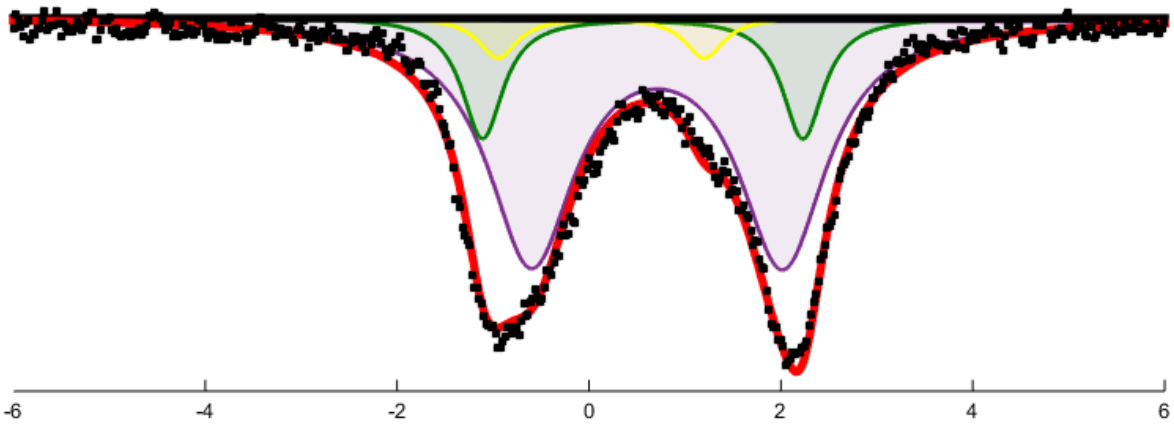

Figure A3.2. Mössbauer spectrum collected from a reaction freeze quenched after stirring for 5 minutes at −78 °C in 1 mL of Et_2O between [P3B(^{57}Fe)N_2][Na(Et_2O)$_3$] and excess 2,6-dichloroanilinium triflate (50 equiv). Raw data shown as black points, simulation as a solid red line, with components in (see Table A3.3 for parameters). The spectrum was collected at 80 K with a parallel applied magnetic field of 50 mT as a suspension in Et_2O.

Fitting details for Figure A3.2: Three quadrupole doublets were found to be necessary to obtain an adequate simulation. Although a variety of parameters could potentially simulate the relatively broad absorptions observed here, previous reactivity of $[P_3^BFeN_2]^-$ with acid suggested that $P_3^BFeN_2$ and $[P_3^BFe]^+$ were likely products. Satisfyingly if one of those components was provided to the fitting program the other major component was found to be the other species after refining freely. The third species was unchanged in these simulations and represents an unknown species but is demanded by the inflection point on the more negative side of the right-hand absorbance. Modeling this feature also helps to capture the asymmetry of the left-hand absorbance while using the symmetric line-shapes we expect for

$P_3{}^BFeN_2$ (green) and $P_3{}^BFe^+$ (purple). The broad linewidths for $P_3{}^BFe^+$ have been observed previously and may be explained by the existence of unbound and bound varieties of the species with the reaction mixture providing potential ligands such as OTf^-, $^{2,6\text{-}Cl}PhNH$, and N_2.

Table A3.5: Simulation parameters for Mossbauer spectrum in Figure A3.2.

Component	δ (mm s^{-1})	ΔE_Q (mm s^{-1})	Linewidths, Γ_L/Γ_R (mm s^{-1})	Relative area
A (green)	0.58 ± 0.02	3.28 ± 0.07	0.52/0.52	0.26
B (purple)	0.76 ± 0.02	2.57 ± 0.05	1.10/1.10	0.63
C (yellow)	0.13 ± 0.02	2.24 ± 0.04	0.50/0.50	0.11

A3.6. EPR Spectroscopy

A3.6.1 General Procedure for EPR Spectroscopy

All solvents are stirred with Na/K for ≥2 hours and filtered prior to use. In a nitrogen-filled glovebox, the desired Fe species (0.0023 mmol) is quantitatively transferred using THF to a vial and then evaporated to yield a thin film. That vial is charged with a small stir bar and the

acid (0.116 mmol, 50 eq) as solids ([2,6-dichloroanilinium][OTf] or [2,6-dichloroanilinium][Bar^F_4]). The vial is then chilled to 77 K in a liquid nitrogen bath and allowed to equilibrate for five minutes. To the chilled tube is added 1 mL of Et_2O (for HOTf 50 eq have been dissolved in this 1 mL of Et_2O at room temperature) and this allowed to equilibrate for another five minutes. The vial is then transferred to a cold well that has been pre-cooled for at least fifteen minutes to −78 °C with a dry ice/acetone bath. When the stir bar is freed from the frozen solvent and begins to stir the time is started. The reaction mixture is stirred for five minutes and then stirring is stopped. Using a pre-chilled pipette approximately 0.5 mL of the reaction mixture is rapidly transferred to a pre-chilled X-band EPR tube. The X-band EPR tube is then placed in a liquid nitrogen bath causing the reaction mixture to freeze in approximately twenty seconds. The EPR tube is then sealed and removed from the glovebox in liquid nitrogen.

A3.6.2. Comment on Stoichiometric Reactivity

In our attempt to model the catalytic reaction mixture we were interested in the reactivity of $[P_3^BFeN_2]^-$ (observed previously both from mixing $[P_3^BFe][Bar^F_4]$ with excess Cp^*_2Co and under the catalytic reaction conditions) with acid. In order to achieve this we wanted to prepare independently known $[P_3^BFeN_2]^-$ species to model the proposed catalytic intermediate $[P_3^BFeN_2][Cp^*_2Co]$. We chose $[P_3^BFeN_2][Na(Et_2O)_3]$ because its solubility in Et_2O modeled that of $[P_3^BFeN_2][Cp^*_2Co]$.

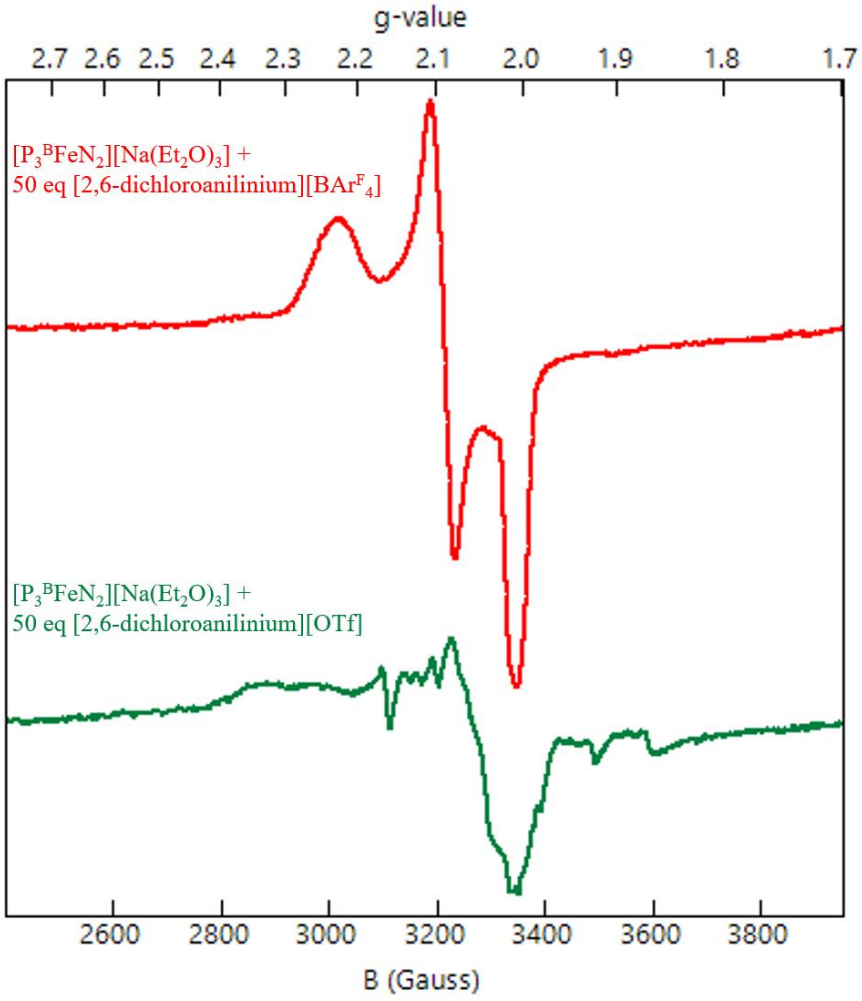

Figure A3.3. The continuous wave, X-band EPR at 77K in Et_2O of reaction mixtures freeze-quenched after five minutes. In red is the reaction of $[P_3^BFeN_2][Na(Et_2O)_3]$ with 50 eq of [2,6-dichloroanilinium]$[BAr^F_4]$ clearly demonstrating the formation of $[P_3^BFeNNH_2][BAr^F_4]$. In green is reaction of $[P_3^BFeN_2][Na(Et_2O)_3]$ with 50 eq of [2,6-dichloroanilinium][OTf] in which the small residual species is neither the starting material ($[P_3^BFeN_2][Na(Et_2O)_3]$) or the desired product ($[P_3^BFeNNH_2][OTf]$). Although we do not know the chemical identity of this species we note that it is very similar to the EPR

observed in the reaction of $[P_3^BFeN_2][Na(12\text{-crown-}4)_2]$ with 1 eq. of $HBAr^F_4$.[17] We hypothesize therefore that it may represent a Fe–H side product.

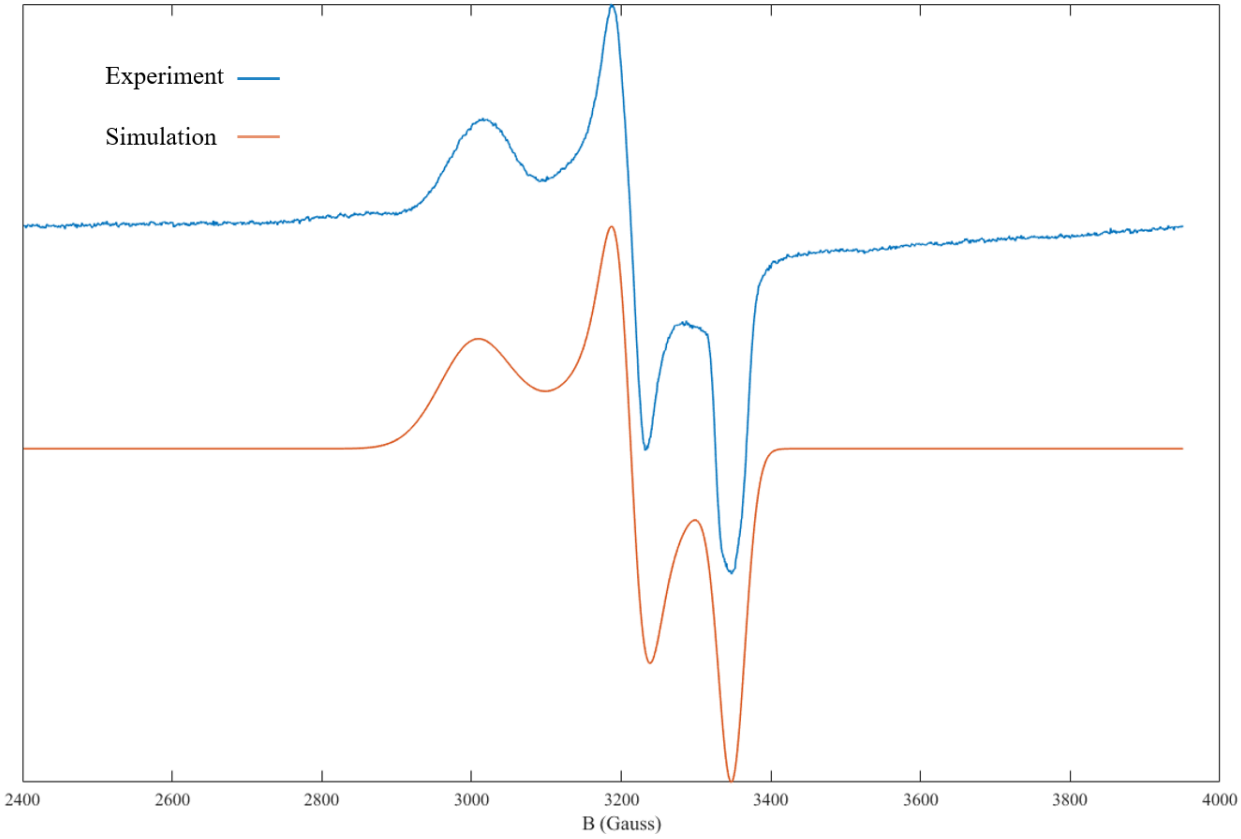

Figure A3.4. In blue is the continuous wave, X-band EPR spectrum at 77K of a reaction mixture of 50 eq. [2,6-dichloroanilinium][Bar^F_4] with $[P_3^BFeN_2][Na(12\text{-crown-}4)_2]$ quenched with liquid nitrogen after 5 minutes. In orange is the simulation of this spectrum (fitting details below)

Fitting details for Figure A3.4: The parameters used to fit the spectrum were obtained using the esfit application in the easyspin program.[18] The fitting program obtains the best fit by minimizing the root mean square deviation from the data.

The data was fit with the following parameters: g_1 = 2.23899, g_2 = 2.09189, g_3 = 2.00664, and a line broadening of 323.8530, 71.2309, and 38.7902 MHz respectively. These parameters represent only a very small perturbation from those used previously to model $[P_3^BFeNNH_2][Bar^F{}_4]$: g_1 = 2.222, g_2 = 2.091, g_3 = 2.006 and a line broadening of 256, 113, and 41 MHz respectively.[17] The slightly broader spectrum observed here precludes resolution of the small phosphorus coupling on g_3. We believe that this broadening arises from either the use of a non-glassing solvent (Et_2O vs 2-MeTHF) or via small differences in hydrogen-bonding that arise from the presence of 2,6-dichloroaniline.

A3.7. Acid Quench of $P_3^BFeN_2^-$

A3.7.1 Standard Acid Quench Procedure

All solvents are stirred with Na/K for ≥2 hours and filtered prior to use. In a nitrogen-filled glovebox, the desired Fe species (2.3 μmol) was weighed into a vial. The precatalyst was then transferred quantitatively into a Schlenk tube using THF. The THF was then evaporated to provide a thin film of Fe species at the bottom of the Schlenk tube. The tube is then charged with a stir bar and [2,6-dichloroanilinium][OTf (36.2 mg, 115 μmol, 50 eq) is added as a solid. The tube is then sealed at room temperature with a septum and a Konte's valve that is left partially open. The tube is then chilled to 77 K and allowed to equilibrate for 10 minutes. To the chilled tube is added 1 mL of Et_2O through the septum. The temperature of the system is allowed to equilibrate for 5 minutes and then the Konte's valve is sealed. This tube is passed out of the box into a liquid N_2 bath and transported to a fume hood. The tube is then

transferred to a dry ice/acetone bath where it thaws and is allowed to stir at −78 °C for three hours. At the end of the reaction the Konte's valve is opened and the reaction headspace is allowed to equilibrate. At this point the headspace of the tube is sampled with a 10 mL gas, locking syringe which is used to analyze for H_2. The tube is then allowed to warm to RT with stirring and then stirred at room temperature for a further ten minutes. At this point the previously described procedure for quantifying ammonia was employed.

Table A3.6. Comparative NH_3 and H_2 Yields for [$^{2,6\text{-}Cl}$PhNH$_3$][OTf] and [$^{2,6\text{-}Cl}$PhNH$_3$][BAr$^F{}_4$]

Acid	Integration Relative Internal Standard	% Yield NH_3 (error)	% Yield H_2	% Yield H_2 (error)
[2,6-dichloroanilinium][OTf]	0.00, 0.00	0.0(0.0)	39.0, 48.2	43.7(4.6)
[2,6-dichloroanilinium][BAr$^F{}_4$]	0.36, 0.25	0.20(0.03)	30.3, 45.6	37.8(7.6)

A3.8. Solubility Measurement

A3.8.1. Procedure for Measuring Solubility of Cp*$_2$Co

All solvents are stirred with Na/K for ≥2 hours and filtered prior to use. In a nitrogen-filled glovebox, a Schlenk tube is charged with a stir bar and the Cp*$_2$Co (41.2 mg, 0.125 mmol)

is added to the tube. The tube is then chilled to 77 K in a liquid nitrogen bath and allowed to equilibrate for 5 minutes. To the chilled tube is added 1 mL of Et_2O. The temperature of the system is allowed to equilibrate for 5 minutes and then the Schlenk tube is transferred to the cold well which has been prechilled to −78 °C for fifteen minutes. After five minutes of stirring at ~620 rpm, the stirring is stopped. With a prechilled pipette the entirety of the reaction mixture is transferred to a similarly prechilled celite pad for filtration. Filtration yielded a pale green solution that was then warmed to room temperature and the solvent was removed under reduced pressure. The vial was then extracted with a 20 mM solution of 1,3,5-trimethoxybenzene in C_6D_6. The NMR was then measured and the Cp^*_2Co signal was integrated relative to the 1,3,5-trimethoxybenzene standard. The accuracy of this integration procedure was confirmed by performing this procedure on a sample of Cp^*_2Co that had simply been weighed into a vial. Repetition of this experiment resulted in Cp^*_2Co concentrations between 5-6 mM.

A3.8.2. Procedure for Measuring Solubility of [2,6-dichloroanilinium][OTf]:

All solvents are stirred with Na/K for ≥2 hours and filtered prior to use. In a nitrogen-filled glovebox, a Schlenk tube is charged with a stir bar and the [2,6-dichloroanilinium][OTf] (77.9 mg, 0.250 mmol) is added to the tube. The tube is then chilled to 77 K in a liquid nitrogen bath and allowed to equilibrate for 5 minutes. To the chilled tube is added 1 mL of Et_2O. The temperature of the system is allowed to equilibrate for 5 minutes and then the Schlenk tube is transferred to the cold well which has been prechilled to −78 °C for fifteen minutes. After five minutes of stirring at ~620 rpm, the stirring is stopped. With a prechilled

pipette the entirety of the reaction mixture is transferred to a similarly prechilled celite pad for filtration. Filtration yielded a colorless solution that was then warmed to room temperature and the solvent was removed under reduced pressure. The vial was then extracted with a 20 mM solution of 1,3,5-trimethoxybenzene in THF-d_8. The NMR was then measured and the two signals for [2,6-dichloroanilinium][OTf] were integrated relative to the 1,3,5-trimethoxybenzene standard. The result was a [2,6-dichloroanilinium][OTf] concentration of 0.4 mM.

A3.9. Controlled Potential Electrolysis (CPE) and Cyclic Voltammetry (CV) Details

General considerations. All manipulations are carried out in an N_2 filled glove box. For CPE experiments a sealable H-cell consisting of two compartments separated by a fine porosity sintered glass frit is cooled to −35 °C in a cold well and charged with 4 mL (working chamber) and 4 mL (auxiliary chamber) of 0.1 M $NaBAr^F{}_4$ solution in Et_2O, the solutions are also cooled to −35 °C and the solution for the working chamber may contain additional chemical components as described below. The working chamber is outfitted with a glassy carbon working electrode, rectangular prismatic in shape with dimensions of 10 mm x 2 mm and submerged in the working chamber solution to a depth of ~10 mm. The working chamber is also equipped with a $Ag/AgPF_6$ in 0.1 M $NaBAr^F{}_4$ Et_2O reference electrode isolated by a CoralPor™ frit (obtained from BASi) and referenced externally to Fc/Fc^+. The auxiliary chamber is outfitted with a solid sodium auxiliary electrode (~5 mm by ~1 mm rectangular prism, submerged to ~5 mm). The cell is sealed before electrolysis. The cell is connected to

a CH Instruments 600B electrochemical analyzer and controlled potential bulk electrolysis experiments were performed at −35 °C with stirring, cold well external bath temperature maintained by a SP Scientific FTS Systems FC100 immersion cooler.

CV experiments are conducted in a single compartment cell cooled to −35 °C in a cold well in 0.1 M $NaBAr^F_4$ Et_2O solution, again cold well external bath temperature maintained by a SP Scientific FTS Systems FC100 immersion cooler. The working electrode is a glassy carbon disk, the reference electrode is a $Ag/AgPF_6$ in 0.1 M $NaBAr^F_4$ Et_2O reference electrode isolated by a CoralPor™ frit (obtained from BASi) and referenced externally to Fc/Fc^+, the auxiliary electrode is a platinum wire. Measurements conducted with a CH Instruments 600B electrochemical analyzer

General methodology for controlled potential electrolysis experiments: To the working chamber is added 3 mg of $[P_3{}^BFe][BAr^F_4]$ (2 μmol), 100 μmol of acid (e.g. $[Ph_2NH_2][OTf]$), 0-23.8 mg of $[CoCp^*_2][BAr^F_4]$ (0-20 μmol), and a magnetic stir bar. The cell is held at a working potential of −2.1 V vs Fc/Fc^+ until the current passed in the cell falls to 1% of the initial current pass or until 21.5 hours have passed. After that time the potential bias is removed, the headspace of the cell is sampled with a sealable gas syringe (10 mL), which is immediately analyzed by GC for the presence of H_2. Then an additional 100 μmol of acid in 2 mL 0.1 M $NaBAr^F_4$ solution in Et_2O is injected through rubber septa into both chambers to sequester NH_3 as $[NH_4][OTf]$. The cell is allowed to stir at -35 °C for 10 minutes and then warmed to room temperature. The contents of both chambers are then transferred to a

Schlenk tube (cell washed with additional Et_2O) and this material is analyzed for NH_3 by base digestion, vacuum transfer of volatiles, and NMR integration as described in section A1.4

Methodology for controlled potential electrolysis experiments with reloading of substrate: To the working chamber is added 3 mg of $[P_3^BFe][BAr^F_4]$ (2 μmol), 100 μmol of acid (e.g. $[Ph_2NH_2][OTf]$), 0-23.8 mg of $[CoCp^*_2][BAr^F_4]$ (0-20 μmol), and a magnetic stir bar. The cell is held at a working potential of −2.1 V vs Fc/Fc^+ until the current passed in the cell falls to 1% of the initial current pass or until 21.5 hours have passed. After that time the potential bias is removed. An additional 100 μmol of acid in 2 mL 0.1 M $NaBAr^F_4$ solution in Et_2O is then added to the working chamber of the cell via injection through a rubber septum. The cell is then held at a working potential of −2.1 V vs Fc/Fc^+ until the current passed in the cell falls to 1% of the initial current pass or until 21.5 hours have passed. After that time the potential bias is removed, the headspace of the cell is sampled with a sealable gas syringe (10 mL), which is immediately analyzed by GC for the presence of H_2. Then an additional 100 μmol of acid in 2 mL 0.1 M $NaBAr^F_4$ solution in Et_2O is injected through rubber septa into both chambers of the cell to sequester NH_3 as $[NH_4][OTf]$. The cell is allowed to stir at -35 °C for 10 minutes and then warmed to room temperature. The contents of both chambers are then transferred to a Schlenk tube (cell washed with additional Et_2O) and this material is analyzed for NH_3 by base digestion, vacuum transfer of volatiles, and NMR integration as described in section A1.4

Table A3.7. Controlled Potential Electrolysis Data.

Entry	Acid	Equiv [$CoCp^*_2$] [BAr^F_4]	Time (h)	Charge Passed (C)	Yield of NH_3 (equiv per Fe)	FE NH_3 (%)	FE H_2[a] (%)
1	$[Ph_2NH_2][OTf]$	0	42	7.5	2.3	18	80
2	$[Ph_2NH_2][OTf]$	0	63	6.2	2.8	26	25
Avg					2.6 ± 0.4	22 ± 6	
3[b]	$[Ph_2NH_2][OTf]$	0	43	7.5	2.2	17	67
4	$[Ph_2NH_2][OTf]$	1	17	8.1	4.4	31	56
5	$[Ph_2NH_2][OTf]$	1	22	8.3	3.5	24	47
Avg					4.0 ± 0.6	28 ± 5	
6	$[Ph_2NH_2][OTf]$	5	17	8.5	3.9	26	61
7	$[Ph_2NH_2][OTf]$	5	21	9.1	3.5	22	57
8	$[Ph_2NH_2][OTf]$	5	22	9.5	4.6	28	27
Avg					4.0 ± 0.6	25 ± 3	
9	$[Ph_2NH_2][OTf]$	10	21	9.4	3.0	19	64
10	$[Ph_2NH_2][OTf]$	10	10	10.2	5.1	29	47

Avg					4 ± 1	24 ± 7	
11	[$PhNH_3$][OTf]	5	15	9.0	1.2	8	48
12	[$PhNH_3$][OTf]	5	22	7.8	0.6	4	35
Avg					0.9 ± 0.4	6 ± 3	
13	[2,6-Cl_2 $PhNH_3$][OTf]	5	17	10.6	2.0	11	44
14	[2,6-Cl_2 $PhNH_3$][OTf]	5	17	10.7	1.7	9	41
Avg					1.9 ± 0.2	10 ± 1	
15[b]	[Ph_2NH_2][OTf]	5	32	17.3	6.1	20	43
16[b]	[Ph_2NH_2][OTf]	5	22	18.7	6.7	21	32
17[b]	[Ph_2NH_2][OTf]	5	37	13.7	4.7	20	38
18[b]	[Ph_2NH_2][OTf]	5	41	15.3	4.8	18	52
19[b]	[Ph_2NH_2][OTf]	5	43	17.8	5.4	18	31
Avg					5.5 ± 0.9	19 ± 1	
20A[c]	[Ph_2NH_2][OTf]	5	21.5	9.5	4.6	28	27
20B[c]	[Ph_2NH_2][OTf]	5	11.5	9.2	0.0	0	88

21[d]	$[Ph_2NH_2][OTf]$	5	16	9.2	0.0	0	75
22[e]	$[Ph_2NH_2][OTf]$	5	43	0.0	0.3	N/A	N/A
23[f]	$[Ph_2NH_2][OTf]$	Chemical runs	21.5	N/A	1.3	7.8 e^-	50 e^-
24[f]	$[Ph_2NH_2][OTf]$	Chemical runs	21.5	N/A	2.3	13.8 e^-	31 e^-
Avg					1.8 ± 0.7	11 ± 4	

[a]Some ports of the cell are sealed with septa and one of these is pierced before the electrolysis begins to pressure equilibrate the cell as it cools to -35 °C, we note therefore that H_2 gas may escape from the cell particular during long experiments, indeed a test of H_2 retention in the cell under equivalent conditions revealed leakage of H2 thus the detected % yield of H_2 reported here should be considered a lower limit. [b]These experiments were conducted using the reloading protocol as described above. [c]Electrode rinse test as described in main text. [d]Control experiment with no $[P_3^BFe][BAr^F_4]$ included but including a typical loading of 11.9 mg (10 μmol) of $[CoCp^*_2][BAr^F_4]$. [e]Control experiment where the cell, with all components including the sodium auxiliary electrode, was assembled and stirred at -35 °C for 43 hours but no potential bias was applied. [f]Chemical catalysis runs at -35 °C in 0.1 M $NaBAr^F_4$ Et_2O solution with 50 equiv (100 μmol) of Cp^*_2Co included as a chemical reductant as well as $[P_3^BFe][BAr^F_4]$ (2 μmol) and 100 μmol of acid ($[Ph_2NH_2][OTf]$).

A3.10. Computational Details

A3.10.1. Calculation of Acid Dissociation Constants

Acid dissociation constants (pK_a and pK_d) were performed were optimized and solvated as discussed in the general methods section. For pK_a values, the □G for the exchange of a proton (H^+) between the acid of interest and $^{2,6\text{-Cl}}PhNH_2/^{2,6\text{-Cl}}PhNH_3^+$. For p$K_d$ values, the same approach was used except that the net exchange of a HOTf unit was calculated. In all cases the dissociation constant was reference to the literature value for the pK_a of $^{2,6\text{-Cl}}PhNH_3^+$ in THF.

A4.10.2. Determination of PT, ET and PCET Kinetics

Kinetic barriers for reported for PT, ET and PCET were performed in one of two ways. Internal consistency between the methods was determined where possible. Values are summarized in Table A3.8.

Method A. Marcus Theory. Standard Marcus theory expressions[19] were used in method A. Inner sphere reorganization energies for PT or PCET were calculated using the method developed by the group of Hammes-Schiffer (Eq. A3.1) utilizing the force constants for the reactant (f_j^r) and product (f_j^p) species and the change in equilibrium bond length (Dq$_j$).[20]

$$\lambda_{is,PT/PCET} = \sum_j \frac{f_j^r f_j^p}{f_j^r + f_j^p} \Delta q_j{}^2$$

(Eq. A3.1)

Outer sphere reorganization energies were calculated using a continuum solvation model for the solvation of a point charge ($\lambda_{os,ET}$)[19] or a dipole ($\lambda_{os,PT}$).[20-22] The $\lambda_{os,PCET}$ was approximated using equation A3.2, where θ is the angle between the ET and PT vectors.[20] It was determined via analysis of the structure of a constrained optimization (in which the Fe−H–Co distance was kept constant) that θ is between 0 and 45°, a range which corresponds to an insignificant variation (less than 0.2 kcal/mol) in $\lambda_{os,PCET}$.

$$\lambda_{os,PCET} = \lambda_{os,PT} + \lambda_{os,ET} - (\lambda_{os,PT} * \lambda_{os,ET})\cos(\theta) \quad \text{(Eq. A3.2)}$$

Relative rates for a bimolecular PT/ET vs PCET (k_{bi}) pathway for reaction shown in Table A3.8, Equation 6 were determined via the method outline by the group of Hammes-Schiffer in which the bimolecular rate constant for PT, ET or PCET is approximated by equation A3.3.

$$k_{bi} = K_A * k_{uni} \quad \text{(Eq. A3.3)}$$

K_A represents the pre-arrangement equilibrium constant and k_{uni} represents the unimolecular rate constant for PCET or ET.[23] Along an PT/ET pathway, the barriers calculated suggest that $k^{PT} > k^{ET}$. In approximating k_{uni} for PCET and ET, we made extensive use of the webPCET portal.[22] The electronic coupling for PCET and ET was assumed to be equal. In order to approximate a lower bound for k^{PCET}/k^{ET}, the pre-arrangement equilibrium (K_A) was also assumed to be equal for PCET and ET. We believe this represents a lower bound as the approximation for K_A does not include any hydrogen bonding interactions for a PCET

pathway.

Method B. Optimization of a 1st Order Saddle Point. PT barriers for the protonation of Cp^*_2Co was also performed using optimization of a 1st order saddle point.

Table A3.8. Overview of Parameters Used to Calculate Kinetic Barriers

1. $[^{2,6\text{-Cl}}PhNH_3][OTf] + Cp^*_2Co \rightarrow Cp^*Co(\eta^4\text{-}C_5Me_5H)\text{-}OTf + {}^{2,6\text{-Cl}}PhNH_2$

2. $[^{2,6\text{-Me}}PhNH_3][OTf] + Cp^*_2Co \rightarrow Cp^*Co(\eta^4\text{-}C_5Me_5H)\text{-}OTf + {}^{2,6\text{-Me}}PhNH_2$

3. $[^{4\text{-OMe}}PhNH_3][OTf] + Cp^*_2Co \rightarrow Cp^*Co(\eta^4\text{-}C_5Me_5H)\text{-}OTf + {}^{4\text{-OMe}}PhNH_2$

4. $P_3{}^BFe(NNH) + [Cp^*Co(\eta^4\text{-}C_5Me_5H)][OTf] \rightarrow [P_3{}^BFe(NNH)_2][OTf] + Cp^*_2Co$

5. $[P_3{}^BFe(NNH)_2][OTf] + Cp^*_2Co \rightarrow P_3{}^BFe(NNH_2) + [Cp_2{}^*Co][OTf]$

6. $P_3{}^BFe(NNH) + [Cp^*Co(\eta^4\text{-}C_5Me_5H)][OTf] \rightarrow P_3{}^BFe(NNH)_2 + [Cp^*_2Co][OTf]$

Reaction	λ_{is}	λ_{os}	Barrier $\{k_{rel}\}$	Method
1	N/A	N/A	1.3 kcal/mol	A
1	7.5 kcal/mol	6.3 kcal/mol	1.3 kcal/mol	B
2	N/A	N/A	3.8 kcal/mol	A
2	7.5 kcal/mol	6.3 kcal/mol	3.6 kcal/mol	B

3	N/A	N/A	4.5 kcal/mol	A
3	7.5 kcal/mol	6.3 kcal/mol	4.8 kcal/mol	B
4	8.9 kcal/mol	6.3 kcal/mol	1.5 kcal/mol	A
5	8.9 kcal/mol	25.0 kcal/mol	4.1 kcal/mol	A[a]
			$\{k_{rel} \equiv 1\ M^{-1}s^{-1}\}$	
6	13.7 kcal/mol	0-10 kcal/mol	0.2 – 0.6 kcal/mol	A
			$\{2000 – 4500\ M^{-1}s^{-1}\}$	

[a]The barrier for $[P_3^BFe(NNH_2)][OTf]$ reduction was calculated assuming that rate-determining reduction to $[P_3^BFe(NNH_2)][OTf]^-$ precedes OTf^- release.

A3.10.3. BDFE Calculations

Bond dissociation free energies (BDFE) of X–H bonds were calculated in the gas-phase using a series of known reference compounds.[25] The free-energy difference between the H-atom donor/acceptor pair was calculated based on the thermochemical information provided by frequency calculations after structure optimizations using the procedure described in the general computational section. A linear plot of ΔG vs $BDFE_{lit}$ was generated to form a calibration curve (**Figure A3.5.**). BDFE predictions were generated by application of the line of best fit to the calculated ΔG of the unknown species.

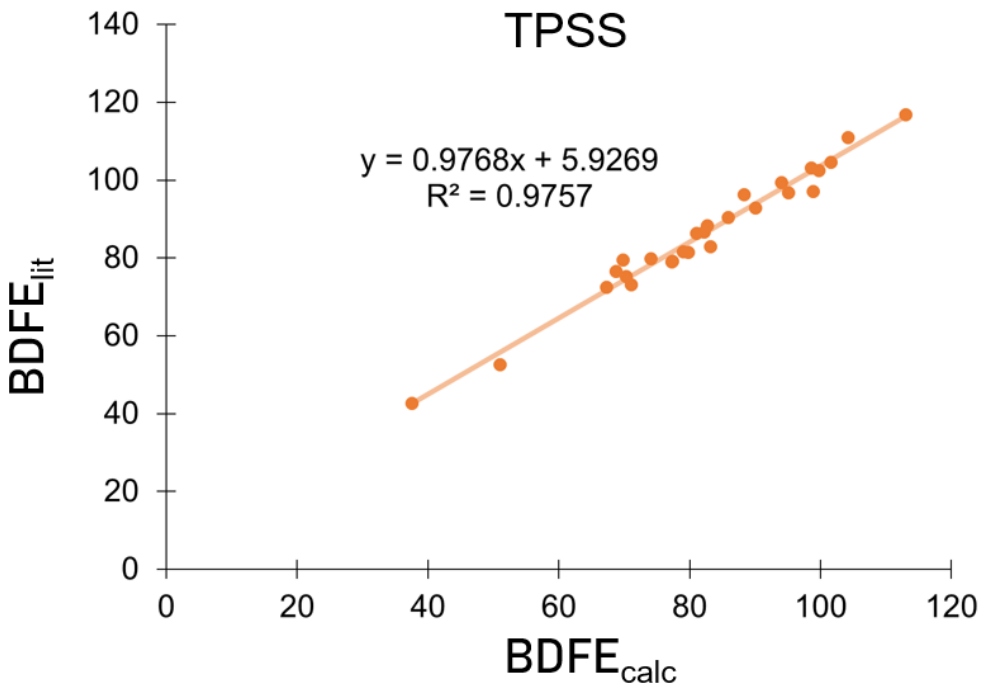

Figure A3.5. $BDFE_{calc}$ and $BDFE_{lit}$ plotted for species of known $BDFE_{E-H}$. Line of best fit is shown.

Table A3.9. Data used to generate the plot and line of best fit shown in Figure A3.5.

	DG (E-H)	DG ($E^{\bullet}$)	DG_{calc}	$BDFE_{E-H}$
HOOH	-151.4	-150.8	69.8	79.7

MeOH	-115.6	-115.0	88.3	96.4
EtOOH	-230.0	-229.4	68.7	76.6
H_2O	-76.4	-75.7	104.2	111.0
NH_3	-56.5	-55.8	94.0	99.4
Me_3CH	-158.3	-157.6	82.7	88.3
PhOH	-307.2	-306.6	74.0	79.8
Et_2NH	-213.6	-212.9	81.0	86.4
NH_2NH_2	-111.8	-111.1	67.3	72.6
OH^-	-75.7	-75.0	98.6	103.1
PhSH	-630.2	-629.5	70.3	75.3
NH_4^+	-56.8	-56.1	113.0	116.9
Me_2CH_2	-119.0	-118.4	85.9	90.4
HC(O)OOH	-264.7	-264.1	82.2	86.8
OOH	-150.8	-150.2	37.5	42.7
C_6H_6	-232.1	-231.4	101.6	104.7
C_2H_4	-78.5	-77.8	99.7	102.5

C_2H_6	-79.7	-79.1	90.0	92.9
$PhCH_3$	-271.3	-270.7	79.0	81.6
CH_4	-40.5	-39.8	95.1	96.8
CpH	-193.9	-193.3	71.0	73.2
EtSH	-477.8	-477.2	77.2	79.1
MeSH	-438.6	-437.9	77.3	79.2
$PhNH_2$	-287.4	-286.7	79.8	81.5
NHNH	-110.6	-110.0	51.0	52.6
H_2S	-399.3	-398.7	83.1	83.0
H_2	-1.2	-0.5	98.8	97.2

A3.11. X-ray Photoelectron Spectroscopy (XPS) details

The surface composition of the carbon electrode surface after a 15 hour bulk electrolysis in the presence of $P_3{}^BFe^+$, $Cp^*_2Co^+$, $[Ph_2NH_2][OTf]$ and N_2 was determined via XPS on a Kratos Axis Nova spectrometer with DLD (Kratos Analytical; Manchester, UK). The excitation source for all analysis was monochromatic Al $K\alpha_{1,2}$ ($h\nu$ = 1486.6 eV) operating at 10 mA and 15 kV. The X-ray source was directed 54° with respect to the sample normal. A base pressure of 1×10^{-9} Torr is maintained in the analytical chamber, which rises to 5 ×

10^{-9} Torr during spectral acquisition. All spectra were acquired using the hybrid lens magnification mode and slot aperture, resulting in an analyzed area of 700 μm × 400 μm. Survey scans were collected using 160 eV pass energy, while narrow region scans used 10 eV; charge compensation via the attached e^--flood source was not necessary in this study.

Subsequent peak fitting and composition analysis was performed using CasaXPS version 2.3.16 (Casa Software Ltd.; Teignmouth, UK). Energy scale correction for the survey and narrow energy regions was accomplished by setting the large component in the C 1s spectrum, corresponding to a C 1s C(=C) transition, to 284.8 eV. All components were fitted using a Gaussian 30% Lorentzian convolution function. For quantification, Shirley baselines were employed where there was a noticeable change in CPS before and after the peak in the survey spectrum; otherwise, linear was chosen. Atomic percentages were calculated using the CasaXPS packages for regions and/or components and are reported herein. Calculations were performed using region or component areas normalized to relative sensitivity factors specific to the instrument conditions with deconvolution from the spectrometer transmission function.

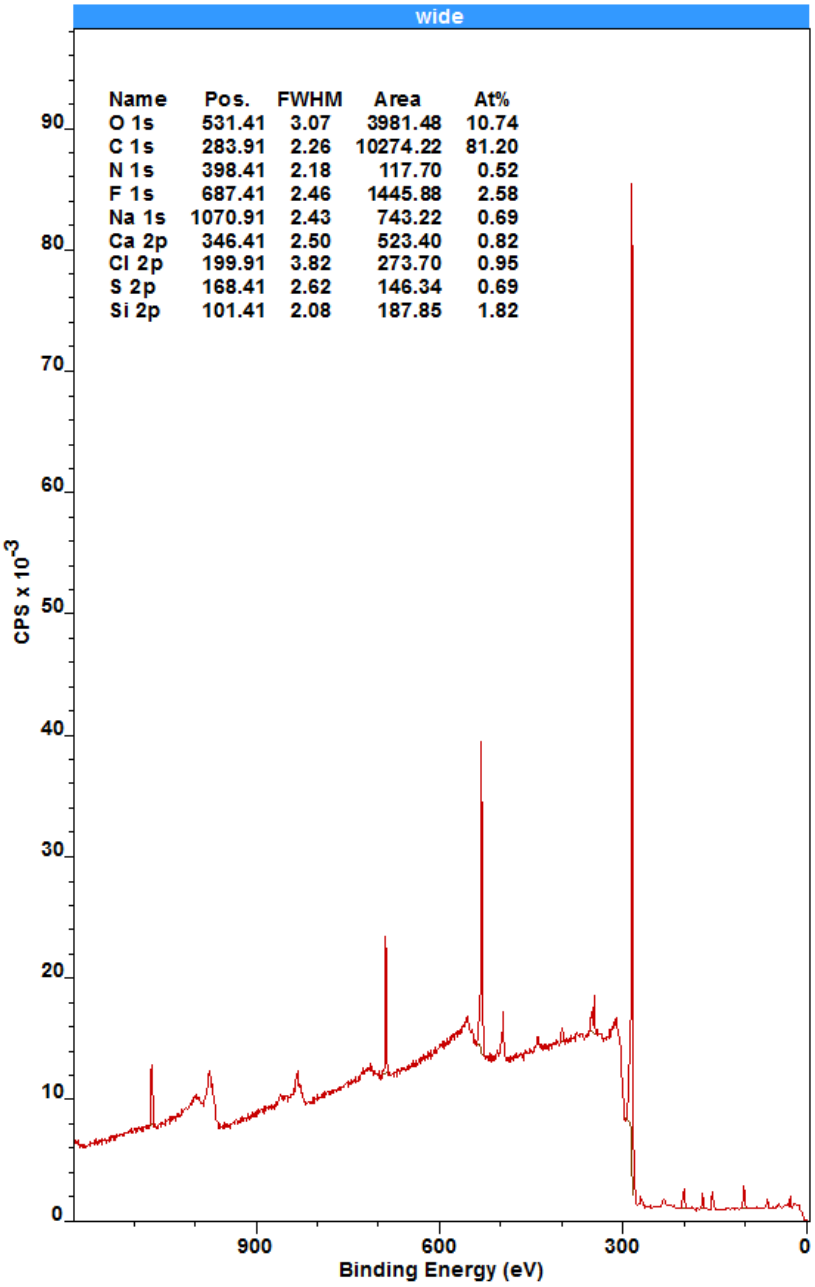

Figure A3.6. XPS survey scan of a section of a glassy carbon plate which was not exposed to the working chamber solution during a 15 hour bulk electrolysis in the presence of $P_3{}^{B}Fe^{+}$, $Cp^*_2Co^{+}$, $[Ph_2NH_2][OTf]$ and N_2 at -2.1 V (vs Fc/Fc^{+}). XPS and Auger peaks are assigned as labeled in the legend, which also includes atomic percentages calculated from

component fits from scans of individual XPS regions. This material represents a baseline of the electrode surface composition resulting from cleaning, polishing, and handling prior to CPE experiments and is provided for comparison to a XPS survey scan of a section of the same glassy carbon plate which was exposed to the working chamber solution during a 15 hour bulk electrolysis in the presence of $P_3{}^BFe^+$, $Cp^*_2Co^+$, $[Ph_2NH_2][OTf]$ and N_2 at -2.1 V (vs Fc/Fc^+) presented in Figure A3.7.

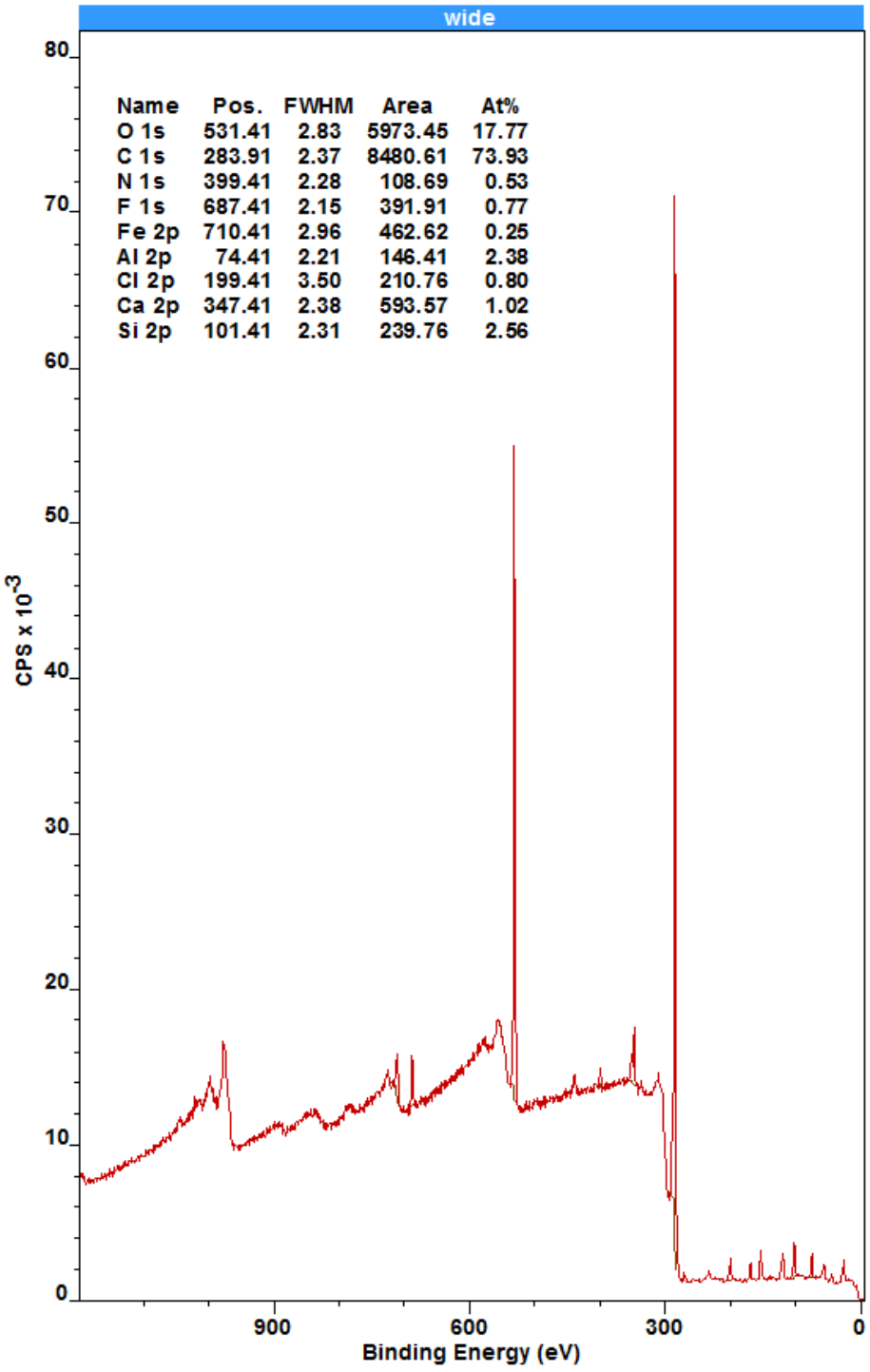
wide
Name Pos. FWHM Area At%
O 1s 531.41 2.83 5973.45 17.77
C 1s 283.91 2.37 8480.61 73.93
N 1s 399.41 2.28 108.69 0.53
F 1s 687.41 2.15 391.91 0.77
Fe 2p 710.41 2.96 462.62 0.25
Al 2p 74.41 2.21 146.41 2.38
Cl 2p 199.41 3.50 210.76 0.80
Ca 2p 347.41 2.38 593.57 1.02
Si 2p 101.41 2.31 239.76 2.56
CPS x 10^-3
80
70
60
50
40
30
20
10
0
900
600
300
0
Binding Energy (eV)

Figure A3.7. XPS survey scan of a section of a glassy carbon plate which was exposed to the working chamber solution during a 15 hour bulk electrolysis in the presence of $P_3^BFe^+$, $Cp^*_2Co^+$, $[Ph_2NH_2][OTf]$ and N_2 at -2.1 V (vs Fc/Fc^+). XPS and Auger peaks are assigned as labeled in the legend, which also includes atomic percentages calculated from component fits from scans of individual XPS regions. This material represents a post-electrolysis state of the electrode surface composition for comparison to a XPS survey scan of a section of the same glassy carbon plate which <u>was not</u> exposed to the working chamber solution during a 15 hour bulk electrolysis in the presence of $P_3^BFe^+$, $Cp^*_2Co^+$, $[Ph_2NH_2][OTf]$ and N_2 at -2.1 V (vs Fc/Fc^+) presented in figure A3.3.1.Notably this active surface scan reveals a small Fe signal attributed to some degree of decomposition of the $P_3^BFe^+$ catalyst over the course of the 15 hour electrolysis, also notable is that no new Co signal is observed in the post-electrolysis scan suggesting that $Cp^*_2Co^+$ does not decompose to a surface bound Co species in appreciable amounts during the electrolysis.

A3.12. pK_a Determination Strategy

Bosch et al. published a procedure for converting a pK_a in THF into the equivalent pK_a in different solvents.[26] Although not all of the pK_a values have been experimentally determined in THF the values obtained from converting from MeCN or H_2O into a THF value is quite accurate. So we have used these converted values in the text. Where available a number measured in THF has been used, if not the average of the two values has been used if available. These choices do not materially affect the analysis as the interpretation of pK_a effect is qualitative in nature.

Solvent conversion equations:

$pK_a(THF) = 0.78 \times pK_a(MeCN) - 0.52$

$pK_a(THF) = 1.19 \times pK_a(H_2O) + 2.13$

Acid	pK_a in MeCN	pK_a in H_2O	Converted pK_a [a]	Experimental pK_a in THF
[4-methoxyanilinium][OTf]	11.86[27]	5.29[29]	8.8 (8.4)	8.8[26]
[anilinium][OTf]	10.62[27]	4.58[29]	7.8 (7.6)	8.0[26]
[2,6-dimethylanilinium][OTf]	--	3.89[29]	-- (6.8)	
[2-chloroanilinium][OTf]	7.86[27]	2.64[29]	5.6 (5.3)	6.0[26]
[2,5-dichloroanilinium][OTf]	6.21[28]	1.53[27]	4.3 (4.0)	4.5[26]
[2,6-dichloroanilinium][OTf]	5.06[27]	0.42[30]	3.4 (2.6)	
[2,4,6-trichloroanilinium][OTf]	--	−0.03[30]	-- (2.1)	
[pentachloroanilinium][OTf]	2.35[28]	--	1.3 (--)	

[a]First is listed the value converted from THF and then in parentheses is the value converted from H_2O.

A3.13. References

[1] Robbins, J. L.; Edelstein, N.; Spencer, B.; Smart, J. C. Syntheses and Electronic Structures of Decamethylmetallocenes. *J. Am. Chem. Soc.* **1982**, *104*, 1882.

[2] Anderson, J. S.; Moret, M.-E.; Peters, J. C. Conversion of Fe–NH_2 to Fe–N_2 with Release of NH_3. *J. Am. Chem. Soc.* **2013**, *135*, 534.

[3] Moret, M.-E.; Peters, J. C. N_2 Functionalization at Iron Metallaboratranes. *J. Am. Chem. Soc.* **2011**, *133*, 18118.

[4] Del Castillo, T. J.; Thompson, N. B.; Peters, J. C. A Synthetic Single-Site Fe Nitrogenase: High Turnover, Freeze-Quench ^{57}Fe Mössbauer Data, and a Hydride Resting State. *J. Am. Chem. Soc.* **2016**, *138*, 5341.

[5] Grimme, S.; Antony, J.; Ehrlich, S.; Krieg, H. *J. Chem. Phys.* **2010**, *132*, 154104.

[6] Tao, J.; Perdew, J. P.; Staroverov, V. N.; Scuseria, G. E. Climbing the Density Functional Ladder: Nonempirical Meta-Generalized Gradient Approximation Designed for Molecules and Solids. *Phys. Rev. Lett.* **2003**, *91*, 146401.

[7] Weigend, F.; Ahlrichs, R. Balanced Basis Sets of Split Valence, Triple Zeta Valence and Quadruple Zeta Valence Quality for H to Rn: Design and Assessment of Accuracy. *Phys. Chem. Chem. Phys.* **2005**, *7*, 3297.

[8] *John Towns, Timothy Cockerill, Maytal Dahan, Ian Foster, Kelly Gaither, Andrew Grimshaw, Victor Hazlewood, Scott Lathrop, Dave Lifka, Gregory D. Peterson, Ralph Roskies, J. Ray Scott, Nancy Wilkins-Diehr, "XSEDE: Accelerating Scientific Discovery", Computing in Science & Engineering, vol.16, no. 5, pp. 62-74, Sept.-Oct. 2014, doi:10.1109/MCSE.2014.80*

[9] Valiev, M.; Bylaska, E. J.; Govind, N.; Kowalski, K.; Straatsma, T. P.; Van Dam, H. J. J.;

Wang, D.; Nieplocha, J.; Apra, E.; Windus, T. L.; de Jong, W. A. NWChem: A Comprehensive and Scalable Open-Source Solution for Large Scale Molecular Simulations. *Comput. Phys. Commun.* **2010**, *181*, 1477.

[10] Neese, F. The ORCA program system. *Wiley Interdiscip. Rev.: Comput. Mol. Sci.* **2012**, *2*, 73.

[11] Klamt, A.; Schüürmann, G. COSMO: A New Approach to Dielectric Screening in Solvents with Explicit Expressions for the Screening Energy and its Gradient. *J. Chem. Soc. Perkin Trans. 2.* **1993**, *2*, 799.

[12] Marten, B.; Kim, K.; Cortis, C.; Friesner, R. A.; Murphy, R. B.; Ringnalda, M. N.; Sitkoff, D.; Honig, B. New Model for Calculation of Solvation Energies: Correction of Self-Consistent Reaction Field Continuum Dielectric Theory for Short-Range Hydrogen Bonding Effects. *J. Phys. Chem.* **1996**, *100*, 11775.

[13] Ribeiro, R. F.; Marenich, A. V.; Cramer, C. J.; Truhlar, D. G. Use of Solution-Phase Vibrational Frequencies in Continuum Models for the Free Energy of Solvation. *J. Phys. Chem. B* **2011**, *115*, 14556.

[14] Wang, T.; Brudvig, G.; Batista, V. S. Characterization of Proton Coupled Electron Transfer in a Biomimetic Oxomanganese Complex: Evaluation of the DFT B3LYP Level of Theory. *J. Chem. Theory Comput.* **2010**, *6*, 755.

[15] Hamashima, Y.; Somei, H.; Shimura, Y.; Tamura, T.; Sodeoka, M. Amine-Salt-Controlled, Catalytic Asymmetric Conjugate Addition of Various Amines and Asymmetric

Protonation. *Org. Lett.* **2004**, *6*, 1861.

[16] Anderson, L. L.; Arnold, J.; Bergman, R. G. Proton-Catalyzed Hydroamination and Hydroarylation Reactions of Anilines and Alkenes: A Dramatic Effect of Counteranions on Reaction Efficiency. *J. Amer. Chem. Soc.* **2005**, *127*, 14542.

[17] Anderson, J. S.; Cutsail, G. E., III; Rittle, J.; Connor, B. A.; Gunderson, W. A.; Zhang, L.; Hoffman, B. M.; Peters, J. C. Characterization of an Fe=N-NH_2 Intermediate Relevant to Catalytic N_2 Reduction to NH_3. *J. Am. Chem. Soc.* **2015,** *137*, 7803.

[18] Stoll, S.; Schweiger, A. EasySpin, a Comprehensive Software Package for Spectral Simulation and Analysis in EPR. *J. Magn. Reson.* **2006**, *178*, 42.

[19] Marcus, R. A. On the Theory of Oxidation-Reduction Reactions Involving Electron Transfer. I. *J. Chem. Phys.* **1956**, *24*, 966.

[20] Iordanova, N.; Decornez, H.; Hammes-Schiffer, S. Theoretical Study of Electron, Proton, and Proton-Coupled Electron Transfer in Iron Bi-Imidazoline Complexes. *J. Am. Chem. Soc.* **2001**, *123*, 3723.

[21] Koper, M. T. M. Theory of Multiple Proton–Electron Transfer Reactions and its Implications for Electrocatalysis. *Chem. Sci.* **2013**, *4*, 2710.

[22] Onsager, L. Electric Moments of Molecules in Liquids. *J. Am. Chem. Soc.* **1936**, *58*, 1486.

[23] Thoss, M.; Evers, F. Perspective: Theory of Quantum Transport in Molecular Junctions. *J. Chem. Phys.* **2018**, *148*, 030901.

[24] (a) *web*PCET Application Server, University of Illinois at Urbana-Champaign,

http://webpcet.scs.uiuc.edu (2009) (b) Hammes-Schiffer, S.; Soudackov, A. V. *J. Phys. Chem. B* **2008**, *112*, 14108-14123.

[25] Warren, J. J.; Tronic, T. A.; Mayer, J. M. Thermochemistry of Proton-Coupled Electron Transfer Reagents and Its Implications. *Chem. Rev.* **2010**, *110*, 6961.

[26] Garrido, M. Rosés, C. Ràfols, E. Bosch Acidity of Several Anilinium Derivatives in Pure Tetrahydrofuran. *J. Soln. Chem.* 2008, *37*, 689.

[27] Kaljurand, I.; Kütt, A.; Sooväli, L.; Rodima, T.; Mäemets, V.; Leito, I.; Koppel, I. A. *J. Org. Chem.* **2005**, *70*, 1019.

[28] Haav, K.; Saame, J.; Kütt, A.; Leito, I. *Eur. J. Org. Chem.* **2012**, 2167.

[29] Pankratov, A. N.; Uchaeva, I. M.; Doronin, S. Y.; Chernova, R. K. *J. Struct. Chem.* **2001**, *42*, 739.

[30] Liao, K.; Pack, B. W.; Toltl, N. P. *J. Pharm. Biomed. Anal.* **2007**, *44*, 118.